SIMULATING THE INTERPLANETARY RADIATION ENVIRONMENT FOR GROUND BASED SPACE RADIATION STUDIES USING TARGETED ENERGY LOSS AND SPALLATION FROM ^{56}FE NUCLEI IN HYDROGEN-RICH CRYSTALLINE MATERIALS

A Dissertation

by

JEFFERY CADE CHANCELLOR

Submitted to the Office of Graduate and Professional Studies of
Texas A&M University
in partial fulfillment of the requirements for the degree of

DOCTOR OF PHILOSOPHY

Chair of Committee,	Helmut Katzgraber
Committee Members,	John R. Ford, Jr.
	Daniel G. Melconian
	Donald G. Naugle
Head of Department,	Grigory Rogachev

December 2018

Major Subject: Applied Physics

ABSTRACT

Currently ground-based radiobiology experiments are conducted with beams of single ions with single energies, a method that does not fully describe the radiation risks from the complex mixed ion field found in space. The health risks to humans during spaceflight would be better quantified if ground-based mixed field irradiations are utilized in radiobiology experiments and space vehicle shielding studies. Here we demonstrate that it is possible to reproduce the Linear Energy Transfer distribution in simulated tissue of the galactic cosmic ray spectrum expected during spaceflight. This is done by determining which intrinsic properties of polymer and hydrogen-rich crystalline materials influence desired nuclear spallation and fragmentation when placed in an accelerated heavy-ion beam. Using these results, we have matched a target moderator block made of multiple layers that generate the desired particle fragmentation and spallation products. The correct fluence of particles required for each layer (and thickness) will be determined using Monte Carlo methods. This final moderator block is then placed in front of a 1000 MeV per nucleon Iron (^{56}Fe) particle beam, resulting in a complex mix of nuclei and energies similar to the galactic cosmic ray spectrum measured inside the Space Shuttle, International Space Station, and the Orion Exploration Vehicle. Our approach can be generalized to other radiation spectra and is therefore of wide applicability for general radiation studies, not just of biological material, but also for the deployment of shielding, electronics, and other materials in a space environment.

ACKNOWLEDGMENTS

First, I would like to thank my research advisor Helmut Katzgraber. I am forever indebted for his guidance, insight, and unwavering support, but especially his friendship.

I am grateful to my committee members, John Ford, Dan Melconian, and Donald Naugle for their time, effort, and guidance in support of this work.

In addition, thank you to the many past and current members of my research group for many fruitful discussions and support throughout my graduate career; Amin Barzegar, Chao Fang, Darryl Jacob, Richard Lawrence, Oliver Melchert, Humberto Muñoz-Bauza, Chris Pattison, Dilina Perera, Wenlong Wang, Zheng Zhu, and Andrew Ochoa. I would also like to acknowledge the staff at the Department of Physics and Astronomy, especially Mrs Sheree Kessler and faculty members Drs. Artem Abanov, Joe Ross, Alexei Sokolov, and Kim-Vy H. Tran for their many efforts above to help me during graduate career at Texas A&M.

I am grateful for the support of the Texas Advanced Computing Center (TACC) at The University of Texas at Austin for providing HPC resources that have contributed to the research results reported within this paper. Adam Rusek and Peter Guida at the NASA Space Radiation Laboratory for their help collecting the beamline measurement data.

To my great friends Steve Guetersloh and Nic Stoffle who have watched me march down this road for many years and never left my side.

I would also like to thank my research collaborators who provided valuable insights during my studies; Keith Cengel, John Charles, Kate Rubins, and especially Ann Kennedy and Rebecca Blue. Ann, thank you for your years of mentorship and fantastic discussion on radiobiology. Becky, thank you for all our new collaborations on space radiation and medicine. Your keen eye for editing and lightening fast response times saved me on many occasions during this process. Mike Barratt, thank you for the many great talks and the keen insight on operational space medicine. I am also humbled and forever grateful to Jim Ziegler for reviewing my results and the manuscript submitted to Nature Microgravity.

To my amazing daughter Serafina, my family, Mom & Dad, friends and colleagues, too many to name, I could not have done this without a patient ear or excellent advice along the way. Thank you.

No one has committed more to this than my wife, Curly. You are my best friend and the love of my life. Remember that day we got married?. . . best day ever. *Ad astra per aspera*.

CONTRIBUTORS AND FUNDING SOURCES

Contributors

This work was supported by a thesis (or) dissertation committee consisting of Drs. Helmut Katzgraber, Dan Melconian and Donald Naugle of the Department of Physics & Astronomy and Dr. John Ford of the Department of Nuclear Engineering.

High performance computational resources were provided by the Texas Advanced Computing Center (TACC) at The University of Texas at Austin. The discussions on space radiobiology and medicine included input from Drs. Becky Blue, Serena Aunon-Chancellor, Keith Cengel, Ann Kennedy, and Kate Rubins. Beamline measurement were performed at the NASA Space Radiation Laboratory, Brookhaven, NY. All other work conducted for the dissertation was completed by the student independently.

No funding sources were used for this disseratation research

NOMENCLATURE

Fe	Iron nuclei
GCR	Galactic Cosmic Ray
GeV	Mega Electron Volt
HZE	High-Charge and High-Energy
INC	Intranuclear Cascade
IVA	Intravehicular Activity
ISS	International Space Station
keV	Kilo Electron Volt
LEO	Low Earth Orbit
LET	Linear Energy Transfer
MeV	Mega Electron Volt
NCRP	National Council on Radiation Protection and Measurements
PHITS	Particle and Heavy Ion Transport System
RBE	Relative Biological Effectiveness
SPE	Solar Particle Event

TABLE OF CONTENTS

Page

LIST OF FIGURES

FIGURE Page

LIST OF TABLES

1. INTRODUCTION

While space radiation research has expanded rapidly in recent years, large uncertainties remain in predicting and extrapolating biological responses to radiation exposure in humans. As future missions explore outside of *low-Earth orbit* (LEO) and away from the protection of the Earth's magnetic shielding, the nature of the radiation exposures that astronauts encounter will include higher radiation exposures than any experienced in historical human spaceflight. In 1988, the *National Council on Radiation Protection and Measurements* (NCRP) released Report No. 98: Guidance On Radiation Received in Space Activities [1]. In this report, authors recommended that NASA astronauts be limited to career lifetime radiation exposures that would induce no more than a 3% *Risk of Exposure-Induced Death* (REID). This was re-emphasized in the 2015 NCRP Commentary No. 23: Radiation Protection for Space Activities: Supplement to Previous Recommendations, which concluded that NASA should continue to observe the 3% REID career limit for future missions outside of LEO [2]. This limit has been accepted in NASA's Spaceflight Human-System Standard document, NASA STD-3001 Volume 1 (Revision A) [3].

Despite the adoption of these guidelines and the past 30 years of research, there has been little progress on fully defining or mitigating the space radiation risk to human crew. In fact, the NCRP's recent conclusions specified that their 3% limit may not be conservative enough, given the incomplete biological data used in existing projection models, and that such models may overestimate the number of allowable "safe days" in space for missions outside of LEO. One of the more pressing needs noted by the council as recently as 2015 was the continued paucity of an accurate space radiation analog for ground-based radiobiological studies [2]. To date, no pharmaceutical or biological countermeasure has been operationally implemented to help mitigate the space radiation threat. The space radiation threat, in part due to the lack of comprehensive understanding and analysis of the space radiation impact on the human body.

The study of human health risks of spaceflight (e.g., bone health, behavior, nutrition, etc.) typically involves analogs that closely represent the space environment. In almost all cases, theory,

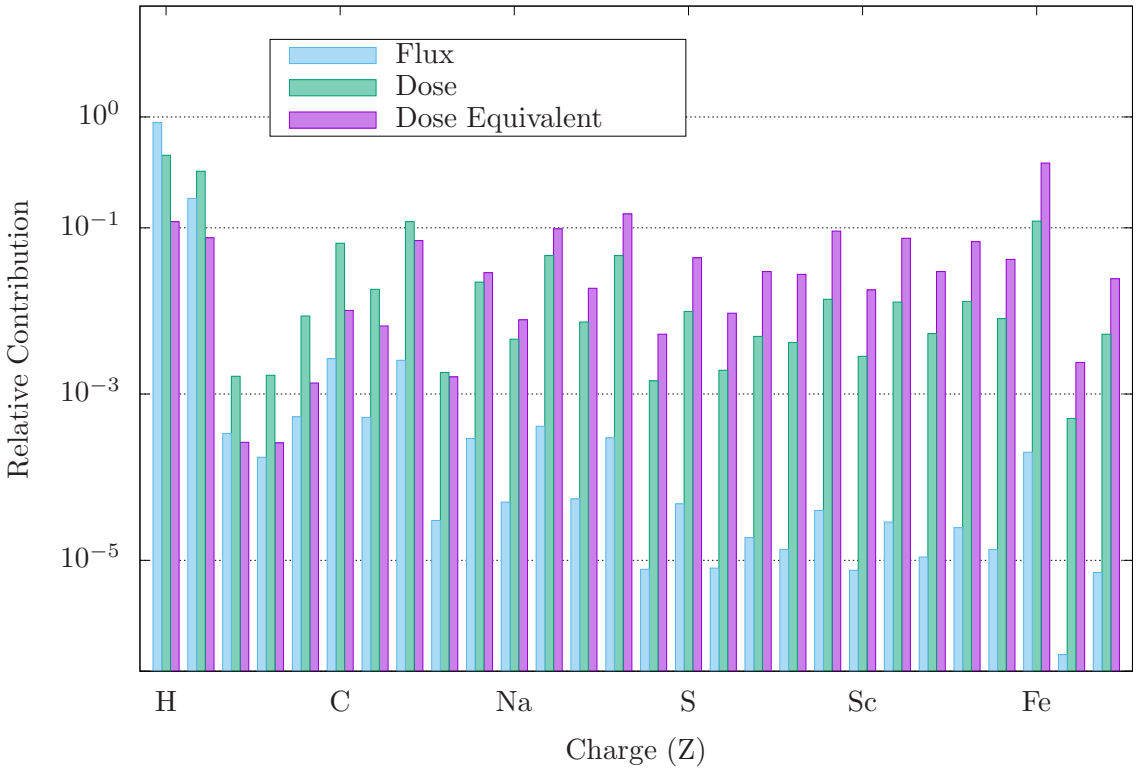

Figure 1.1: **Relative ion abundance of the galactic cosmic ray spectrum.** Relative abundance of the GCR spectrum, and the contribution to dose and dose equivalent from hydrogen ($Z = 1$) to nickel ($Z = 28$). The GCR is spectrum dominated by hydrogen ($Z = 1$) and helium ($Z = 2$) nuclei. While heavier ions such as iron ($Z = 26$) make up only a small portion of the spectrum, they contribute relatively larger energy doses to the cumulative radiation exposure than even hydrogen or helium.

models, and study outcomes can be validated with available spaceflight data or, at a minimum, observation of humans subjected to analog terrestrial stresses. In contrast, space radiation research is limited to the use of analogs or models that, for many reasons, do not accurately represent the operational space radiation environment or the complexity of human physiology. For example, historical epidemiological studies of radiation-exposed humans, which are generally used for correlation of animal and experimental models, include populations such as atomic bomb or nuclear accident survivors exposed to whole-body irradiation at high doses and high dose-rates, limited to scenarios not found in spaceflight.

The space radiation environment is a complex combination of fast-moving ions derived from all

atomic species found in the periodic table, with species ranging from hydrogen (atomic number $Z = 1$) through iron (atomic number $Z = 26$) comprising the majority of ion contributions (Figure 1.1). These ionized nuclei have sufficient energy to penetrate the spacecraft structure and cause deleterious biological damage to astronaut crews and other biological material, such as cell and tissue cultures [4, 5]. Furthermore, interaction with the spacecraft hull attenuates the energy of heavy charged particles and frequently causes their fragmentation into lighter, less energetic elements, changing the complexity and makeup of the intravehicular radiation spectrum. Modern radiobiology studies on the effects of space radiation generally use mono-energetic beams and acute, single-ion exposures (including protons, lithium, carbon, oxygen, silicon, iron, etc.) instead of the complex energy spectra and diverse ionic composition of the space radiation environment. In addition, a projected, cumulative mission dose[1] is often delivered in one-time, or rapid and sequential, doses delivered to experimental animals. In most cases, these dose-rates are several orders of magnitude higher than actual space environment exposures. Even the use of animal models introduces error, as studies make use of a variety of animal species with differing responses and sensitivity to radiation that may not represent human responses to similar exposures. Further, because of the lack of complexity in energy spectra, studies do not challenge multiple organ systems to respond concurrently to the numerous stressors seen in an operational spaceflight scenario.

These disparities and numerous other environmental considerations contribute to the large uncertainties in the outcomes of space radiobiology studies and the applicability of such studies for extrapolation and prediction of clinical health outcomes in future spaceflight crews. There are many risk posed to human health during spaceflight; however, radiation is the only significant health risk where research does not utilize models that accurately resembles stresses to human systems in an operational spaceflight scenario. Given the intended future of human spaceflight, with efforts now to rapidly expand capabilities for human missions to the moon and Mars, there is a pressing need to improve upon the understanding of the space radiation risk, predict likely clinical outcomes of

[1]Dose, or more formally the *effective dose*, is defined as the energy absorbed per unit mass measured in Joules per kilogram. The Gray (Gy) is the SI standard unit for the measurement of ionizing radiation dose [6]. Some older references refer to the previous SI unit of dose, the rad. 1 Gy = 100 rad

interplanetary radiation exposure, and develop appropriate and effective mitigation strategies for future missions. In fact, the National Research Council recently identified five highest-priority areas of technical challenges to be addressed for sustaining human health beyond LEO, one of which was the need to improve understanding of space radiation effects on humans to develop radiation protection technologies to enable exploration missions.

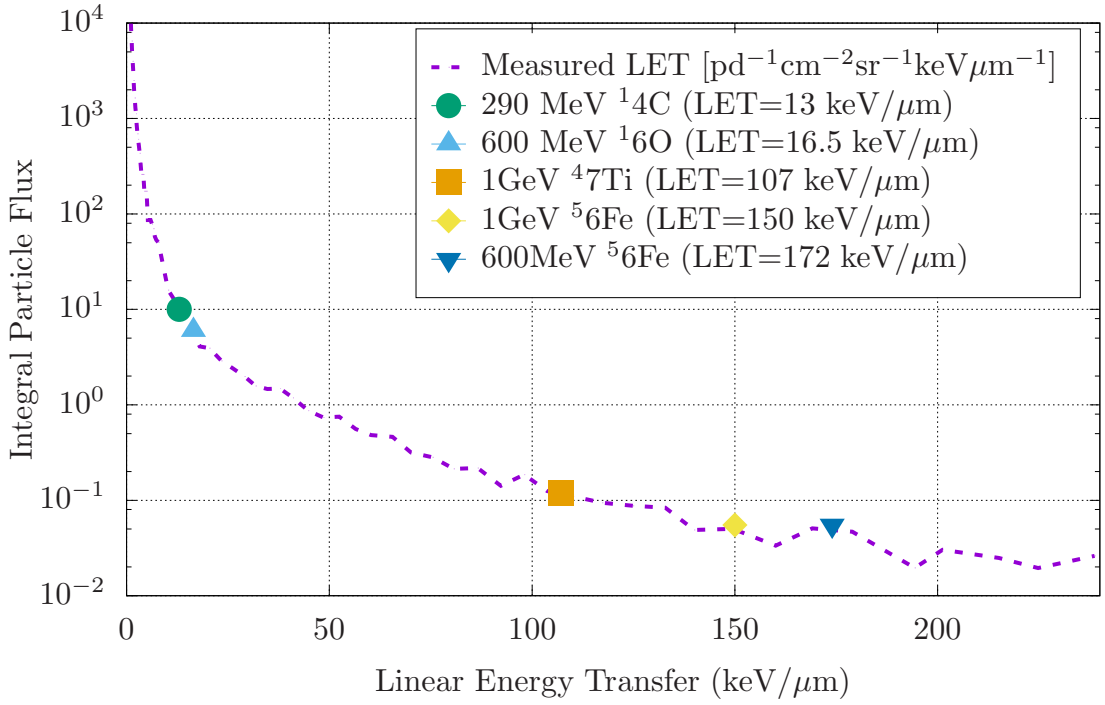

Figure 1.2: **Measured LET from U.S. Space Shuttle missions.** Displayed are the integrated LET/day values measured by Badhwar *et al.* 1998 (purple dotted line) [7], as well as the LET of five single-ion exposures, 290 MeV/n ^{14}C (carbon), 600MeV/n ^{16}O (oxygen), 1 GeV/n ^{47}Ti (titanium), 1 GeV/n ^{56}Fe (iron), and 600 MeV/n ^{56}Fe (iron). As studies generally focus on a single, mono-energetic radiation exposure, this figure highlights the lack in breadth of energies or radiation field complexity used in current radiobiological studies. Figure reprinted with permission from Chancellor et al.[8], under the Creative Commons license.

Recent studies have demonstrated that the biological response to space radiation is unique to the nonhomogeneous, multi-energetic dose distribution of the interplanetary space environment [9, 10]. As demonstrated in Figure 1.2, space radiobiology experiments conducted with beams of single

ions with single energies do not fully describe radiation risks from the complex mixed field found in space. It is reasonable to conclude that previous radiobiological models and experiments utilizing mono-energetic beams may not have fully characterized the biological responses or described the impact of space radiation on the health of vital tissues and organ systems. A ground-based space radiation analog utilizing multiple simultatneous beams would be the most efficient at producing a distribution of the relative abundance of ions found in galactic cosmic radiation (GCR).

The simultaneous experimental reproduction of *all* factors including dose-rate, ion composition, and energies found in the GCR spectrum is unlikely because of limits in current accelerator technologies. Recently, NASA has developed an updated GCR simulator capable of providing three to five consecutive mono-energetic ion beams, with rapid switching between ion species [11]. The NASA Space Radiation Laboratory (NSRL) is located at Brookhaven National Laboratory in Brookhaven, NY. Currently, NSRL is the only U.S. facility with the capabilities to generate heavy-charged particles at energies relevant to space radiation studies. While an improvement upon previous methods, NASA's new GCR simulator remains limited in its ability to emulate the GCR environment of deep space. The simulator lacks the capacity to generate the pions (subatomic particles) and neutrons that would follow spallation reactions, though these would make up 15-20% of a true intravehicular dose [12, 13, 11]. Sequential beam exposures remain ineffective in modeling complex and simultaneous exposures of the actual GCR environment, and there is significant debate regarding the appropriate order of ion exposures delivered (as alteration of exposure sequence can affect the outcomes of an experiment) [13, 14]. Finally, dose-rate delivered by this simulator will remain significantly higher than the radiation dose-rate anticipated for human crews during spaceflight [11, 12, 8].

We address these limitations with the development of a ground-based space radiation analog that closely resembles the complex intravehicular radiation environment. The analog is based on sound physics principles that have been previously rigorously validated and carefully applied to a real-world problem using Monte Carlo techniques and advanced multi-core, high-performance computers.

Highly charged, heavy ions penetrate matter with an approximate straight path and gradually dissipate energy through collisions with lattice atomic and electronic structure. These interactions result in energy transferred from the primary ion into the median, gradually dissipating the primary ion's energy or creating progeny nuclei and spallation fragments [15]. The energy loss is primarily associated with the many interactions with orbiting electrons and the effective *stopping power* of the material. To first order, the energy loss per distance traveled through the medium can be approximated with the equation frequently referred to as the stopping power,

$$\frac{dE}{dx} = n(Z)\,\frac{z^2}{v^2}\,\ln\Big[F(v,Z)\Big]. \tag{1.1}$$

Here $n(Z)$ is a constant dependent on the charge (Z) and atomic mass of the medium, z and v refer to the charge and velocity of the charged particle, and $F(v,Z)$ is logarithmic term that varies slowly over the ranges of velocities of interest. As mentioned, there is a chance that the interaction between the primary and the nuclear structure results in the dislocation of nuclear matter from the primary ion, creating fragments of ion species with charges up to the charge of the primary ion. Brandt and Peters demonstrated that the probability for a nuclear interaction to induce a charge-changing spallation can be determined from the primary ion's energy, geometric cross section, and mass number, A_{P}, as well as the mass number of the nuclei it is interacting with, A_{T} [16, 17]

$$\sigma = \pi r_0^2\Big[\sqrt[3]{A_{\mathrm{P}}} + \sqrt[3]{A_{\mathrm{T}}} - \delta(A_{\mathrm{T}}, A_{\mathrm{P}}, E)\Big]^2, \tag{1.2}$$

where γ is a fitted parameter dependent on the energy of the primary ion and $r_0 = 1.26$ fm. The concept of stopping and cross-sections will be developed in richer detail in Section 2.3.

Analysis of equation (1.1) shows that a charged particle traversing a given material will lose kinetic energy at a rate inversely proportional to its speed, with a prompt loss of energy as it comes to rest. This sudden rise in energy loss is referred to as the *Bragg peak* and is demonstrated in Figure 1.3. In this context, the term "Bragg peak" differs from the definition used in materials and condensed matter studies. In radiation dosimetry (and throughout this study), reference to the Bragg

peak will imply the point where a charged particle promptly loses kinetic energy before coming to rest in a medium.

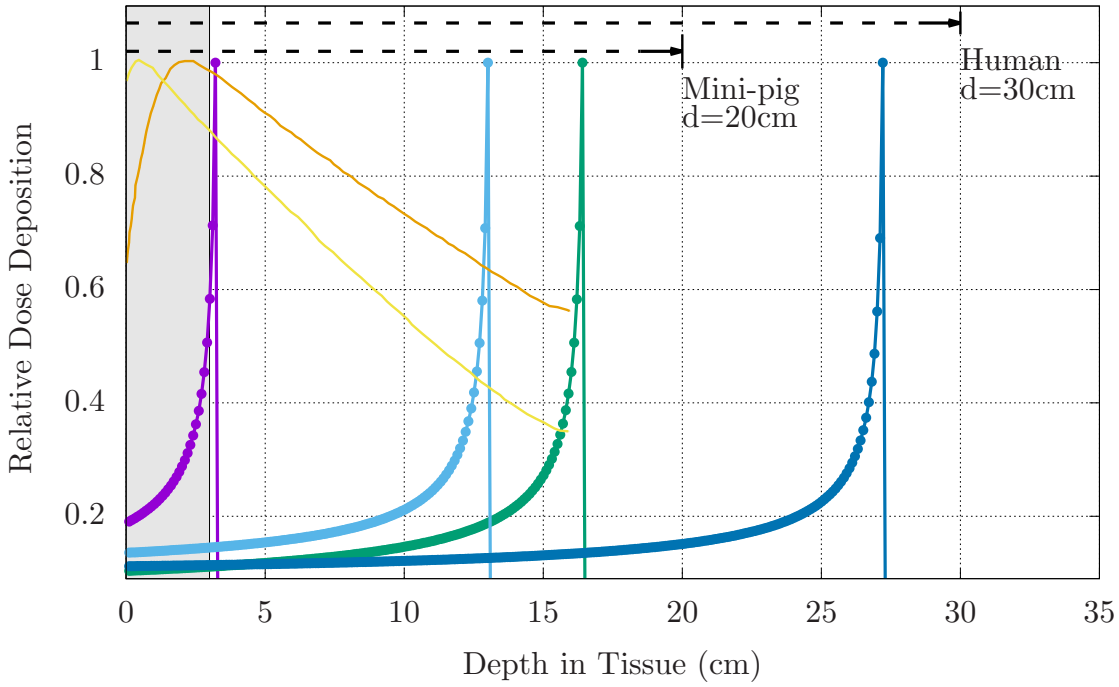

Figure 1.3: **Bragg peak and depth dose characteristics of space radiation.** Shown in the figure are the calculated Bragg peaks and relative dose deposition for ions at energies commonly used in space radiation studies. These are compared to the x-ray and gamma sources used as surrogate radiations for Relative Biological Effectiveness (RBE) quantification. This effect is very pronounced for fast moving, charged particles. Shown are 60 MeV protons (hydrogen, purple), 600 MeV/n ^{56}Fe (iron, light blue), 290 MeV/n ^{12}C (carbon, green), 1 GeV/n ^{56}Fe (iron, dark blue), x-ray (orange dotted line), and ^{60}Co (cobalt, yellow dotted line). The shaded gray area, representing the average diameter of a mouse, demonstrates that the Bragg peak, and thus the majority of dose deposition, is *outside* the mouse body for SPE protons (energies $\geq$ 50 MeV/n) and GCR ions. Figure reprinted with permission from Chancellor et al.[8], under the Creative Commons license.

These phenomena provide valuable information about the character and properties of materials, and provide a novel method of generating a mixed field of ions using accelerator technologies. Careful observation of equation (1.1) shows that a primary ion can penetrate a material of thickness, Δx, assuming a high enough incident energy, E. We can choose Δx so that roughly half of the primary ions have a charge-changing reaction defined by equation (1.2). With these constraints

the location of the first charge-changing interaction will occur, on average, at approximately the midpoint (e.g., $\Delta x/2$). The resulting secondary particles will then travel a distance equal to approximately half of the material's thickness, Δx, and will lose energy at a rate described by equation (1.1). Most nuclear reactions are peripheral and remove only a few nucleons from the incident primary ion. On average, observing equation (1.2), the probability of the lighter fragments having tertiary interactions is proportional to it's atomic mass e.g., $2/3\ A_{\mathrm{T}}$, or approximately 25%.

For a primary ion of constant energy, E, atomic mass, A_{P}, and charge, z, incident on a target with atomic mass, A_{T}, and thickness, Δx, the emerging field will consist of a mix ion species with charges up to that of the primary. Conceptually, it is reasonable to predict that a single particle, mono-energetic ion beam can be accelerated at target blocks constructed of one or more materials. The spectrum of the emerging field can then be *moderated* by the amount of mass or length of material the primary and secondary nuclei travels. The robustness of the resulting field of mixed ions and energies would be dependent on the careful selection of target material(s) and the relative contribution of each layer to the desired spectrum.

The stopping power is equivalent to the energy loss per unit path length of the primary ion, or the *Linear Energy Transfer* (LET), where $\mathrm{LET} = dE/dx$. The LET quantifies how much energy is lost in a material. It is typically given in units of MeV/cm for materials studies; however, for radiobiological quantification where the outcome varies at distances of 10^{-6} m, LET is given in keV/μm. A logical goal would be to simulate the LET distribution of the GCR environment. As shown in Table 1.1, LET, although not uniquely related to biological response, it is an important metric that is utilized to determine radiation tissue damage where the differences in the *relative biological effectiveness* (RBE) of different ions are, in part, attributed to differences in the LET of the radiation[2] [18]. LET remains the focus of many biological investigations and serves as the basis of radiation protection and risk assessment [19, 18].

Our model thus leverages available technologies to provide an enhancement to current ground-based analogs of the space radiation environment by reproducing the measured intravehicular LET

[2]The RBE of a particular radiation type is the numerical expression of the relative amount of damage that a fixed dose of that type of radiation will have on biological tissues.

Table 1.1: **Determination of quality factor, Q, and its dependence on the linear energy transfer**. The *dose equivalent*, (H), accounts for differing biological impact of radiation species. It is determined by the product of the measured dose (D) and dimensionless weighting factor, $Q(L)$, referred to as the *quality factor*. $H = Q(L)\ D$, and the SI unit for dose equivalent is the *Sievert*. $Q(L)$ is an *ad hoc* scaling estimate of the relative hazard of ionizing radiations of different species and energies to human health. The values of $Q(L)$ are arbitrarily defined by the NCRP and the International Commission on Radiation Units (ICRU) as a function of LET.

LET (keV/μm in water)	**Quality Factor** (*prior to 1990*)
3.5 or less	1
$3.5 - 7.0$	$1 - 2$
$7.0 - 23$	$2 - 5$
$23 - 53$	$5 - 10$
gamma, X-ray,	1
electrons	1

LET (keV/μm in water)	**Quality Factor** (*since 1990*)
< 10	1
$10 - 100$	$0.32\ L - 2.2$
> 100	$300/\sqrt{L}$

spectrum. In this work we demonstrate an approach to emulate the space radiation environment in a laboratory setting. For simplicity, we focus on the intravehicular radiation spectrum measured on different spacecrafts. We emphasize, however, that our approach can be generalized to other radiation spectra and is therefore of wide applicability for general radiation studies, not just of biological material, but also, for example, for the deployment of shielding, electronics, and materials in a space environment, or for nuclear research facilities and laboratories. Our goal is to develop a target moderator block that can be easily constructed from materials with multiple layers of varying geometry to generate specific nuclear reactions and spallation products.

The moderator block is designed so that the final field closely simulates the intravehicular LET spectrum measured on previous spaceflights. This target moderator block can, for example, be placed in front of a 1 GeV per nucleon (GeV/n) iron (^{56}Fe) single-particle beam and the resultant nuclear spallation processes will create modest amounts of the desired fragments resulting in a complex mixed field of particle nuclei with different atomic numbers, Z, in the range $1 < Z \leq 26$

and LETs $\leq$ 250 keV[3] per micron (keV/μm). The concept is shown in Fig. 1.4. Modifications to the internal geometry and chemical composition of the materials in the target moderator block allow for a shaping of the emulated intravehicular LET to specific spectra. We must emphasize that pragmatic decisions motivated material choice and subsequent geometry. It should be practical for a moderator block to be crafted with high precision in the machine shop of a typical accelerator laboratory, allowing for replicated use at any heavy-ion accelerator. Thus, polymers or soft materials were giving priority because of sufficient tensile strength and relative ease of machining.

The results from our numerical models are compared to measurements of the intravehicular LET spectrum from the U.S. Space Shuttle orbiter during the Shuttle-MIR missions, the International Space Station (ISS), and NASA's Orion Multi-Purpose Crew Vehicle (MPCV), clearly illustrating that the bespoke moderator blocks more accurately replicate the space radiation environment for ground-based radiobiology experiments. The results presented show that it is possible to closely mimics the dose-rate, distribution of ion species, and the expected LET spectrum measured on previous spaceflight missions. This approach can also be utilized to emulate the external GCR field, a planetary surface spectrum (, Mars), or a local radiation environment of orbiting satellites, and provides the first instance of a true ground-based analog for characterizing the effects of space radiation.

[3]keV or mega-electron volt. The electron-volt is the energy gained by an electron accelerated through a potential difference of 1 Volt [20]. In SI units, the electron-volt is equivalent to approximately $1.6202176 \times 10^{-19}$ Joules. 1 keV = 1,000 eV.

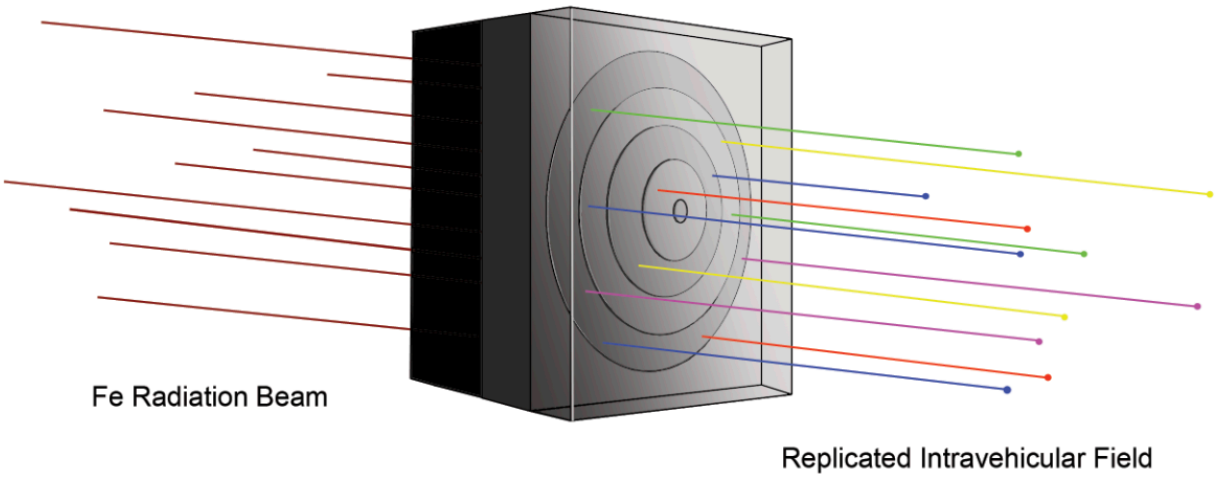

Figure 1.4: **Moderator block geometry concept for the emulation of space radiation spectra.** A primary beam of ^{56}Fe (iron, left) is selectively degraded with a carefully designed moderator block to produce a desired distribution of energies and ions (represented by the colorful lines on the right) simulating the intravehicular space radiation environment. To preferentially enhance fragmentation and energy loss, cuts are performed in the moderator block made up of different materials (depicted by different shades of gray). Before the spallation products exit the moderator block, a high-Z material layer is added for scattering. Figure reprinted with permission from Chancellor et al.[8], under the Creative Commons license.

2. BACKGROUND

A recent report by Schwadron et al., has identified important concerns regarding the interplanetary radiation environment and the risks to human spaceflight activity [21]. The unusually low activity between solar cycles 23 and 24 (1996-present) has resulted in the longest period of minimum solar activity observed in over 80 years of solar measurements. The lack of solar activity has led to a substantial decrease in solar wind density and magnetic field strengths that typically attenuate the fluence (the flux of particles crossing a given plane)[1] of GCR ions during periods of solar minimum. As a result, Schwadron et al., project that GCR fluences will be substantially higher during the next solar cycles (24-25) leading to increased background radiation exposure and, subsequently, as much as a 20% decrease in the allowable safe days in space (outside of LEO) to ensure that astronauts stay below the 3% REID limits [21] [2].

2.1 Space Radiation Environment

The primary sources of space radiation found in LEO are GCR, protons and a small component of heavier nuclei that make up solar particle events (SPE), and the electrons and protons that remain trapped in the Earth's magnetic field to form the Van Allen radiation belts [1]. The GCR and SPE particles are ionized nuclei that have been accelerated to very high velocities by various processes. Typical energies are in the range of 50 to 1000 MeV/n, which is much higher than the energies of ionizing particles from natural sources on Earth [23, 1, 24].

For the purpose of this dissertation, neither SPEs or trapped electrons or protons of the Van Allen Radiation belts are be considered when modeling the radiation environment. The descriptions below are intended to clarify the different radiation fields that encompass the space radiation environment.

[1] Flux is defined as number of particles passing a unit plane per unit time ($m^{-2}s^{-1}$), while the Fluence, or *flux density*, is the flux at any interval of time (m^{-2}) [22].

[2] Portions of Chapter 2 are reprinted with permission from Chancellor et al.[8], under the Creative Commons license

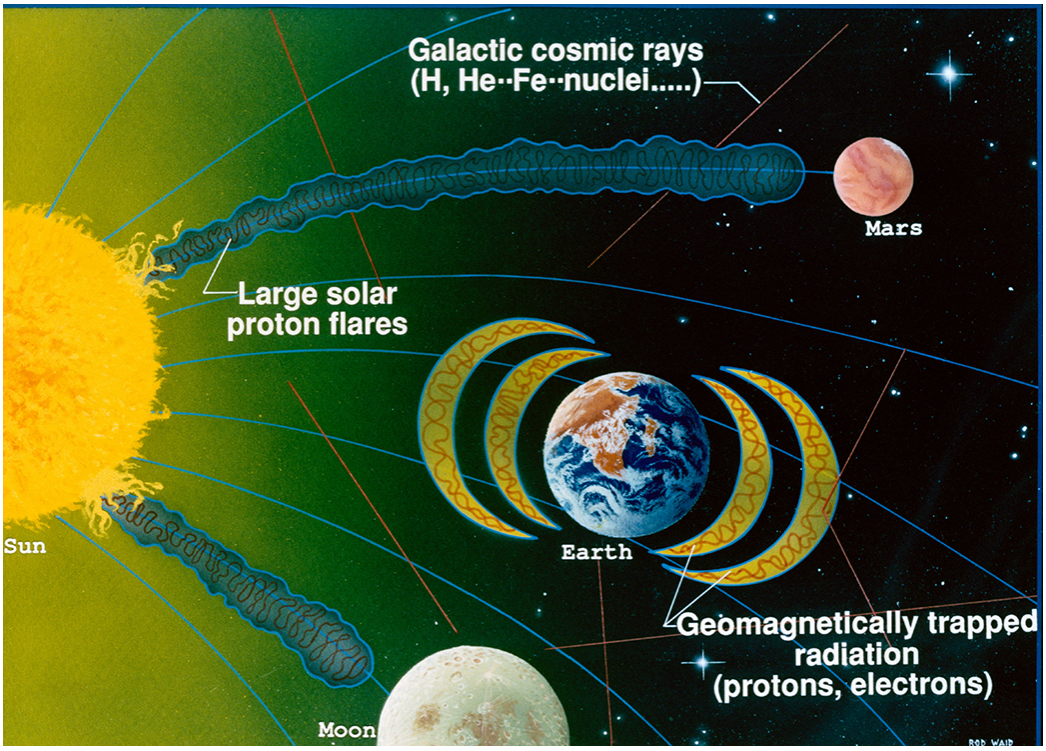

Figure 2.1: **Diagram of the space radiation environment.** Operational space radiation environment is comprised of three sources of ionizing radiation, energetic protons from solar particle events, relativistic heavy ions of the galactic cosmic ray spectrum, and trapped electrons and protons in the Van Allen Belts.

2.1.1 Solar Particle Events

During SPEs, magnetic disturbances on the surface of the sun result in the release of intense bursts of ionizing radiation that are difficult to forecast in advance [25, 26, 27]. SPE radiation is primarily composed of protons with kinetic energies ranging from 10 MeV up to several GeV. SPEs are predicted to produce a heterogeneous dose distribution within an exposed astronaut's body, with a relatively high superficial (skin) dose and a significantly lower dose to internal organs.

As extravehicular space suits provide relatively low shielding protection, SPE exposures occurring during extravehicular activities would pose significant risk to astronauts [28]. However, astronauts would still receive potentially significant elevations in radiation dose even within a shielded spacecraft and remain vulnerable, especially on long-duration missions, to both acute effects of sudden SPE radiation boluses and to the overall additive effects of GCR and repetitive

SPEs over the course of a mission.

While many SPEs show modest energy distributions, there are occasional and unpredictable high fluence events; for example, a particularly large SPE in October 1989 is predicted to have delivered dose-rates as high as 1,454 mGy/hour to an exposed astronaut in a vehicle traveling in interplanetary space. For context, consider that the daily dose for long-duration astronauts aboard the ISS is approximately 0.282 mGy/day [28, 29, 30]. Similarly, some SPE can deliver particularly high-energy doses: for example, 10-15% of the total fluence of an October 1989 SPE was made up of protons with energies in excess of 100 MeV/n [1, 28]. If an astronaut were exposed to such an event during long-duration spaceflight, there are potential risks for both acute radiation-induced illnesses and for significant increase in the overall mission dose accumulation. It should be noted that these predictions made use of classic shielding values of 5 g/cm^2, which is similar to those of the Apollo command module which had an average shielding of 6.15 g/cm^2 [31].

Energetic SPEs produce protons with energies greater than 100 MeV/n that would penetrate classic spacecraft shielding, potentially reaching blood-forming organ depths with deleterious clinical sequelae. These highly energetic SPE exposures delivered to crews undertaking interplanetary flight could result in potentially serious symptoms ranging from prodromal responses (nausea, vomiting, fatigue, weakness) to fatality. In addition, large SPE doses can produce degenerative effects associated with cancer, ocular cataracts, respiratory and digestive diseases, and damage to the microvasculature; while these effects are mostly latent and do not necessarily pose an immediate risk to crew health, their overall impact upon long-duration crews is an important consideration [32].

2.1.2 Galactic Cosmic Rays

GCR ions, originating from outside our solar system, are relativistic nuclei that possess sufficient energies to penetrate any shielding technology used on current mission vehicles [34]. The GCR spectrum is a complex combination of fast-moving ions derived from most atomic species found in the periodic table [23]. The GCR spectrum, from hydrogen ($Z = 1$) through iron ($Z = 26$), is shown in Figure 2.2. This spectrum consists of approximately 87% hydrogen ions (protons), 12%

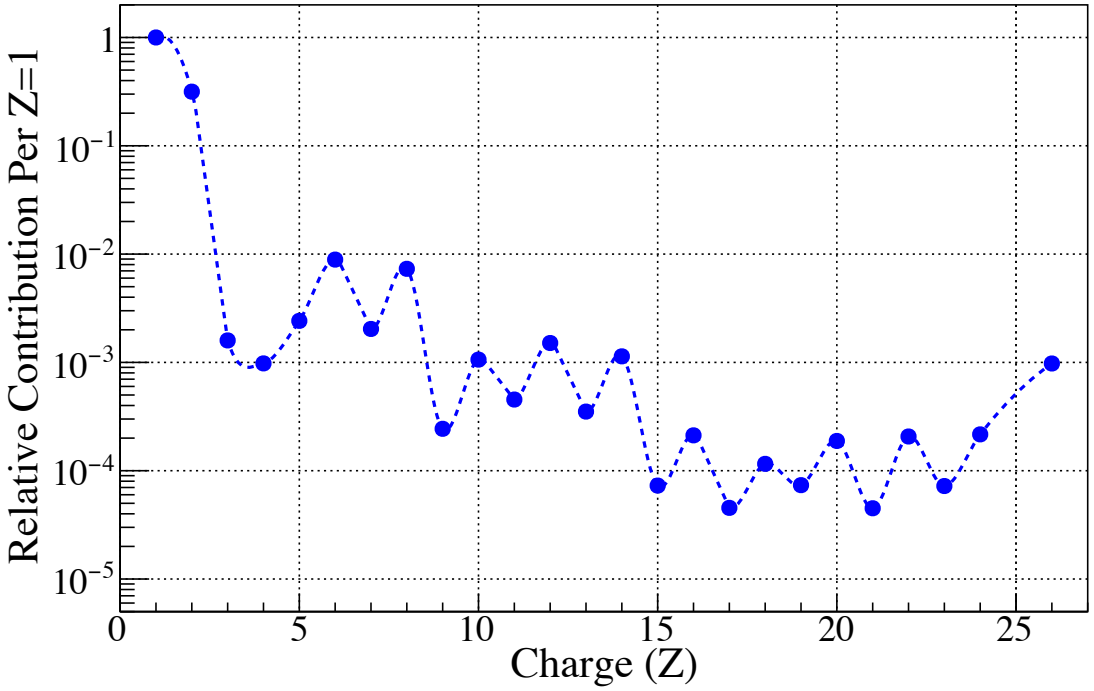

Figure 2.2: **Relative abundance of the GCR spectrum from $Z = 1$ up to $Z = 26$.** The relative contribution to the spectrum from Iron ($Z = 26$) is three orders of magnitude than the more prolific Hydrogen component [23, 33].

helium ions (α particles), and 1-2% heavier nuclei with charges ranging from $Z = 3$ (lithium) to $Z = 28$ (nickel) [23, 35]. Ions heavier than nickel are also present, but they are rare in occurrence. GCR ions with charge $Z \geq 3$ are frequently referred to as *HZE* particles (*H*igh nuclear charge *Z* and energy *E*).

During transit outside of LEO, every cell nucleus within an astronaut's body would be traversed by a hydrogen ion or delta ray, a recoil electron caused by fragmentation after ion interactions, every few days, and by a heavier GCR ion, e.g., O, Si, Fe, every few months [36, 37]. Despite their infrequency, the heavy ions contribute a significant amount to the GCR dose that astronauts would incur outside of LEO. The energies of the heavier GCR ions are so penetrating that shielding can only partially reduce the intravehicular doses [37]. Thicker shielding could provide protection, but is limited by mass and volume restrictions of exploration vehicles and dependent upon the

capabilities of spacecraft launch systems.

The high-LET radiation found in the GCR spectrum can produce excessive free radicals that instigate oxidative damage to cell structures. Chronic exposure to such oxidative stress contributes to the radiation-induced changes associated with premature aging, cardiovascular disease, and the formation of cataracts. The large ionization power of GCR ions makes them a potentially significant contributor to tissue damage and carcinogenesis, *central nervous system* (CNS) degeneration, and deleterious health outcomes [4, 5]. In addition, as GCR ions pass through a space vehicle, interaction with the spacecraft hull attenuates the energy of heavy-charged particles and frequently causes spallation reactions [38, 39]. Spallation occurring as GCR particles collide with shielding materials can result in 'cascade showers' that produce progeny ions with much higher potential for biological destruction than the original particle [34, 37, 40, 24]. This process changes the makeup of the intravehicular radiation spectrum, adding to the complexity of the radiation environment unique to spaceflight.

The fluence of GCR particles in interplanetary space fluctuates inversely with the solar cycle, with dose-rates of $50 - 100$ mGy/year at solar maximum to $150 - 300$ mGy/year at solar minimum [41]. The fluence and occurrence of SPEs is unpredictable, but dose-rates as high as $1400 - 2837$ mGy/hour are possible [1, 42, 28].

As discussed above, even if shielding in spacecraft effectively reduces radiation dose to the crew from SPEs, spallation occurring as GCR particles collide with shielding materials may lead to biological damage [34, 37, 40, 24]. Aluminum shielding greater than 20-30 g/cm^2 could only reduce the GCR effective dose by no more than 25% [43]. An equivalent mass of polyethylene would only provide about a 35% reduction in GCR dose [44, 45]. While this degree of shielding has been achieved aboard the ISS, similar shielding is impractical within exploration mission design parameters due to the limited lift-mass capabilities of planned space launch systems. The Apollo crew module is the only vehicle to date that has transported humans outside of LEO; this vehicle could only effectively shield SPE protons with energies less than approximately 75 MeV [31]. To date, no studies have successfully emulated the complexity of energetic elements of the

intravehicular radiation spectrum that astronauts are actually exposed to during space travel, or successfully incorporated vehicular design and shielding parameters in analog testing environments, limiting the understanding of the true effects of such an environment on the human body.

In addition to the highly penetrating GCR nuclei, the intravehicular dose found on the ISS includes secondary radiation created by fragmentation products (e.g., neutrons, protons, pions) of GCR particles interacting with the space vehicle structure and hardware [36, 46, 45]. Although the fluence of GCR particles is very low, the contribution to the mission dose is significant as they can have much higher stopping powers, and therefore a higher biological impact. The dose equivalent, a measure that takes into account the biological impact from ionized nuclei, is predicted to be approximately 10% from neutron fragmentation products, 70% from lighter GCR nuclei, and 20% from HZE particles. Assuming a space vehicle with an average areal density of 30 g/cm^2, the approximate average shielding of ISS, Walker *et. al.,*. determined that the relative contribution of the ISS intravehiclar dose would be : 10% for neutrons, 70% for $Z = 1$ or $Z = 2$, 5% for $3 \leq Z \leq 10$, 10% for $11 \leq Z \leq 20$, and 5% for $21 \leq Z \leq 28$ [5].

2.2 Modeling the Transfer of Energy for Space Radiobiology Experiments

As a charged particle traverses a material (such as spacecraft shielding, biological tissue, etc.), it continuously loses energy in particle interactions until the particle escapes the medium or has slowed enough to have strong interactions with orbiting electrons. This results in a rapid loss of particle energy over a very small distance with a corresponding rapid and sharp rise in LET. The Bragg peak (Figure 1.3) describes the rapid transfer of kinetic energy from a charged particle before the particle comes to rest in a medium. This peak is particularly pronounced for fast-moving, charged particles, indicating more substantial energy transfer and, as a result, the potential for greater deleterious biological effect from such particles. However, if a particle instead passes directly through tissue without sufficient energy loss to provide effective stopping power, the sudden energy loss associated with a Bragg peak does not occur and damage is minimal. Space radiation studies to date generally presume a homogeneous distribution of energy loss inclusive of the Bragg peak for each type of radiation, likely overestimating the relative damage of some exposures [47]. Improved modeling of

dose deposition and resultant biological sequelae specific to the space environment would advance risk estimation capabilities. The mechanisms for energy loss and charged particle interactions with matter are described in Section 2.3.

The biological effects of space radiation depend on multiple particle- and energy-specific factors, such as the LET specific to each ion, as well as the dose-rate of exposure. The RBE of a particular radiation type is the numerical expression of the relative amount of damage that a fixed dose of that type of radiation will have on biological tissues. Higher RBEs are associated with more damaging radiation for a given dose. RBE is determined using the effectiveness of cobalt (^{60}Co) gamma rays as a standard. An RBE equal to one means that the "test" radiation type (for example, heavy ion exposure) is as effective as ^{60}Co radiation at producing a biological effect, and an RBE greater than one means that the test radiation is more effective than ^{60}Co radiation at producing a biological effect. However, in some cases this comparative value does not fully represent the energy transfer curve of a specific radiobiological insult (Figure 2.3).

The effect of quantifying factors such as LET, particle identity, dose-rate, and total dose on RBE remains incompletely understood. The RBE can vary for the same particle type, depending on energy, dose-rate, target organ, and other factors. Different particle types are assigned a radiation *weighting factor* (formerly *quality factor*), W_{R}, that represents an average of calculated RBEs for a given particle. To identify the relative biological risk of a specific type and dose of radiation exposure, the physical dose (in Gy) is multiplied by W_{R} to obtain the biologically effective dose in units of *Sieverts* (Sv). This method of estimating dose and relative effect introduces limitations in predicting the true biological risk of exposures, particularly exposures to complex and poorly understood radiation environments.

There are numerous limitations of current terrestrial analogs used for studying and predicting space radiation effects on biological tissues. The mechanisms that cause biological damage from space radiation are uniquely different from those associated with terrestrial radiation sources that are frequently used as surrogates in space radiobiology studies. Charged particle radiation, including GCR and SPE, causes primarily direct ionization events, where biological effects are the direct

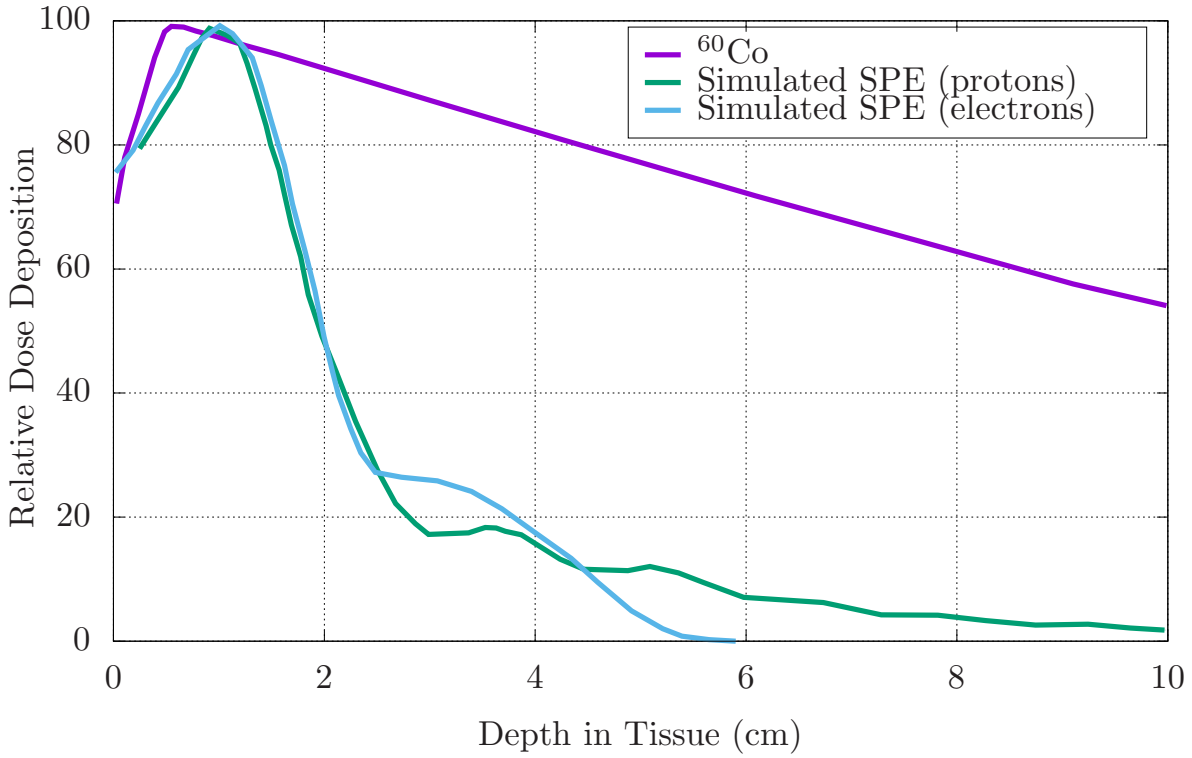

Figure 2.3: **Proton and electron range, energy and dose distributions for the October 1989 solar particle event compared to a dose-equivalent ^{60}Co exposure.** Charged particles (electrons, protons, heavy-charged particles) typically deposit more energy towards the end of their range. In contrast, the current standard, ^{60}Co radiation, loses the most energy at the tissue surface. These energy characteristics demonstrate the poor fidelity of ^{60}Co as a surrogate for studying the complex SPE and GCR spectrums. Figure adapted by permission from Springer Nature: Radiation and Environmental Biophysics, Cengel et al., [47].

result of interactions between the charged ion and impacted tissue. As charged particles lose energy successively through material interactions, each energy loss event can result in damage to the biological tissue. In contrast, terrestrial analogs often use radiation that causes indirect ionizing events. In indirect ionization, non-charged particles, such as photons, interact with other molecules and cause the release of charged particles, such as free radicals or electrons, that ultimately cause biological damage. Thus, it is difficult to extract a meaningful estimation of the direct ionizing space radiation impact through the use of terrestrial analogs and indirect ionizing radiation.

Models of the space environment outside of LEO have predicted that astronaut crews may receive a total body dose of approximately 1-2 mSv per day in interplanetary space and approximately

0.5-1 mSv per day on the Martian surface [37, 48]. These doses would increase with any SPE encountered over the course of the mission.

Many recent studies have led to ominous conclusions regarding the non-acute effects of GCR radiation on CNS and cardiovascular health that are difficult to interpret as real effects likely to occur in humans, but suggest that the protracted, low dose and dose-rate radiation exposure expected on longer exploration missions might lead to mission-relevant threats to astronaut health [49, 50]. These experiments were performed using rodent models exposed to single ion, mono-energetic heavy-ion beams, in some cases at total doses that are many times higher than the radiation human crews would experience during interplanetary space travel [51, 52, 53]. Even in studies where lower total doses are used, study methods delivered the cumulative mission doses for an entire mission over a very short period of time, typically over a few minutes [11, 54]. These parameters do not allow for critical physiologic components of the radiobiological response that would be expected under chronic, low-dose and low-dose-rate radiation conditions, such as cell regrowth and up-regulation of repair mechanisms [55]. Additionally, there is substantial evidence that GCR exposure at the dose-rates expected in interplanetary space may not induce acute or subacute biological responses, while acute exposure to total/cumulative dosage easily could [32].

Until recently, these multienergy-specific toxicity profiles and dose distributions were poorly understood. As a result, the majority of prior research has been based largely on simplified models of radiation transport, relying upon simple spherical geometry to estimate organ dose approximation at average depths [56, 57]. However, with this new evidence of heterogeneous dose distribution, spherical geometry is insufficient for the modeling of radiation delivered within the space environment.

2.2.1 Animal Model Sensitivity and Dose Simulation

For ease of dose specification and modeling, mono-energetic protons and GCR ions in the 100-1,000 MeV/n range are often used for *in vivo* animal model experiments such that the entire target is contained within the plateau portion of the depth-dose distribution [58, 59, 60, 61, 62]. In experimental animals that are much smaller than humans, simple scaling of particle energies

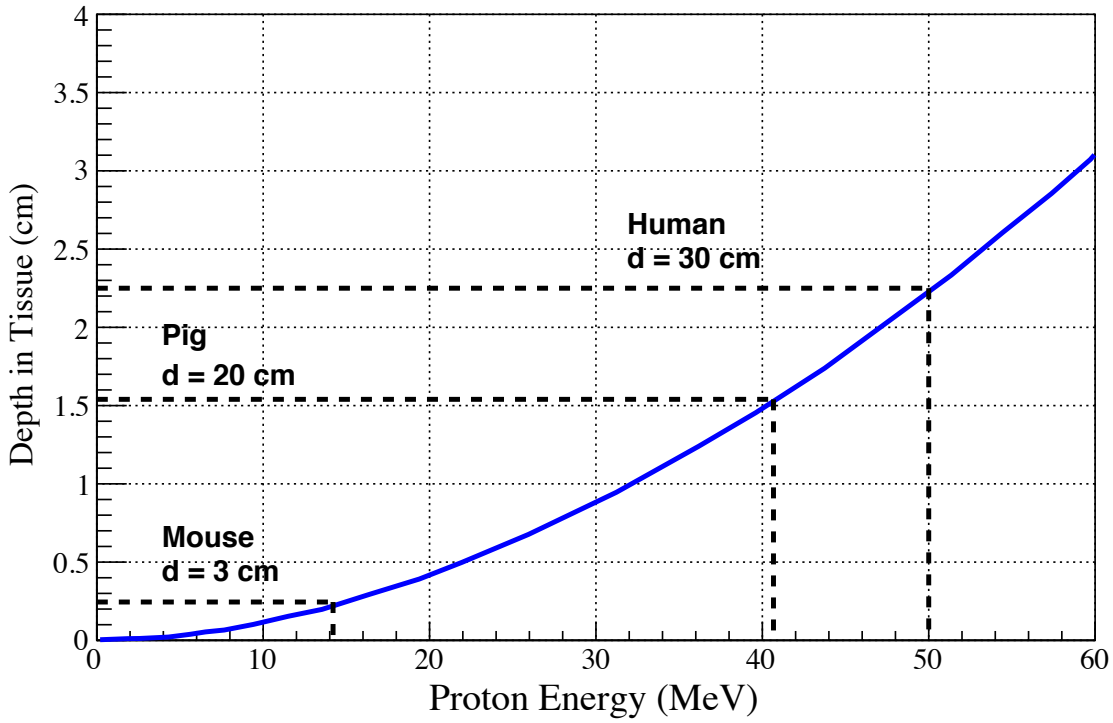

Figure 2.4: **Depth dose, energy, and linear energy transfer characteristics of protons.** Range of proton energies relative to the body diameter (dotted lines) and bone marrow depth (ordinate) for mice, pigs, and humans for energies up to 60 MeV. Figure adapted by permission from Springer Nature: Radiation and Environmental Biophysics, Cengel et al., [47].

to match dose distribution dramatically alters the LET spectrum for the protons (Figure 2.4). Conversely, delivering a simulated SPE or GCR exposure to smaller animals without scaling the energies would match their respective LET spectrum but create an heterogeneous dose distribution that is higher to internal organs than to superficial tissues, the exact inverse of the human SPE dose distribution [63]. For smaller animals (such as rodents), it is not possible to match both the LET spectrum and dose distribution of an SPE using protons [63, 64, 65]. Larger animal models, such as pigs or primates, allow for matching of the anticipated dose distribution for human SPE exposure using protons with a similar LET spectrum; thus, larger animal models are more likely than smaller species to provide robust estimations of human-specific space radiation effects [63]. However, it remains unclear whether the concurrent exposure to low-dose and dose-rate GCR radiation

Table 2.1: **LD_{50} of various animal models used in space radiobiology studies compared to the human LD_{50} dose following radiation exposures.** This broad spectrum in LD_{50} values emphasizes the difficulty in interpreting results of studies using specific radiation exposures in different animal models and translating them into clinical outcomes in humans.

Species	**LD_{50},(Gy)**	**Reference**
Ferret	< 2	Harding
Pigs	2.57	Morris & Jones
Dogs	2.62	Morris & Jones
Primates	4.61	Morris & Jones
Mice	8.16	Morris & Jones
Humans	3–4	Hall & Garcia

can be successfully emulated in small or large animal models [66]. Modeling of GCR radiation effects may be similarly altered by variations in animal species; however, without dedicated efforts towards expanding understanding of these phenomena, prediction of the biological consequences of long-term GCR exposure will remain theoretical at best.

Differences between animals and humans are clearly demonstrated by the characteristics of *radiation-induced death* (RID). The LD_{50} defines the required dose of an agent (e.g., radiation) necessary to cause fatality in 50% of those exposed. As illustrated in Table 2.1, remarkably different LD_{50} values have been reported for radiation exposure among different species. Currently, the genetic and physiologic basis for inter- and intra-species variation in LD_{50} is not well understood. Mice have been the most extensively developed model for human diseases including radiation-induced tissue damage. Rodent models have a high potential utility in describing the physiologic and genetic basis for many aspects of the mammalian radiation response. Even so, it should be noted that, in addition to simple physiological differences between mice and larger animals (including significantly higher metabolic rate, shorter lifespan, and lower body mass), the LD_{50} for mice is significantly higher than that of most other mammalian species, including humans.

It has been proposed that the differences between the LD_{50} values for humans compared to small mammals, like rodents, are due to different mechanisms involved in RID at these dose levels. For mammals, death at the LD_{50} dose is thought to be caused by the hematopoietic syndrome, which

includes destruction of precursor cell lines within blood-forming organs. Historically, it was thought that infection and hemorrhage are the major causes of death from hematopoietic syndrome, with one or the other of these factors predominating in different species' responses to lethal radiation exposure [67]. For example, bacterial infection is the predominate factor leading to RID in mice at doses near their respective LD_{50} levels [67, 68, 69]. However, recent results from Krigsfeld et al. have indicated that *radiation-induced coagulopathy* (RIC) and clinical sequelae that mimic *disseminated intravascular coagulation* (DIC) can result in hemorrhage, microvascular thrombosis, organ damage, and death from multiorgan failure from exposure of large animals (including ferrets and pigs) to doses of radiation at or near the species' LD_{50} [70, 71, 72, 73, 74]. RIC-associated hemorrhage occurs well before the expected decline in peripheral platelet counts after irradiation. Rodents do not exhibit signs of hemorrhage or disorders of primary hemostasis at time of necropsy after lethal radiation exposure at doses near the LD_{50} dose, while large animals, including humans, do exhibit hemorrhage at death following radiation exposure. These findings suggest that humans may be at risk for coagulopathy-induced complications after radiation exposure in addition to the classically anticipated (delayed) concerns of infectious sequelae or cell-count decline, effects that may not be modeled by rodent surrogates.

Further, RBE values for proton irradiation vary between animal models. In general, RBE values increase with animal size, with mini-pigs demonstrating higher RBEs than ferrets, and ferrets, in turn, exhibiting higher RBEs than mice [75] (Table 2.2). Numerous studies have focused on RBE values for hematopoietic cells in mice at various time points after the animals have been exposed to different doses of proton or gamma radiation [76, 77]. In these rodent models, RBEs do not differ significantly from 1.0 at any of the time points or doses of radiation evaluated. However, similar studies in ferrets and mini-pigs have demonstrated alterations of RBE value that are dependent upon animal model, type of radiation, time since exposure, and cell-line evaluated (for example, total white blood cell count vs. neutrophils). In one study, proton-irradiated ferrets examined 48 hours after exposure demonstrated RBEs for white blood cells ranging from $1.2 - 1.6$ and RBEs for neutrophils ranging from $1.9 - 2.1$ [78]. In Yucatan mini-pigs evaluated four days after exposure,

Table 2.2: **Relative biological effectiveness for SPE-like protons.** When compared with standard reference radiations (gamma or electron) in animal models [78, 65, 76, 77], the RBE of proton exposure varies greatly for total white blood cells (WBC) and specifically for neutrophils. Note that ferret RBE values were determined 48 hours after exposure; mini-pig values were determined 4 days post-irradiation.

Animal	**WBC**	**Neutrophil**
Mouse	1	1
Ferret	$1.16 - 1.6$	$1.9 - 2$
Mini-Pig	$2.4 - 4.1$	$2.2 - 5$

the RBEs for white blood cells was found to be $2.4 - 4.1$ and the RBEs for neutrophils was $2.2 - 5.0$ [65] (see Table 2.2).

In other experiments, proton exposure in mini-pigs again resulted in significantly greater hematopoietic injury and white blood cell count reduction than comparable gamma exposure [64, 65]. The results of these studies demonstrate that RBE values of different radiation types, calculated for the same endpoints, can vary greatly by animal species and cell line. One contributing factor may be the repair capacity of the blood cell renewal systems in mice; such capabilities appear to be lacking in mini-pigs (an animal model with more human-like hematopoietic characteristics), making them more susceptible to radiation-induced declines in cell counts. Given the presumed closer approximation of radiation effects in larger animals to human-specific consequences, this suggests that space radiation-specific RBE values for humans may be considerably higher than those in mice.

These studies demonstrated novel efforts towards an integrated, physiology-based approach for the evaluation of organ system- and species-specific endpoints. Using a more comprehensive evaluation of radiation toxicity for multiple doses and dose-rates in multiple animal models, this effort advanced the understanding of the impact of genetic heterogeneity and demonstrated that animal model, physiology, body mass, and fidelity of a space radiation analog (in this case, a multi-energy proton spectrum) all contribute to radiation response. Such efforts towards the integration of the numerous factors that contribute to radiation-induced effects, coupled with an ground-based analog that accurately represents the space radiation environment, will be critical to translation of

research results and prediction of clinical responses in humans.

2.2.2 Translation of Space Radiobiology Research to Human Health Outcomes

To date, there have been no biological or pharmaceutical countermeasures implemented in operational space flight. This has been true since the beginning of manned spaceflight and remains a major concern for exploration missions outside of LEO [9, 8]. This limitation arises, in part, due to the paucity of knowledge regarding risk of biological damage from space radiation exposure, the difficult translation of terrestrial radiation understanding to the space environment, and the lack of development of accurate space radiobiology analogs for rapid advances in terrestrial research.

Biological damage from radiation exposure is generally classified as *deterministic*, dose threshold-based effects related to significant cell damage or death (for example, the spectrum of clinical manifestations that make up Acute Radiation Sickness), or *stochastic*, where increased exposure is associated with increased risk though no threshold dose is necessary for biological impact (for example, carcinogenesis) [79]. Currently, carcinogenesis is the only long-term, stochastic effect that has a clearly defined permissible exposure limit in spaceflight. Terrestrial radiation (e.g., occupational or clinical radiotherapy gamma or x-ray exposures) is known to be associated with carcinogenic risk; at this time, there is no definitive evidence that space radiation causes human cancer, but it is reasonable to assume that it can [80]. The dose-equivalent of radiation received by astronauts currently traveling to the ISS for 6 months is approximately 100mSv [81]; doses of 100mSv of terrestrial radiation sources have been associated with an elevated cancer risk in human populations [80]. NASA's "Lifetime Surveillance of Astronaut Health" (LSAH) program documents cancer cases in astronauts, among other health parameters. Previous review of LSAH data suggests that there may be evidence of increased cancer risk in astronauts compared to a control population, though data are inconclusive and limited by the very small sample size [82].

Most evidence for the effects of space-like radiation exposures in humans has been derived from epidemiological studies on the atomic-bomb survivors, radiotherapy patients, and occupationally-exposed workers. These studies have focused on the association between ionizing radiation exposure and the long-term development of degenerative tissue effects such as heart disease, cataracts,

immunological changes, cancer, and premature aging for moderate to high doses of low-LET radiation [83, 84]. The findings are further supported by results of laboratory studies using rodent animal models [85]. However, true risks for these diseases from low dose-rate exposures to GCR and intermittent SPE are much more difficult to assess due to long latency periods and the numerous challenges involved in studying the radiation environment [85]. Additionally, the types of radiation exposure produced by atomic bombs (high dose and high dose-rate gamma and neutron radiation) are dissimilar to radiation exposures for astronaut crews during spaceflight.

The theoretical, calculated RBEs for some space radiation-induced cancers are quite high, which has led to speculation that the risk of cancer development from space radiation exposure is at least as high, and perhaps higher, than the risk of cancer development from exposure to radiation on Earth [86, 87]. However, there are currently no biophysical models that can accurately project all acute, subacute, degenerative, and carcinogenic risks specific to the range of particles and energies of ionizing radiation in the space environment. There is little information available about dose response and dose-rate modifiers for specific effects or about the degenerative effects associated with ionizing radiation, and very few biological models describe degenerative processes (e.g. cardiovascular degeneration) caused by ionizing radiation [88].

Exposure to the LEO radiation environment has been associated with alterations to chromatin structure [89, 90, 91, 92]. However, it is not well understood how such damage relates to impacts on cellular function or long-term carcinogenic risk. There is a paucity of understanding regarding the interpretation of chromosomal damage rates identified in astronauts and the long-term effects induced by the space radiation environment, without relying on terrestrial studies of different radiation sources, doses, dose-rates, or complexity for context. For example, NASA's Human Research Program Evidence Report on the Risk of Radiation Carcinogenesis [93], published in 2016, cites numerous studies to provide an assessment of risk for chromosomal damage (and, ultimately, carcinogenesis). A review of the studies cited in this report highlights the limitations described throughout this manuscript, including reliance upon mono-energetic radiation sources [51, 94, 92, 95, 54, 53], comparison to or interpretation of results in the context of gamma or x-ray

exposures [94, 95, 96, 54, 53], or use of dose or dose-rates far exceeding those expected during spaceflight [51, 92, 54, 53]. Indeed, many of these same factors are cited as limitations to NASA's primary radiation cancer risk prediction model [97].

2.3 Charged Particle Interactions in Matter

The current method of modeling the physical interactions of a complex spectrum of heavy charged particles in the space radiation environment by relating it to a homogenous analog is fundamentally flawed. It is not a reasonable approximation "to normalize" the multi-ion, multi-energy GCR spectrum to a rapid, single energy exposure. Inherent in our approach is the questioning of whether the accepted paradigm of using traditional terrestrial radiation protection can be applied to the space environment. This requires a richer discussion of the unique mechanics of heavy-charged particle interactions with materials.

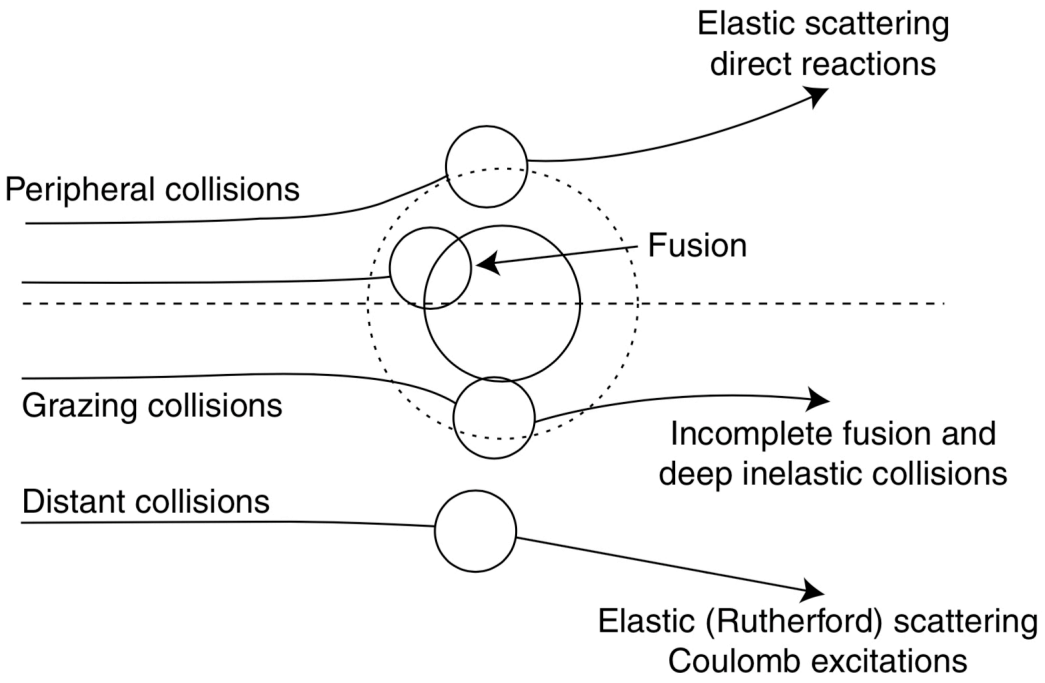

Figure 2.5: Trajectory of heavy ion reactions corresponding to close, grazing, peripheral and Coulomb collisions. Figure reprinted with permission from Loveland et al., Reference [98].

The study of how high energy, heavy charged particle radiation traverses through matter began with the works of Rutherford and Bragg [15]. A charged particle passing an atom at a considerable distance that is greater than a minimum distance for nuclear overlap the influence of the particle's Coulomb force field affects the atom as a whole. The perturbation can excite the atom to a higher energy level, possibly ionizing it by ejecting a valence-shell electron. The net effect is the transfer of a very small amount of energy (a few eV) to an atom of the absorbing medium. An incident particle can also interact primarily with a single atomic electron, which is ejected from the atom with considerable kinetic energy. These ejected electrons are referred to as delta rays, δ.

A heavy charged particle with sufficiently high kinetic energy and a de Broglie wavelength, $\lambda = \hbar/\sqrt{2ME_{\mathrm{CM}}}$), less than the nuclear radius may also interact inelastically with the nucleus. The resulting reactions can be described by the minimal distance between the two interacting ions, r_{min},

$$r_{\mathrm{min}} = \frac{b}{\sqrt{1 - V(r_{\mathrm{min}}/E_{\mathrm{CM}})}}, \tag{2.1}$$

where $V(r_{\mathrm{min}})$ is the potential energy between the ion and nucleus. It is then possible to distinguish four regions where the reaction mechanisms dominate below a minimum threshold distance as demonstrated in Figure 2.5:

1. the fusion region where $0 \leq r_{\mathrm{min}} \leq R_{\mathrm{F}}$,
2. the deep inelastic and incomplete fusion region where $R_{\mathrm{F}} < r_{\mathrm{min}} \leq R_{\mathrm{DIC}}$,
3. peripheral region where $\leq R_{\mathrm{DIC}} < r_{\mathrm{min}} \leq R_{\mathrm{N}}$,
4. the Coulomb region with $r_{\mathrm{min}} > R_{\mathrm{N}}$, where R_{N} is the distance above where nuclear reactions are negligible.

In the *fusion* region (R_{F}), the interaction leads predominantly to the formation of a stable composite nucleus, but not before a considerable fraction of the excitation energy is released in the form of fast particle clusters with energies greater than the thermal energy. In the *deep inelastic* and *incomplete fusion* (R_{DIC}) region, the overlap of the ions is sufficient to allow the transfer of a

sizable fraction of the kinetic energy to internal excitation energy. The result is the possible transfer of nucleons[3] between the interacting pair of ions. This can result in one or more of the individual nucleons (protons or neutrons) knocked out of the nucleus in an *intranuclear cascade* process that is collimated in the forward direction. The highly excited nucleus will decay from it's excited state by emitting the so-called *evaporation* particles consisting mostly nucleons of relatively low energy and γ-rays. In the *peripheral* region, the interaction of the ion pairs results, with increasing impact parameter, with the transfer of one or more nucleons and elastic and elastic scattering. In the *Coulomb* region, interactions between the ion nucleus is negligible and the dominating process is the scattering by the Coulomb fields.

For the intermediate energies (e.g., $50 \leq E \leq 1000$ MeV/n) and range of ions species of interest in this study, the dominating nuclear reaction are in the Coulomb and peripheral regions. The dynamics of these reactions will be discussed in the following sections with a focus on the particular mechanics of interest.

2.3.1 Energy Loss

As described in equation (2.3) below, energy loss and elastic scatting are the dominating processes when the minimum interaction distance, $r_{\min}$ is greater than R_{N}. The mechanisms of the energy loss are dependent on the primary ion's energy and charge and the intrinsic properties of the atomic nuclei in the median [22, 99, 100]. Bohr was the first to propose a unified theory of energy loss by introducing atomic structure and accounting for energy transferred to electrons by considering them as harmonic oscillators. His description of ion energy loss during passage through matter has two distinct elements: the transfer of energy from the primary ion to the (1) nucleons that make up the atom's nucleus, and (2) to orbital electrons [101]. Bohr correctly assumed the majority of energy loss would be attributed to the electronic interactions with atomic orbitals. This was later confirmed by Bethe, who demonstrated that the energy transfer to atomic nucleons was greater than one percent of the energy loss.

[3]Nucleon refers to either the proton or neutron that make of an atom's nucleus. The nuclear mass, A, of an atom is thus the sum of the nucleon masses.

Bohr's approach considers a heavy particle of charge z that is moving at a velocity v that passes through a median having a uniform density of *n* electrons per unit volume. Binary collisions from the interaction of electromagnetic forces result in a momentum transfer between the primary and target electrons. Using conservation of energy, the momentum impulse transverse to the path of the primary ion can be shown to be,

$$\Delta p = \int_{-\infty}^{\infty} k_0 e E(t)\, dt \;=\; \frac{2k_0 z e^2}{bv}, \tag{2.2}$$

where $k_0 = 8.99{\times}10^9 \mathrm{Nm^2C^{-2}}$, e is the electron charge ($e = 1.60217646 \times 10^{-19}$ C) and b is the impact parameter that describes the closest distance of approach between the primary ion and the nucleus of the atom (see Figure 2.6). This results in a transfer of energy to a atom's orbiting electron given by,

$$\Delta E = \frac{\Delta p^2}{2m_e} = \frac{2k_0 z^2 e^4}{m_e v^2 b^2} \tag{2.3}$$

where, in this expression, Bohr assumes that the electron recoil is much smaller relative to the impact parameter. The energy loss is then given by,

$$dE = 2\pi\, \frac{2k_0 z^2 e^4}{m_e v^2 b^2}\, b\, db\, dx, \tag{2.4}$$

which can be integrated to give the energy transferred to the electronic median per unit path length, dE/dx, frequently referred to as the stopping power,

$$\frac{dE}{dx} = 2\pi\, \frac{2k_0 z^2 e^4}{m_e v^2} \int_{-\infty}^{\infty} \frac{db}{b}. \tag{2.5}$$

The integral of this expression diverges as $b \rightarrow$0, necessitating the need for establishing a minimum impact parameter, $b_{\min}$. For heavy charged particles, e.g., protons or larger, the electron mass is much smaller, $m_e \ll m_p$, and will recoil strongly for very small impact parameter, contradicting the earlier assumptions of very small electron collision recoil. This can be resolved by constraining the minimum distance to the recoil electron's de Broglie wavelength, $\lambda = h/m_e v$, and thus establishing

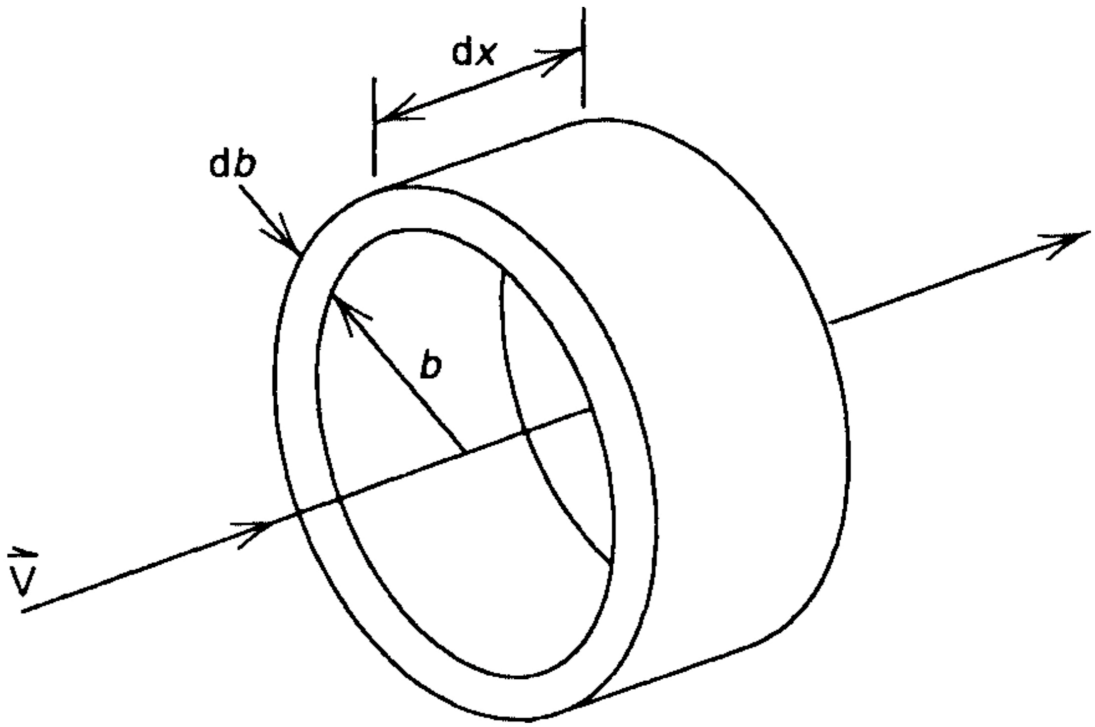

Figure 2.6: **Geometry of heavy charged particles electronic interactions with nuclei.** Here b defines the impact parameter for a charged particle with velocity v passing close to an electron located at the origin. Figure reproduced with permission from Turner et. al. 2008 [6].

a minimum impact parameter, $b_{\min} = h/m_e v$.

The integral also becomes undefined as $b \rightarrow \infty$. This can be made more tractable by limiting the collision between the primary ion and the recoil electron to adiabatic interactions. This establishes a maximum impact threshold for when the interaction time becomes longer than orbiting frequency of the recoil electron, $b_{\max}$, is approximately v/ω. With these constraints to the allowable values of impact parameters, the energy loss becomes,

$$\frac{dE}{dx} = \frac{4\pi k_0 z^2 e^4}{m_e v^2} \ln\left(\frac{m_e v^2}{h\,\omega}\right). \tag{2.6}$$

Equation (2.6) does not account for relativistic effects. Additionally, as the equation was developed before quantum mechanics, it imposes *ad hoc* constraints to the impact parameter, b, that

assumes the primary particle has a well defined momentum and localized position. Thus, Bethe introduced the first complete solution energy loss using the first Born approximation where the entire system is considered quantized. Bethe, along with Moller, later extended the solution to include corrections for relativistic ions [102, 103]. Subsequently, Fano proposed corrections to the energy-loss equation that accounted for low velocity primaries (e.g., velocities comparable to the velocities of the electrons in the target atoms) and polarizing effects due to dipole distortion in the medium at relativistic energies. These are referred to as the shell and density effect corrections, C/Z, and δ/2, respectively [104].

These results allow for the description of energy loss as heavy charged particles traverse a medium to be descibed by,

$$\frac{dE}{dx} = \frac{4\pi e^4 z^2\ Z}{m_e c^2 \beta^2}\left[\ln\left(\frac{2m_e\gamma^2\beta^2}{\langle I\rangle}\right) - \beta^2 - \frac{C}{Z_2} - \frac{\delta}{2}\right], \tag{2.7}$$

where $\gamma^{-1} = \sqrt{1 - v^2/\beta^2}$ is the Lorentz factor, $\beta = v/c$ is the particles velocity relative to the speed of light ($c = 299792458$ m/s), and I is the mean ionization potential of the medium (discussed below). Figure 2.7 demonstrates equation (2.7) for several ions of interesting in this study.

The stopping power equation can be simplified for ease of analysis by using the definition for the Bohr electron radius, $r_0 = e^2/mc^2$, and combining the relativistic terms in the bracket, $F(\beta) = \ln[2mc^2\beta^2/(1-\beta^2)] - \beta^2$;

$$\frac{dE}{dx} = \frac{4\pi r_0^2 m_e c^2 Z^2 z}{\beta^2}\left[F(\beta) - \ln\langle I\rangle - \frac{C}{Z_2} - \frac{\delta}{.}2\right] \tag{2.8}$$

The prefactor terms can be further reduced to the constant, $\kappa = 4\pi r_0^2 m_e c^2 = 0.000509$ eV/10^{15}atoms cm^2. Stopping units of MeV/cm are quickly found by multiplying κ with N$_A$/$10^{21}A$, where N$_A$ is Avagadro's number (6.022$\times 10^{23}$) and A is the atomic weight of the target. For radiobiology measurements where path length is measured at the cellular level, approximately 10^{-6}, the stopping power is given in units of keV/μm. In this case, stopping units are found with κ = (0.1)$\times$N$_A$/$10^{21}A$

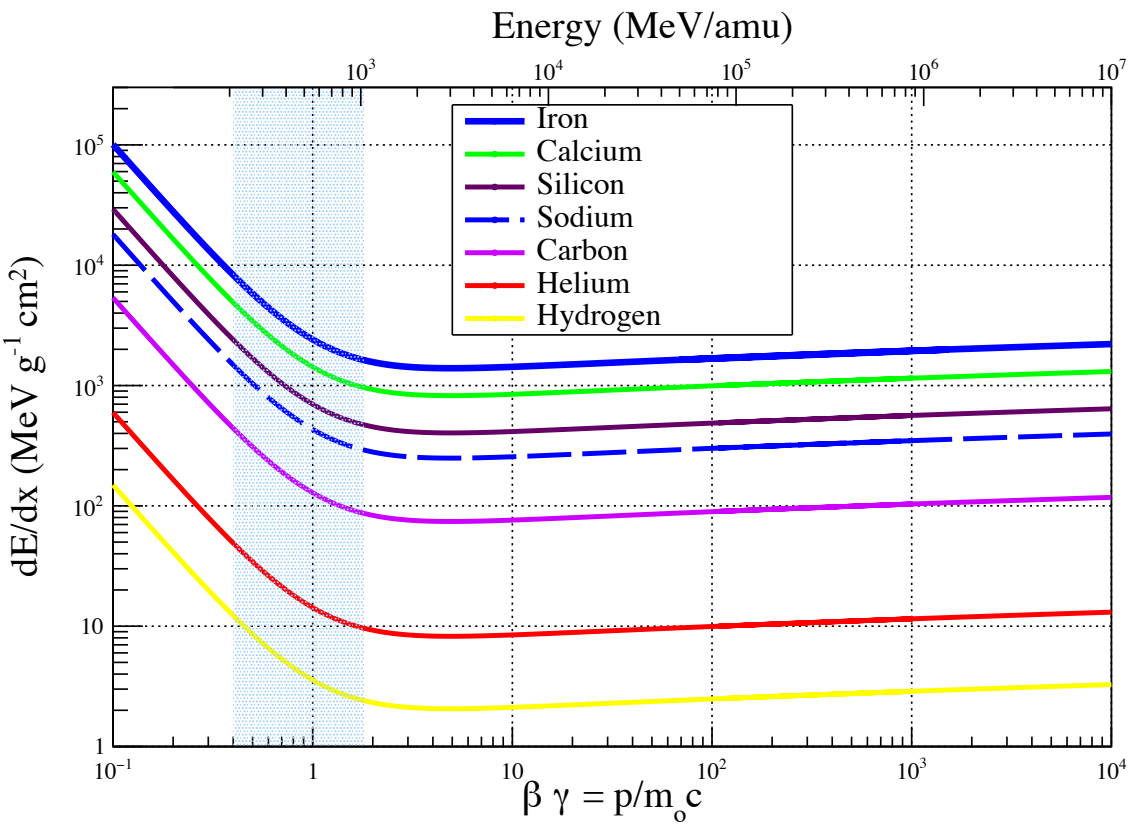

Figure 2.7: **Mass stopping power of polyethylene (C_2H_4) on hydrogen ($Z = 1$), helium ($Z = 2$), silicon ($Z = 24$), calcium ($Z = 20$) and iron nuclei ($Z = 26$).** The ordinate is the mass stopping power, a useful for expressing the rate of energy loss of a charged particle per g cm^{-2} of the traversed medium and is detemined by dividing equation (2.7) by the density of polyethylene (0.94 g/cm^3). The lower abscissa is the nuclei's momentum while the upper abscissa defines the respective energy. A shaded box defines the momentum and energy range of interest for this study (e.g., $0.1 \leq \beta\gamma \leq 0.9$ and 100 MeV/n $\leq$ E $\leq$ 1 GeV/n).

$$\frac{dE}{dx} = \kappa\, N_A \frac{Z}{A}\frac{z^2}{\beta^2}\, L_0(\beta)\; MeV/cm, \tag{2.9}$$

where the *stopping number*, $L_0(\beta)$, contains the relativistic terms found in $F(\beta)$ and the correction factors determined by Fano. Equation (2.9) can be expanded around powers of z^2, providing higher order corrections,

$$\frac{dE}{dx} = \kappa\, N_A \frac{Z}{A}\frac{z^2}{\beta^2}\, \Big[L_0(\beta) + zL_1(\beta) + z^2 L_2(\beta)\Big]. \tag{2.10}$$

The higher order terms, $L_1(\beta)$ and $L_2(\beta)$, are commonly referred to as the *Barkas-Anderson* and

Block correction factors [100]. Neither of these corrections are significant (less than 1%) for primary energies $E > 5$ MeV/n, thus outside of the scope of this research. Further discussion of the mean ionization potential, and the correction parameters, including C/Z_2, δ/2, will be discussed in detail in the following sections

The primary stopping number, L_0, contains the most significant corrections to the stopping power of a medium;

$$L_0 = \ln\left(\frac{2mc^2\beta^2}{(1-\beta^2)}\right) - \beta^2 - \ln\ \langle\ I\ \rangle - \frac{C}{Z_2} - \frac{\delta}{2}. \tag{2.11}$$

Each of the correction terms, I, C/Z_2, and $\delta/2$, are dependent on the properties of the target material; the later two, however, are have additional significant dependence on the velocity, β, of the primary ion.

The mean excitation potential, I, describes the energy transfer during a charged particle/atomic electron collision that produces an excitation event. All of the atomic electrons are assumed to participate in the energy exchange. For a given material, I is defined as [104],

$$\ln\langle I\rangle = \sum f_n \ln E_n, \tag{2.12}$$

where f_n and E_n are the dipole oscillator strength and the excitation energy for the transition from the ground state to the *n*th excited state. The natural logarithm of I can be expanded as the dipole oscillator strength for the *n*th energy level,

$$f_n = \frac{2mE_n}{\hbar^2 Z_2}\left|\sum_j \langle n|x_j|0\rangle\right|^2. \tag{2.13}$$

In principle, the mean excitation potential of a material can be obtained from equation (2.12). However this can be cumbersome since the oscillator strengths for a desired energy range are generally not well known. This is especially true in the 10 eV to 1 keV excitation energy range of most elements, where the knowledge of f_n is poorly understood. Using a statistical approach, Bloch

demonstrated that the I of an atom was proportional to it's atomic number, Z, by some constant K, or $I \propto KZ$ [105]. Subsequent attempts by Bloch, Barkas and Berger, Sternheimer, and Dixon were made to quantify the value of K for different media using experimental results.

Discrepancies remain between the theoretical estimates and experimental measurements of I. Additionally, there are no systematic values of both experimental and theoretical values of I for all atomic elements. This makes it difficult to determine the exact contribution of I and how the variation will affect the outcome for this study. However, the most recent by Turner provides a close approximation using a semi-empirical equation [6]:

$$I \cong \begin{cases} 19.0\ eV & Z = 1; \\ 11.2 + 11.7Z\ eV & 2 \leq Z \leq 13; \\ 52.8 + 8.71Z\ eV & Z > 13. \end{cases} \tag{2.14}$$

When the material is a compound or mixture, I can be calculated by simply adding the separate contributions from the individual constituent elements. If there are N_i atoms cm^{-3} of an element with atomic number Z_i then the mean excitation energy I_t for the compound can be found with,

$$n \ln I_t = \sum_i N_i Z_i \ln_i . \tag{2.15}$$

When a relativistic particle passes through a solid material, its energy loss has been shown experimentally to be slightly less than what is predicted by equation (2.7). This divergence between the theoretical predicted and measured values of stopping power was found to increase at higher energies and in denser media. For 1 GeV protons traversing an emulsion solution, the measured stopping power was less than predicted by approximately 1%. This disparity between measured and predicted values was even greater for 8 GeV protons where the difference reached upwards of 7% for a graphene solid [106].

It was determined by Fermi, and later expanded upon by Sternheimer and Fowler, that the original derivation of the stopping power equation (2.7) ignored the dielectric properties of the

medium [107, 108, 109, 110, 111]. In dense materials, the dielectric polarization of the material alters the particle's fields from their free space values and distorts the assumption that the particles approach of an lattice atom or molecule can be readily defined. For a neutral target medium the recoil of orbital electrons will result in a restoring Coulomb force that drives the charge density to oscillate equally to the plasma frequency. This correction reduces the rise in stopping power from approximately $\ln \gamma^2$ to $\ln \gamma$ for particles where $\beta\gamma$ greater than or equal to 1. At these relativistic energies, the density effect correction has the form,

$$\frac{\delta}{2} = \ln(\beta\gamma) + \ln\left(\frac{I}{\hbar\omega_p}\right) - \frac{1}{2}, \tag{2.16}$$

where ω_p is the plasma frequency of the medium.

Sternheimer demontrated that for intermediate energies, the density effect can be determined with,

$$\frac{\delta}{2} = \frac{\delta_{\text{high}}}{2} - \frac{a}{2}\,(X_1 - X)^m, \tag{2.17}$$

for $X_0 < X < X_1$. Here $\delta_{\text{high}}/2$ is given by Equation 2.16 and the constants X_0, X_1, a, and m are the Sternheimer density effect parameters experimentally determined by Sternheimer et.al. [112]. These values for elemental substances with $Z \leq 97$ along with 180 chemical compounds can be found in Sternheimer et. al., 1984 [112].

In contrast, the shell correction corrects for the assumption that the primary's velocity is much larger than the bound electron's orbital velocity. As the primary ions velocity decreases from relativistic energies, the interaction with bound electrons is not accounted for in the equation and minimizes their contribution to the stopping power. Measured values of the shell correction term, C/Z_2, provides a correction to the failure of the stopping power equation at low energy and velocity ions. Experimental measurements have shown a correction as high as 6% for protons with energies in the range of $1 - 100$ MeV.

Fano first approximated that the values of C/Z_2 could be determined by using the local density approximation, which assumes a particle interacting with a free gas of various densities [104]. The

shell correction term are determined by first calculating the stopping of a charged particle in a medium, and then extrapolating the values of C/Z_2 by inverting equation (2.7),

$$\frac{C}{Z} = \left(\frac{dE}{dx}\right)_{\text{cacl}} \frac{4\pi e^4 Z\, z^2}{m_e v^2}\Big[\ln\left(\frac{2mv^2}{\langle I\rangle}\right) - \ln(1-\beta^2) - \beta^2 - -\frac{\delta}{2}\Big], \tag{2.18}$$

where $(dE/dx)_{\text{cacl}}$ is the calculated stopping power for the specific ion, energy and material. Equation (2.18) provided reasonable approximations of the shell correction for primary energies approximately greater than 5 MeV/n. Bichel addressed this problem by accounting for orbital bonding in the target material and demonstrated that the function C could be approximated with for $\beta\,\gamma$ greater than 0.13,

$$\begin{aligned} C = &(4.2238\times10^{-7}\beta^{-2}\,\gamma^{-2} + 3.048\times10^{-8}\beta^{-4}\,\gamma^{-4} - 3.8106\times10^{-1}\beta^{-6}\,\gamma^{-6})\; I^2 \\ &+(3.85802\times10^{-9}\beta^{-2}\,\gamma^{-2} - 1.66799\times10^{-10}\beta^{-4}\,\gamma^{-4} + 1.57955\times10^{-12}\beta^{-6}\,\gamma^{-6})\; I^3. \end{aligned} \tag{2.19}$$

Ziegler has shown that while Bichel's approach correctly approximates the shell correction for the lower energies, the accuracy for primary energies greater than 5 MeV/n diverges with experimental observations.

Using Equations (2.18) and (2.19) requires prior knowledge of the mean excitation potential, I, for the medium under consideration.

2.4 Discussion On Energy Loss

Given the energies of interest in this study, it is reasonable to conclude that the mean excitation potential, I, provides the largest opportunity to perturb the medium's properties in order to instigate specific changes in the emerging particle spectra that more closely model the desired field. It describes how easily a target material can absorb the kinetic energy imparted from the projectile through electronic and vibrational excitation. Unlike the density and shell corrections, whose relative contribution to stopping is dependent on the projectile's energy and/or atomic charge, I is characteristic of the target material only. It has no dependance on the properties of the projectile ion.

Since the contribution of I to stopping is logarithmic, small changes in its value do not produce major changes in the stopping cross section [113]. This provides an opportunity to make fine adjustments to the energies of the emerging particles by making perturbations around the measured values of the mean excitation potential for material under considerations. Equation (2.14) shows that I can be readily approximated to a high degree of confidence. The measured values of I for atomic elements up to $Z = 50$ is shown in Table B.1. As expected, the values of the mean excitation potential increase with atomic number.

It should be emphasized that the stopping power equation (equation (2.7)), is a determination of the *mean* energy loss of a ion crossing a material. For detectors of moderate thickness Δx such scintillators, the energy loss probability distribution f(δ;β γ,x) is adequately described by the Landau distribution [114]. The most probable energy loss is found with,

$$\Delta\, E = \frac{\kappa Z \Delta x}{2A\beta^2}\left[\ln\frac{2mc^2\beta^2\gamma^2}{I} + \ln\frac{\kappa Z \Delta x}{2A\beta^2 I} + j - \beta^2 - \delta(\beta\gamma)\right], \tag{2.20}$$

Finally, the LET has been described as the linear rate of energy lost from the heavy charged particles traveling through a medium. LET often refers to the stopping power of a medium[4], therefore, theoretically, LET is equivalent to the stopping power and can be written [6],

$$LET = \frac{dE}{dx}, \tag{2.21}$$

Unrestricted stopping power or unrestricted LET, LET_∞, is defined by the International Council on Radiation Units (ICRU) as the linear rate of energy loss due to both soft and hard collisions at all energy ranges. The LET_∞ equals total stopping power [18].

The goal of this research will focus on methods to reproduce the distribution of the LET_∞ found in the GCR as shown in Figure 1.2. The LET distribution found in space is unique and presently cannot be accurately replicated during ground-based radiation studies. It is important to understand

[4]The energy lost by charged particles transversing a medium is not always equal to the energy absorbed. The restricted stopping power, LET_Δ, usually expressed in units of keV/μm, is defined as the linear rate of energy loss due to collisions where the energy loss does not exceed a cutoff value Δ

and reproduce a space radiation-like analog because it is directly associated with radiation risks.

2.5 Scattering Cross Section

As mentioned above, for small $r_{\min}$, there is a probability of a nuclear reaction between the nucleus of the charged particle and target atoms. The probability is described with the interaction cross section, σ. The cross-section can be described as the probability for a reaction or interaction to occur. Assuming an incident beam of particles travels along the z-axis, with momentum, $p = \hbar k$, the particles can be written as a superposition of spherical waves or,

$$\psi_{\text{inc}} = Ae^{ikz} = A\sum_{l=0}^{\infty} i^l(2l+1)j_l(kr)\ P_l(\cos\theta), \tag{2.22}$$

where radial portion, $j_l(kr)$ are spherical Bessel functions that are the solution to the Schrodinger wave equation, and angular $P_l(\cos\theta)$ are the Legendre polynomials. The relation between the particle momentum, p, the impact parameter, b, and the relative angular momentum would be $l\hbar = pb$ or $b = l\hbar/p = l\ \lambda_{\text{dB}}$. Here $\lambda_{\text{dB}} = k^{-1}$ is the reduced de Broglie wavelength. The interaction between the incident particles and target nucleus is limited to integral multiples of the angular momentum. This allows the interaction area to be divided into zones corresponding to specific values of angular momentum, $A = (2l+1)\pi\lambda_{\text{dB}}^2$. Estimation of the maximum impact parameter for nuclear scattering can be taken as the sum of the incident and target nuclei, or $R = R_{\text{inc}} + R_{\text{tar}}$ which leads to a total cross section of,

$$\sigma = \sum_{l=0}^{R/\lambda_{\text{dB}}} (2l+1)\pi\lambda_{\text{dB}}^2 = \pi(R + \lambda_{\text{dB}}^2). \tag{2.23}$$

When the particle is far from the nucleus, the radial solutions to the Schrodinger wave equation can be expanded,

$$j_l(kr) \approx \frac{\sin(kr - 1/2\ l\pi)}{kr} = i\ \frac{e^{-i(kr-l\pi/2)} - e^{i(kr-l\pi/2)}}{kr},\ \ (kr \ggg l), \tag{2.24}$$

which gives for the incident particle wave equation,

$$\psi_{\rm inc} = \frac{A}{kr}\sum_{l=0}^{\infty} i^{l+1}(2l+1)\,[e^{-i(kr-l\pi/2)} - e^{i(kr-l\pi/2)}]\,P_l(\cos\theta), \tag{2.25}$$

where the first term in the bracket represents an incoming spherical wave, and the second term (*e.g.* e^{ikr}) is the outgoing wave scattered off the target nucleus. Interactions with the target nucleus will be seen with either a change in phase or amplitude of the scattered wave. The loss in amplitude indicates reactions other than elastic collisions, such as an inelastic scattering or other nuclear reaction. These are reaction *channels* where the scattered particles have momentum other than $p = \hbar k$. Reactions between the incident particles and the target nucleus may the elastic channel or through the many inelastic channels. In some cases, specific reaction channels are closed to interacting particles and nuclei if there is not enough energy or angular momentum to allow a specific configuration to be reached.

To account for these reactions, a complex coefficient, η_l, is proposed for the outgoing term of the wave equation for the incident particle giving,

$$\psi = \frac{A}{kr}\sum_{l=0}^{\infty} i^{l+1}(2l+1)\,[e^{-i(kr-l\pi/2)} - \eta_l\, e^{i(kr-l\pi/2)}]\,P_l(\cos\theta), \tag{2.26}$$

where the wave equation now represents the scattered terms and the superposition of the incident and scattered waves, $\psi = \psi_{\rm inc} + \psi_{\rm sc}$. Subtracting this from equation (2.25) gives the wave equation for the particles scattered off the target nucleus,

$$\psi_{\rm sc} = \frac{A}{2k}\frac{e^{ikr}}{r}\sum_{l=0}^{\infty} i(1-\eta_l)(2l+1)\,P_l(\cos\theta), \tag{2.27}$$

where we can now determine the current density for the *elastic* scattered particles and subsequently the corresponding cross section. The current density is found with,

$$
\begin{aligned}
j_{\mathrm{sc}} &= \frac{\hbar}{i2m}\left(\psi_{\mathrm{sc}}^{*}\frac{\partial\psi_{\mathrm{sc}}}{\partial r} - \psi_{\mathrm{sc}}\frac{\partial\psi_{\mathrm{sc}}^{*}}{\partial r}\right) \\
&= |A|^2\frac{\hbar}{4mkr^2}\left|\sum_{l=0}^{\infty} i(1-\eta_l)(2l+1)\,P_l(\cos\theta)\right|^2,
\end{aligned}
\tag{2.28}
$$

which leads to the differential cross section,

$$
\frac{d\sigma}{d\Omega} = \frac{1}{4k^2}\left|\sum_{l=0}^{\infty} i(1-\eta_l)(2l+1)\,P_l(\cos\theta)\right|^2. \tag{2.29}
$$

The total cross section can be found by restricting the Legendre polynomials to orthonormal states satisfying,

$$
\int P_l(\cos\theta)\,P_{l'}(\cos\theta) = \frac{4\pi}{2l+1}, \tag{2.30}
$$

for all $l = l'$ and zero otherwise. This immediately reduces to the total cross section for the elastically scattered particles incident on a target nucleus,

$$
\sigma_{\mathrm{sc}} = 4\pi\lambda_{\mathrm{dB}}\sum_{l=0}^{\infty}(2l+1)\,|1-\eta_l|^2. \tag{2.31}
$$

If $|\eta_l| < 1$, processes other than elastic scattering have occurred, making equation (2.31) not valid. All of the non-elastic processes can be grouped into a term referred to as the *reaction cross section*, σ_r. In order to determine σ_r, the rate at which particles are disappearing from the elastic reaction channel with wave number k. This can be done by using equation (2.26) to determine the difference between the incoming and outgoing particle currents.

$$|j_{\rm in}| - |j_{\rm out}| = |A|^2 \frac{\hbar}{4mkr^2} \Bigg\{ \Big| \sum_{l=0}^{\infty} i^{l+1}(2l+1)\, e^{il\pi/2}\, P_l(\cos\theta) \Big|^2 - \Big| \sum_{l=0}^{\infty} i^{l+1}(2l+1)\, \eta_l e^{il\pi/2}\, P_l(\cos\theta) \Big|^2 \Bigg\}, \tag{2.32}$$

which gives the reaction cross section,

$$\sigma_{\rm r} = \pi \lambda_{\rm dB}^2 \sum_{l=0}^{\infty} (2l+1)\,(1 - \Re[\eta_l]), \tag{2.33}$$

and the *total* cross section is now determined with $\sigma_{\rm t} = \sigma_{\rm sc} + \sigma_{\rm r}$,

$$\sigma_{\rm t} = 2\pi \lambda_{\rm dB}^2 \sum_{l=0}^{\infty} (2l+1)\,(1 - \Re[\eta_l]). \tag{2.34}$$

2.6 Discussion on Reaction Cross-Sections for Heavy Ions

For this study, emphasis is on the reaction cross-sections, σ_r, that are unique for heavy-ion interactions. A heavy ion reaction is considered low energy if the primary energy is less than the Coulomb barrier (e.g., approximately $\leq$ 10 MeV/n). The *intermediate* nuclear reactions typically occur for primary energies $20 < E \leq 250$ MeV/n and a *high energy* reaction if the primary's energy exceeds the Coulomb barrier and approaches the rest mass of the nucleon, approximately 938 MeV/n.

The distinction between these different classifications of nuclear reactions is the processes of nucleon-nucleon interactions between the primary ion and target nucleus. During low-energy reactions, the nucleon(s) of the primary ion interact with the mean nuclear force associated with the target nucleus. In contrast, high-energy nuclear reactions, the primary interest of this research, the primary-target nucleons interact individually as nucleon-nucleon collisions. This is apparent when considering the de Broglie wavelength of 10 MeV protons compared to 1 GeV protons. For the low energy, 10 MeV proton, $\lambda = 9$ fm, while the much more energetic 1 GeV proton wavelength

is $\lambda = 0.73$ fm. Given that the average spacing of atomic nucleons is approximately 1.2 fm, the low-energy 10 MeV protons interact with several nucleons at once, while the 1 GeV protons interact with individual nucleons.

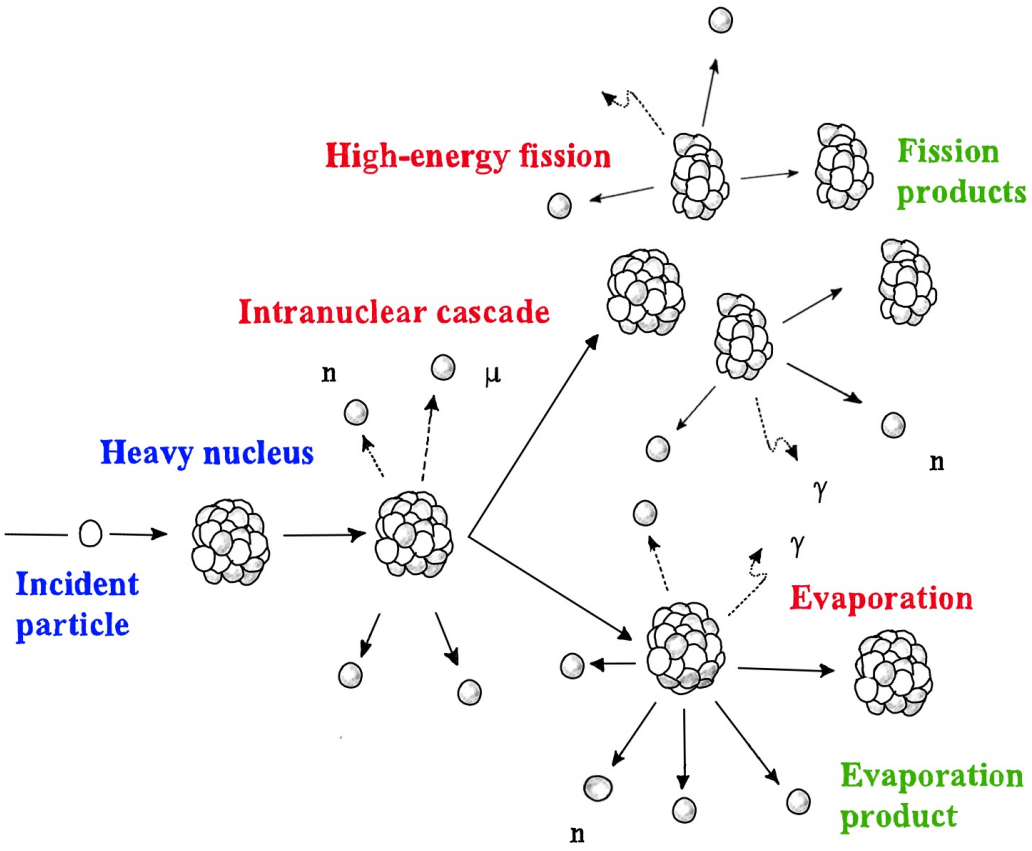

Figure 2.8: **Stages of the spallation reaction for nuclear interactions.** Spallation reaction occurs when a projectile interacts with target's atomic nuclei and results in the emission of hadrons and/or lighter fragments.

High energy nuclear reactions dominated by nucleon-nucleon collisions result in a continuous distribution of product masses that range from the primary ion mass number to very low values of A. Three regions can be identified in the distribution of fragment yields. One region is centered around $A_{\mathrm{p}}/2$ and consists of products of the fission of the projectile nucleus. The larger fission remnants

(e.g., $A_{frag} \geq 2/3\ A_p$) typically are from spallation. A spallation reaction occurs when a projectile interacts with target's atomic nuclei and results in the emission of hadrons and/or lighter fragments. A primary ion knocks out several nucleons in a series of two-body collisions, subsequently leaving behind a highly excited heavy nucleus. The excited nucleus decays by the evaporation of charged particles and neutrons, forming a continuous distribution of progeny ranging downward in atomic mass (A) from the primary's mass number. Spallation occurs in two stages, (1) intra-nuclear cascade (INC), and (2) de-excitation as shown in Figure 2.10.

The INC occurs swiftly, over a time period of approximately 10^{-22} seconds, where the projectile loses (or gains) energy through interactions with the individual nucleons in the target nucleus resulting in a cascade of nucleon-nucleon collisions. The energy threshold for an INC producing a particular species increases with mass. Pions are typically produced at MeV energies with heavier hadrons produced at higher energies (MeV - GeV) and particles participate in the INC process. Excited intra-nuclear particles can obtain enough energy to escape the nucleus are emitted approximately in the direction of the incident projectile. The remaining energy is distributed among the remaining nucleons, leaving the nucleus in a highly excited state. There is no sharp separation of the INC and de-excitation stages and the transition defined by *pre-equilibrium emission*. During the transition, fragmentation of the target nucleus or the projectile ion into nuclei of relatively small charges or complete breakup into individual particles occurs, especially for higher energy projectiles and heavy-ion collision.

For the lowest mass numbers ($A_{frag} \leq 1/3\ Ap$), one observes another group of fragments that are termed to be intermediate mass fragments (IMFs). These fragments are the result of very highly excited remnants of the most head-on collisions occurring by sequential particle emission or nuclear disintegration, multi-fragmentation. The cross-section for nucleon-nucleon scattering varies inversely with the primary's energy, thus at very high energies, the cross section may become small enough so that some nucleons pass through the nucleus without any collisions. This phenomenon is referred to as a *transparent* nucleus.

At very high projectile energies, a number of observations are interpreted in terms of a simple

geometric model named the *abrasion-ablation*, or *fireball*, model. In the abrasion-ablasion model, the incoming primary shears off a section of the target which corresponds to an overlap of the primary and target nucleus, the "abrasion" step. Any regions not overlapping are assumed to be left essentially undisturbed and unheated. These are the spectators to the collision. In the overlap region, the "participants form a fireball" that decays with the release of nucleons and fragments. The fragmented target nucleus is assumed to have a region of now extra exposed surface area where an excitation energy, corresponding to the surface area term of the semi-empirical mass equation of approximately 1 MeV per excess fm^2 of surface area. As the excited nucleus relaxes, the excess surface energy becomes available as excitation energy and subsequently in the emission of nucleons and fragments, the "ablation" step [39].

The use of this simple model for high-energy nucleus-nucleus collisions provides a general categorization of energetic nucleus-nucleus collisions as either peripheral or central. Peripheral reactions have large impact parameters and small momentum transfer. These reactions, producing large spectator fragments, are referred to as fragmentation reactions. These reactions are of primary interest in this research and the abrasion-ablation model will be the focus for determining fragment cross sections.

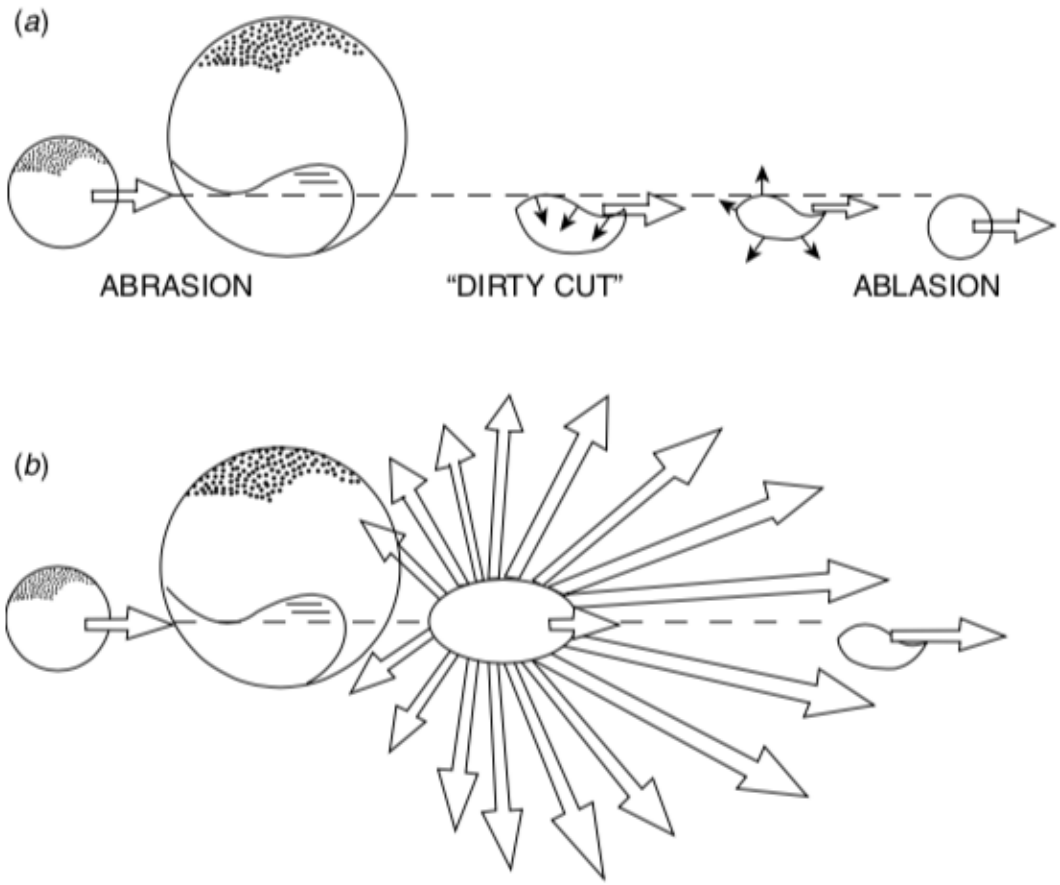

Figure 2.9: **Abrasion-ablation model for high energy nuclear interactions.** Incoming primary ions shears off a section of the target which corresponds to an overlap of the primary and target nucleus, the "abrasion" step. In the overlap region, the "participants form a fireball" that decays with the release of nucleons and fragments. As the excited nucleus relaxes, the excess surface energy becomes available as excitation energy and subsequently in the emission of nucleons and fragments, the "ablation" step. Figure reprinted with permission from Loveland et al., Reference [98].

2.7 Neutrons

It is convenient to divide neutron fields into energy categories: thermal, intermediate, and fast neutrons. Thermal neutrons display a Maxwell-Boltzman distribution of thermal motion that is characteristic of the temperature of the medium in which they exist. Their most probable kinetic energy at 2° is $E = 0.025$ eV. Typically, any neutron with energies below 0.5 eV are referred to as thermal. Neutrons with energies above the thermal cutoff of 0.5 eV but below 10 keV are referred

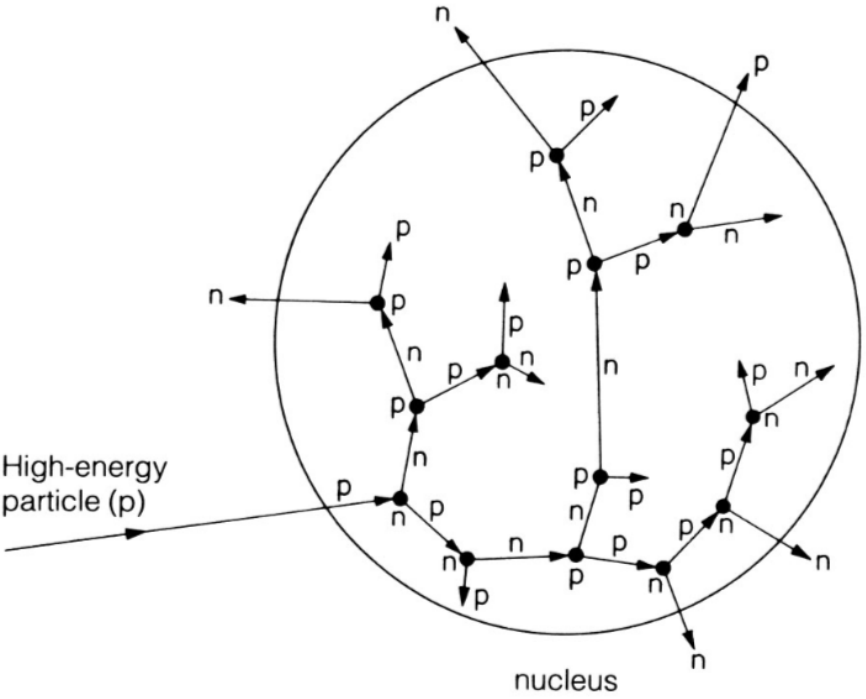

Figure 2.10: **Intranuclear cascade of spallation reactions**. The initial stages of spallation reactions where a primary ion knocks out several nucleons in a series of two-body collisions leaving behind a highly excited heavy nucleus. Figure reproduced with permission from Loveland et al., Reference [98].

to as intermediate-energy neutrons. Fast neutrons cover the energy range from 10 keV and higher.

A neutron will move through material along a straight line with a constant energy until it interacts with a nucleus and induces a nuclear reaction. Neutron attenuation follows an exponential law; written in terms of an energy-dependent attenuation length, μ_{E} we have,

$$I = I_0 e^{\mu_{\mathrm{E}} x}, \tag{2.35}$$

where x is a linear dimension and I_0 is the incident intensity. The attenuation length is the inverse of the mean free path, λ, and is proportional to the total nuclear reaction cross section,

$$\mu_{\mathrm{E}} = \frac{1}{\lambda_E} = N_0 \sigma_{\mathrm{Total}}(E), \tag{2.36}$$

where N_0 is a constant that gives the total number of nuclei per unit volume in the material. The total nuclear reaction cross section is a characteristic of each isotope in the absorbing material and has the dimensions of an area.

Neutrons can interact with matter via a number of different reactions, depending on their energy. The following are among the most important of these reactions:

- Elastic scattering, $A(n,n)A$, the principal interaction mechanism for neutrons.
- Inelastic scattering, $A(n,n')\ A(n,n')A^{\star}$, where the product nucleus A is left in an excited state. To undergo inelastic scattering, the incident neutron must have sufficient energy, generally about 1 MeV or more, to excite the product nucleus.
- Radiative capture, $A(n,\gamma)A+1$. This cross section shows a $1/n$ energy dependence and is important for low-energy neutrons.
- Fission, $A(n,f)$, occurring typically at thermal energies but also at energies where the neutron binding energy exceeds the fission barrier height for fissile nuclei.

Neutrons and other non-charged particles were not included in our LET calculations primarily because they were not included in the flight measurement data and, in this work, all effort was made to accurately reproduce these data sets. Spallation neutrons are typically present. However, they should not be included without reliable and accurate measurements from spaceflights – data that are currently unavailable, as such measurements are exceedingly difficult to perform. Charged particles move (mostly) along a straight path losing energy according to equation (2.7). Knowing their energy, ion type, and corresponding LET provides enough information to evaluate the biological impact as the charged particle propagates from the skin surface and through soft tissue. In contrast, neutron propagation is far more sporadic. During any interaction, a neutron may deposit only a small fraction, or even all of its energy, into the medium. For neutrons, LET refers to the energy deposited in the medium by the secondary charged particles generated by neutrons. Therefore, an accurate measurement of the intravehicular neutron spectrum is needed before the neutron contribution can be distinguished from the charged particle spectrum.

3. DEVELOPMENT OF MODEL FOR GROUND-BASED SIMULATION OF SPACE RADIATION

The method in this dissertation leverages currently available technologies to provide an enhancement to current ground-based analogs of the space radiation environment by reproducing the measured intravehicular LET spectrum. A moderator block is placed between a biological sample and an heavy-ion accelerator beam in order to create modest amounts of fragments or varying energies and ion species. A moderator of thickness l will be chosen to correspond with the desired transmission of primary nuclei needed in the final spectrum, where 1000 MeV/n iron (^{56}Fe) has been chosen for the primary beam as it is the heaviest nuclei significantly contributing to absorbed dose in the GCR environment. GCR ions lighter than iron will be produced by interaction of the projectile beam in subsequent, multiple n-targets of suitable thickness.

The thickness and material of each layer will be chosen in order to instigate energy loss and spallation processes that result in the desired distribution of emerging ions and energies. The key factor in this approach is to match a single target thickness to a desired range of LET. The proper fluence of particles required for each thickness will be determined and the proposed moderator designed accordingly. An example is shown in Figure 3.1.

3.1 Theory & Model

For an initial field, $f(x)$, impinging on a moderator of material, *M*, the resultant emerging field, $f'(x)$, is dependent on the composition of the moderator material and the incident ion and its energy. The fundamental quantities are the reaction cross sections, which are directly related to the probability for producing a particular fragment species as a function of the target material [115]. The effective stopping and fragmentation cross sections for heavy charged nuclei increases with decreasing atomic number [19, 115]. Theses will play an important role in selection of the moderator material.

Collisions between the ^{56}Fe ions and the moderator nuclei will result in projectile and target

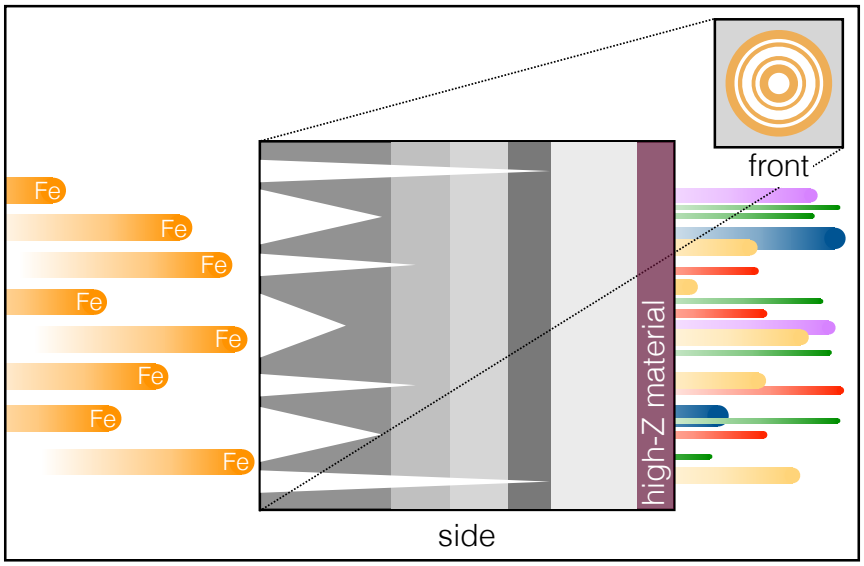

Figure 3.1: **Schematic of the moderator block designed to emulate specific space radiation spectra.** A primary beam of ^{56}Fe (left) is selectively degraded with a carefully-designed moderator block to produce a desired distribution of energies and ions (represented by the colorful lines on the right-hand side). To preferentially enhance fragmentation and energy loss, cuts (white sections on the left-hand side) are performed in the moderator block made up of different materials (depicted by different shades of gray). Before the spallation products exit the moderator block, a high-Z material layer is added for scattering. The inset shows the circular beam spot, as well as the symmetric cuts made into the moderator block.

fragments and recoil products. The remaining ^{56}Fe ions continue with their initial velocity, losing energy by electromagnetic interactions, and because energy is lost and the LET depends on the inverse square of velocity, ions with sufficient range to fully traverse the moderator will emerge with higher LET [115]. The primary ^{56}Fe particles and the heavy projectile fragments represent the high-range LET components and the mid-range LET components of the GCR. The lighter fragment products will provide the contribution to the mid and low-range LET components of the GCR.

Nuclear spallation processes will create modest amounts of fragments that result in an emerging particle field consisting of nuclei with a LET less than 250 keV/μm. As the thickness of the moderator layers are increased, more fragments are produced and more energy is lost in the moderator. The thickness and type of material of each layer will be chosen so that an impinging field, $f(i, E)$, of ions, i, with energies, E, will result in the desired emerging field, $f'(i, E)$, so that:

$$f'(i,E) = g(n,I,C,\delta,\sigma)f(i,E), \tag{3.1}$$

where $g(n,I,C,\delta,\sigma)$ describes the medium and n, I, C, δ, and σ are the electron density, mean excitation potential, shell correction, density effect, and scattering cross-section that are intrinsic material properties affecting charged particles transversing a medium. The correct fluence of particles required for each layer (and thickness) will be determined using Monte Carlo methods. The final moderator block will be designed so that the addition of each layer will result in a final field, $F(i,E)$, such that:

$$F(i,E) = \sum_n g_n(n,I,C,\delta,\sigma)f(i,E), \tag{3.2}$$

where the function, $F(i,E)$, closely simulates the intravehicular GCR spectrum measured on previous spaceflights.

This final moderator block is placed in front of a 1 GeV/n iron particle beam and nuclear fission processes will create modest amounts of fragments that result a complex mixed field of particle nuclei with $1 < Z < 26$ and LETs $\leq$ 250 keV/μm.

3.2 Methods

3.2.1 Primary Beam

As discussed, the ion species and energy of the primary ion was chosen to be 1 GeV/n ^{56}Fe. This is also the dominant ion and energy of the dose-equivalent distribution that is currently available at the NSRL. This energy and ion choice also has ranges much greater than the expected shorter depths of the moderator block (approximately 25 cm). This provides a means of ensuring that the effects of fragmentation dominate while instigating a positive dose attenuation and minimal change in the LET of primaries that survive transport through the block. The energy loss of the primary will increases with depth and this begins to counter the expected decrease in average LET caused by fragmentation. As the primary ranges out and velocity decreases, the LET rises sharply at depths that are small compared to the mean free path for a nuclear interaction and the effects of energy

loss outweigh those of fragmentation. Moderator geometry and thickness will need to balance the effects of energy loss and fragmentation. An example of a concept geometry is shown in Figure 3.5

3.3 Material Selection

The selection of the appropriate material was done assuming that the interaction of the primary particle with the atomic lattice results in one of two outcomes: either the primary ion loses energy to the medium or there is generation of smaller progeny nuclei that result from spallation processes. Both of these stochastic outcomes are influenced by the energy and charge of the primary ion, but are also strongly dependent on the properties of the material. The effectiveness of a material to instigate energy loss attenuation and spallation is typically increases with decreasing atomic number, with hydrogen being the most efficient.

The material(s) being considered should also account for the ability to utilize the moderator block at a heavy-ion accelerator facility (e.g., the NSRL) with very minimal changes to the existing beamline infrastructure. This means mass, length, fabrication, and cost will also be a strong consideration. As shown in the previous section, a heavy-charged particle traversing a material will lose energy that can be approximated to a high degree of accuracy using equation (2.7). The material-specific properties that affect stopping power are the electron density, ionization potential, density effect, and shell corrections.

The density effect term only plays an important factor to the stopping power of a medium for particles with energy greater than 1 GeV/n (e.g., 938 MeV and 3.7 GeV/n for proton and helium ions, respectively). Ziegler et.al., demonstrated that the density effect correction for lighter ions like carbon and beryllium is less than 0.5% for protons with kinetic energy less than approximately 3 GeV [100]. It is a reasonable conclusion to assume that the density effect will not be an important criteria for material choice because these exceed the energy of charged particles being considered (approximately $\leq$ 1GeV).

Figures 3.2 and 3.3 show the relative correction of C/Z_2 to the stopping power medium for oxygen and iron ions ($Z = 6$ and $Z = 56$) crossing through water [104, 116, 100]. These indicate that the shell correction contributes mostly to the overall stopping of ions with energies less than 10

MeV and are not a primary focus of this study. Three study cases discussed later in this text will address this issue.

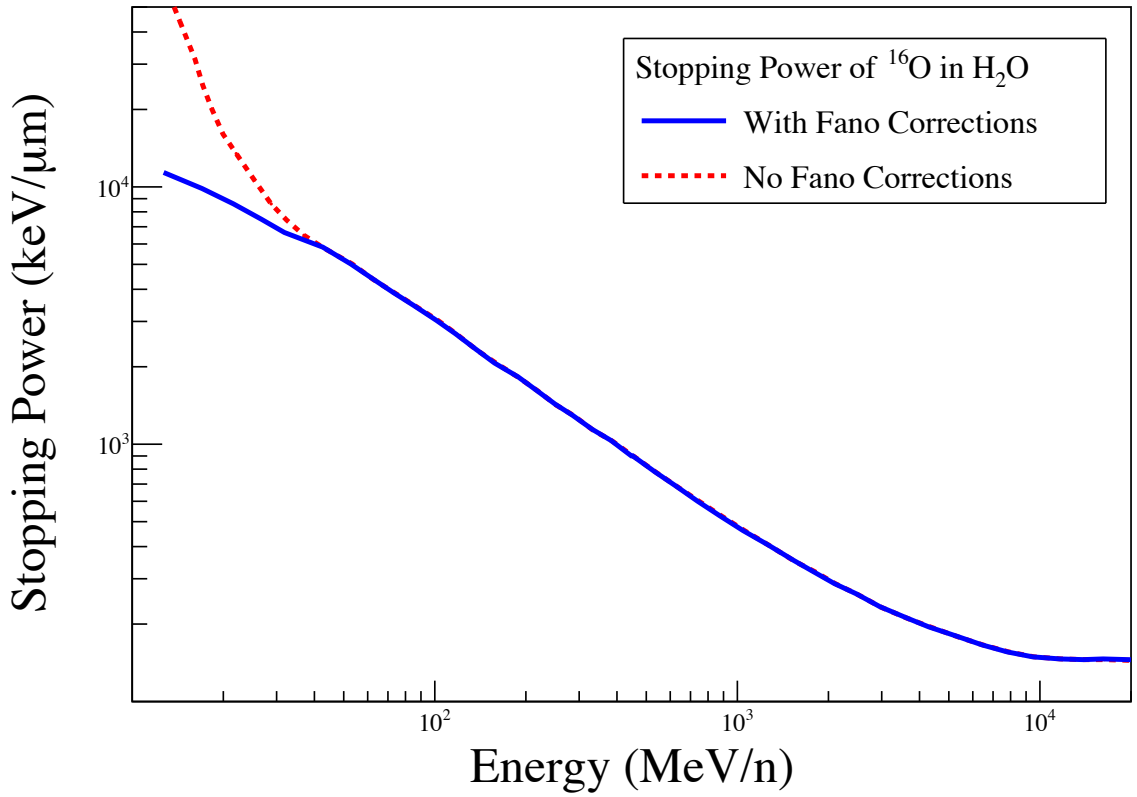

Figure 3.2: **Stopping power equation with and without the shell correction applied for oxygen ($Z = 8$) ions in water.** This demonstrates that no significant contribution for determining stopping power at primary energies greater than approximately 5 MeV/n.

The material selection will thus depend intrinsically on the electron density and the mean excitation energy. Energy loss of medium to high energy particles can then be roughly approximated with $dE/dx \propto z^2/\beta^2$, with the electron density and logarithmic value of the ionizing potential acting as a linear scaling factors. Several values for tissue, polymer, and metal materials are shown in Table B.2. There are noticeable differences in the excitation potential of soft versus hard materials. Tissue, bone and polymer materials have values of I ranging from 57.4 (polyethylene) to as high as

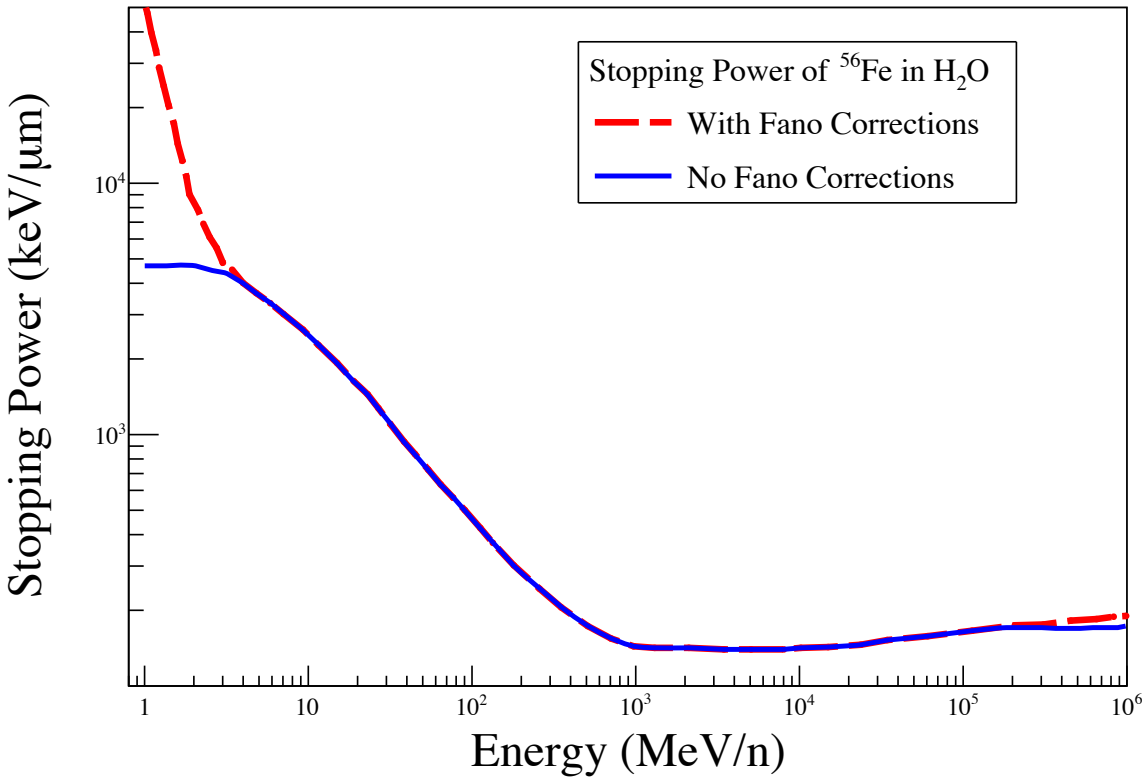

Figure 3.3: **Stopping power equation with and without the shell correction applied for iron ($Z = 26$) ions in water.** This demonstrates that no significant contribution for determining stopping power at primary energies greater than approximately 5 MeV.

79.6 (polyamide).

Additionally, there is a probability of fragmentation of the particle into smaller, lower-energy ions due to spallation processes that result from interactions with nuclei in the material. Predicting the resulting particle species, multiplicity, and corresponding energies is not possible to any high degree of accuracy. The probability for a nuclear interaction to induce a charge-changing spallation can be determined from the primary ion's energy, geometric cross section and mass number, A_P, and the mass number of the nuclei it is interacting with, A_T [17]:

$$\sigma = \pi r_0^2 \left[\sqrt[3]{A_P} + \sqrt[3]{A_T} - \gamma(A_T, A_P, E) \right]^2, \tag{3.3}$$

where γ depends on the energy of the primary ion and is determined by

$$\gamma = 0.2 + A_T^{-1} + A_P^{-1} - \cos\left(0.229E^{0.453}\right)0.292\, e^{-E/792}. \tag{3.4}$$

Polymers, which have a high hydrogen content, are very effective energy absorbers because of the high number of electrons per unit mass and relatively low mean excitation energy. This predicts that a polymers are a suitable candidate material for study since they have a high hydrogen content and sufficient tensile strength (e.g., polyethylene, CH_2, with two hydrogen atoms and one carbon atom per molecule) [117, 118, 119, 120, 100]. Since hydrogen is highly effective, one would expect polyethylene, CH_2, with two hydrogen atoms and one carbon atom per molecule, to be an effective candidate material for the moderator block [121, 122]. Thus, it is reasonable to conclude that, per unit mass, hydrogenous materials stop more of the incident low-energy particles than other materials as well as causing a desired amount of fragmentation of high-energy heavy ions [106].

3.4 Geometry

The design of the target geometry is very important since the LET of the projectile and higher-Z fragments will typically increase more rapidly as the depth of the moderator block increases. Additionally, with increasing moderator block depth, the number of ions available to fragment into lighter ions is depleted by spallation events at shallower points in the target. At moderator depths much greater than the range of the incoming ^{56}Fe primary, the heavy charged fragments begin to range out and their contribution to the LET of the emerging field decreases. At very great depths, the charged particle dose is due to high-energy singularly-charged particles (e.g., protons, charged pions, helium).

In any medium, there is a finite probability for secondary, tertiary, and higher-order generation of nuclear interactions that involve the primary ^{56}Fe ions. The energy loss of the primary and its progeny created by spallation also increase with depth, and this begins to counter the expected decrease in average LET caused by fragmentation. The LET of the primary nuclei and higher-Z fragments typically increase rapidly as the depth of the moderator block increases. As the primary

slows and its energy decreases, the LET rises sharply at depths that are small compared to the mean free path for a nuclear interaction and the effects of energy loss outweigh those of fragmentation. Additionally, as the moderator's depth increases, the number of ions available to fragment into lighter ions is depleted by spallation events at shallower points in the target. At moderator depths much greater than the range of the incoming ^{56}Fe primary, the heavy charged fragments begin to slow and stop, and their contribution to the LET of the emerging field decreases. At very great depths, the charged particle dose is due to high-energy, singly-charged particles (e.g., protons, charged pions, helium, etc.), all of which have very long ranges in polymers (approximately $3 - 4$ m for a 1 GeV proton in CH_2).

The length of travel through a medium can not only positively (or negatively) enhance the number of desired lower-Z ions generated and the energy loss of the primary and secondary ions, it can also affect nuclei yields by depleting the number of high-Z ions still needed. In order to generate the GCR spectrum, the moderator geometry and thickness need to balance the effects of energy loss and fragmentation. This is done by designing the moderator block geometry so that it replicates the attenuation function G for the desired field $F(i, E)$ via $F(i, E) = G\ f[i, E(i)]$. The attenuation G describes the various channels of the moderator block (Figure 3.1) and is a function of the geometry and the intrinsic properties of each material utilized in the moderator design. Each channel or "cut" represents a separate path the primary ions can travel through the block. The diameter, length and material of each cut are chosen to induce specific spallation and energy loss events of the primary ion. This provides a method to selectively induce specific fragmentation and energy losses that result in the emerging field having the desired distribution of emerging ions and energies.

3.4.1 Example Process: Space Shuttle LET

The simulations are performed using the Monte Carlo particle transport simulation software PHITS in order to model particles traversing through thick absorbers and to approximate the desired LET spectrum. The correct fluence of particles required can be determined using data from sources such as satellite measurements, intravehicular measurements during previous space missions, or from peer-reviewed models of the GCR spectrum [123].

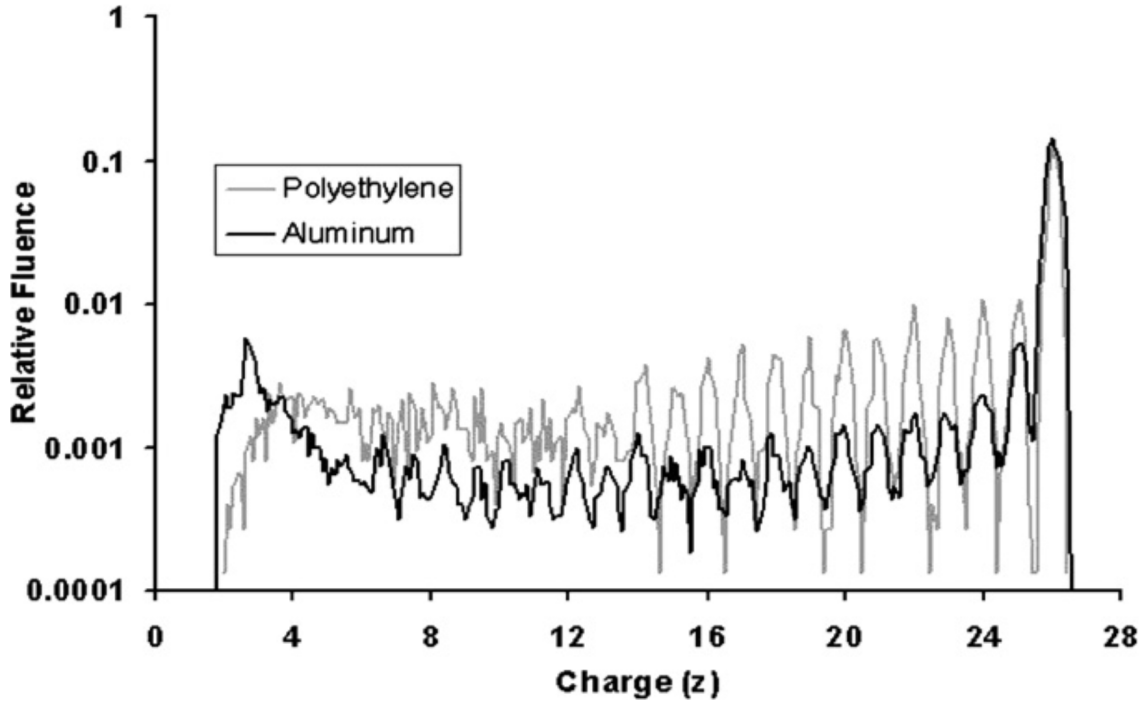

Figure 3.4: **Relative fluence of fragments produced by polyethylene compared to aluminum.** Fragment spectrum from a 1 GeV iron beam on polyethylene and aluminum targets. The higher percentage of progeny fragments with $Z < 26$ indicate that polyethylene is a better choice of materials for creating light fragment particles. Figure reprinted from Guetersloh et. al. 2008 [40], with permission from Elsevier.

PHITS has been previously compared to experimental cross-section data using similar energies and materials. Zeitlin et al., [124, 125] showed that, for large detector acceptance angles, there is good agreement between experimental beam-line measurements of fragmentation cross sections and the simulated outcomes that utilized PHITS to generate the expected progeny fragments and energy loss. More importantly, PHITS can be run in parallel mode and thus take advantage of large-scale multi-core high-performance computing platforms. This allowed for rapid calculations and minimizing statistical variations by using large sample size for each data set. As an example, for just one of the three model cases, 10^6 primary ions were sampled for each layer, typically using 5000-10000 cores in each instance, while generating an average of 2.5 terabytes of data. The total

computation time for each data set is roughly equivalent to 135,000 cpu hours. In each of the PHITS simulations, we have used PHITS version 3.02 and the total reaction cross-sections developed by Tripathi [126, 127, 128]. The Tripathi cross-sections have also been adopted by NASA for modeling charged particle reactions.

An intravehicular LET spectrum measured on the U.S. Space Shuttle, shown in Figure 1.2, was chosen for modeling purposes after reviewing literature and assessing that there was a rich selection of publicly accessible LET spectrums with measurements over days, weeks, and in some cases months. Every effort was made to utilize materials that are commercially available. This allows space radiation researchers at different research centers – for example, the European Space Agency – to replicate results at any heavy-ion accelerators capable of providing 1 GeV/n ^{56}Fe ions. For the Space Shuttle LET (SSL) simulation, polyethylene was chosen for the moderator block material since the hydrogen-rich compound can slow an iron nuclei in a reasonable length of mass while creating a modest amount of lighter progeny fragments and sufficient tensile strength for easy machining. An example of the polyethylene fragment spectrum versus that of aluminum is shown in Figure 3.4.

With the material selected for the SSL moderator block, multiple Monte Carlo simulations were run beginning with $20 - 30$ cm blocks centered around the approximate range of 1 GeV/n Iron in polyethylene. This choice was done under the assumption that most of the primary iron nuclei would fragment or stop along the block and minimize the iron contribution to the final spectrum. Additional blocks were simulated in increasing 5cm increments from 10 cm to 50 cm, and then in 10 cm increments up to 100 cm.

An example of the single layer simulation geometry is shown in Figure 3.5. The emerging field was scored on a plane one meter from the exiting point of the target block. For these simulations we chose the ambient environment measured in the beam house at the NSRL. This allows "air attenuation" of low-energy particles by allowing 1m of travel between the back plane of the moderator and the scoring plane. Additionally, this simulates the moderator placed in a beam-line with the hardware, tissue, or biological samples located 1m down the beam line. The charge, atomic

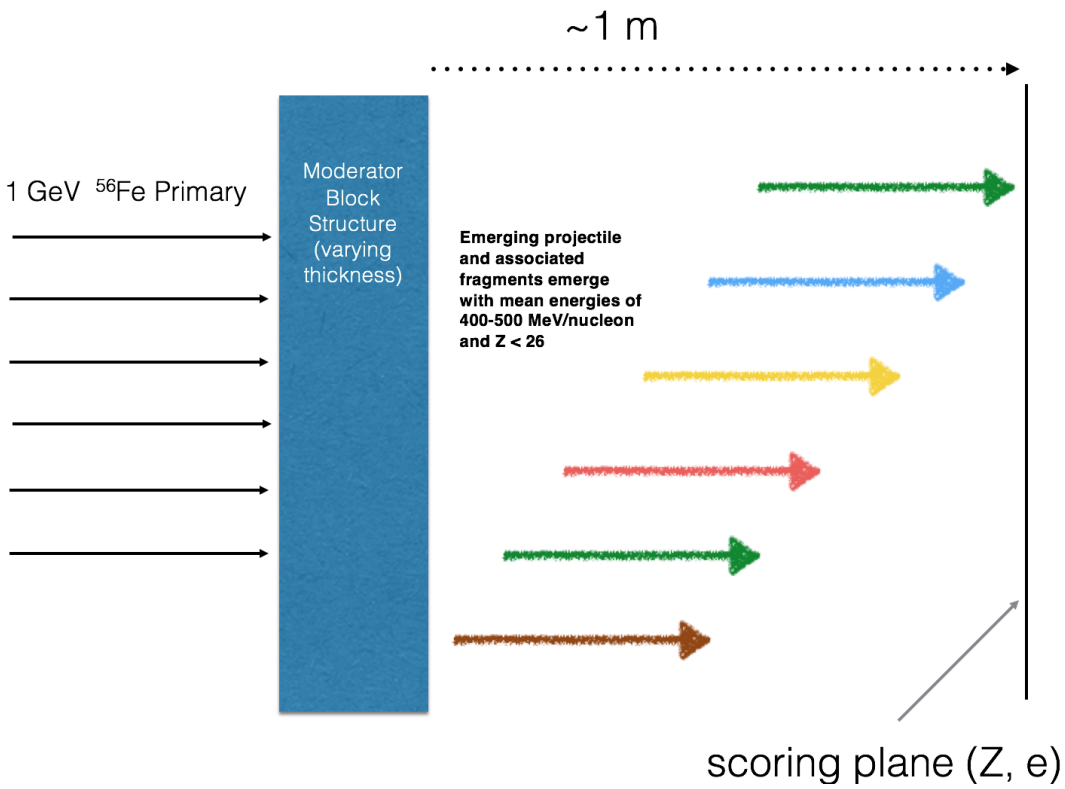

Figure 3.5: **Geometry of the Monte Carlo simulation**. Iron ions enter the target from the left and surviving primaries and progeny fragments exit from the right of the block. Charge species and energy are scored on a plane one meter from the exit point on the target block.

mass, energy, and relative location from the centerline of the initial beam path were scored at the 1m plane, as were the direction cosines for all particles that crossed in the direction of the primary beam.

Equation (2.7) was then used to determine each particle's LET (in water) and generate the simulated LET spectrum, per primary ion, as a function of target depth. These spectra were plotted and a function describing the shape of the curve was generated using a exponential fitting routine (*e.g.*, $g = Ae^{L}$). These provided the multiple subsets of the geometry factor, $g_n(n, I, C, \delta, \sigma)$, discussed in equation (3.2). The same fitting process was performed for the LET spectrum in Figure 1.2, providing the target LET distribution, $F(i, E)$.

An algorithm was created to test multiple iterations and combinations of the datasets, starting with the target block geometries closest to the stopping range of the primary beam. The amplitude, A,

was varied and compared to Figure 1.2, and the closest approximation was chosen. These represented the LET spectrum of potential target block lengths, that when summed and appropriately scaled, would best reproduce the desired LET spectrum. The final SSL moderator block function can be approximated with,

$$F_{\mathrm{SSL}}(i,E) = 7 \times 10^{9} \sum_{i=1}^{3} g_i(n, I = CH_2)\ f(Z = 26, E = 1000MeV/n), \tag{3.5}$$

where the subscript, i, sums over the contribution from the three determined layer thickness of 20 cm, 30 cm, and 40 cm that resulted in the closest approximate of $F_{\mathrm{SSL}}(i,E)$. The relative proportions for each layer, 20cm, 30cm, and 40cm were 1:10:400, respectively.

A three-dimensional version of the moderator block is recreated using combinatorial geometry for the PHITS Monte Carlo simulation. The internal geometry of the final moderator block used for the Space Shuttle orbiter model is shown in Figure 3.6. This model included accurate determinations of the width, length, and curvature of the various channels and cuts. The chemical composition and density specific to each of the moderator's layers also has to be specified for determining the material properties (for example, atomic structure, ionization potential, electron shell configuration, etc.) needed to perform the spallation and energy loss calculations. The block geometry presumes that the primary beam spot will encompass the leading face surface area.

As shown in Fig. 3.1, a 1 GeV/n ^{56}Fe primary beam is accelerated from the left, propagated through the moderator block and emerges along with progeny fragments generated during spallation reactions with the block materials. The field continues to the right where a scoring plane is located 1 m from the moderator block face. Particle species, energy, and directional cosines are recorded for analysis and LET calculations. The LET values (in tissue) are then calculated using the stopping power formula described in equation (2.7). All particles are scored, including electrons, pions, neutrons, etc. However, only the charged particles were considered for the final LET spectrum.

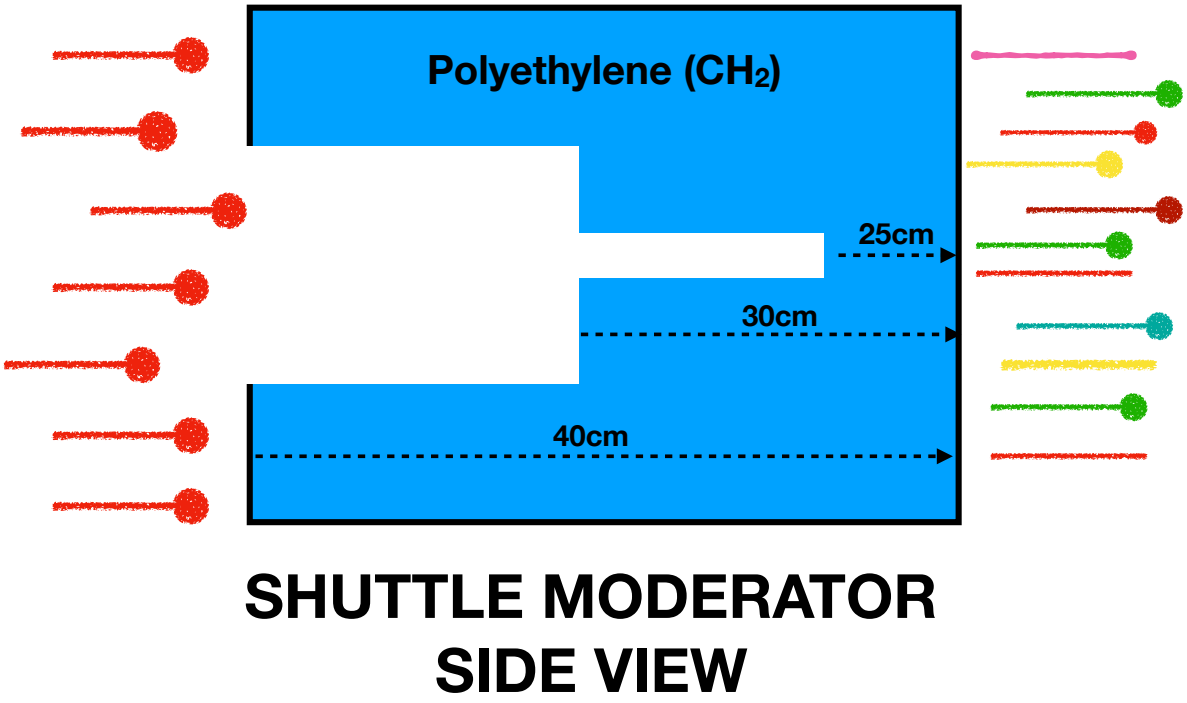

Figure 3.6: **Geometry of the Space Shuttle LET simulation**. Iron ions enter the target from the left and surviving primaries and progeny fragments exit from the right of the block. The three layers of Polyethylene used were 25cm, 30cm, and 40cm.

4. RESULTS

This chapter will illustrate how the moderator blocks developed in this study can accurately reproduce the intravehicular LET for different space exploration missions. Details on the approach are outlined in subsequent sections. Note that the moderator block data are *simulated* using Monte Carlo methods. Experimental validation of these simulations was performed using homogeneous blocks, which will be further presented in Chapter 6.

4.1 Space Shuttle Orbiter

The intravehicular LET spectrum during the Mir 18 and Mir 19 missions was chosen for initial validation of the model [129]. The Mir Space Station had an orbital inclination and flight altitude of 51.6° and approximately 200 nautical miles (370km). Beginning in March of 1995, NASA astronauts flew several long-duration missions on the Mir Space Station, returning to earth via the Space Shuttle. Badhwar et al., [129] measured the integrated LET spectrum that was directly attributed to GCR ions and their spallation progeny using tissue equivalent proportional counters (TEPC) and plastic nuclear track detectors located at six different areas of the vehicle. Contributions from neutrons and non GCR particles (e.g., Van Allen Belt ions) were not considered in order to more closely replicate their measured results.

Figure 4.1 shows the LET (per day) measured during the Shuttle-Mir 18 and Shuttle-Mir 19 Missions [129]. The blue solid line in the same figure represents the results of particle-transport simulations using the moderator block design developed in this work. A mono-energetic 1GeV/n iron (^{56}Fe) beam passes the moderator block carefully designed to output the LET measured in orbit. The distribution of LET obtained from the beamline simulation fits extremely well with the prediction for particles having a LET between 20keV/μm and 200keV/μm and with a reasonable fit for LET up to 500keV/μm. The output is appropriately scaled to closely match the average daily LET rate measured. Note that the simulated target moderator block reproduces the spectrum over approximately six orders of magnitude. In comparison, Fig. 4.1 also shows individual mono-

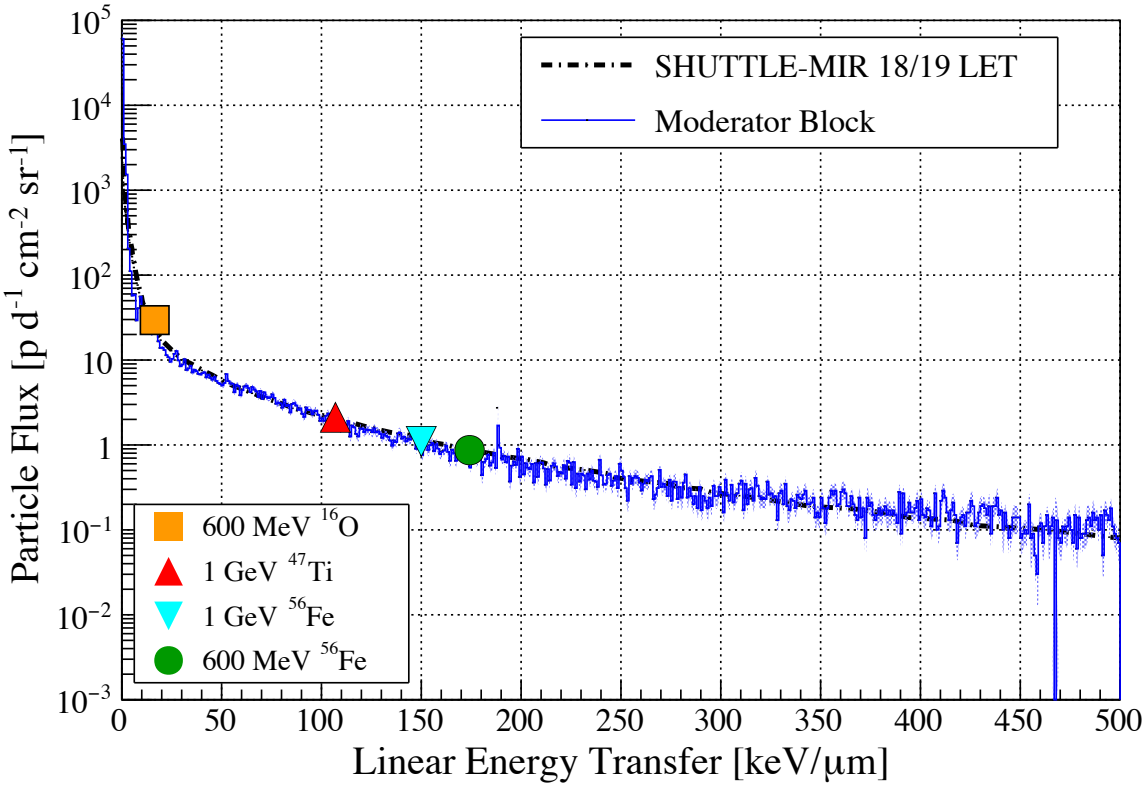

Figure 4.1: **Intravehicular particle flux (particles/day/cm^2/steradian) versus the LET (keV/micron) field from the Shuttle-Mir 18 and Shuttle-Mir 19 missions.** As measured by Badhwar *et. al.,* [129] (dashed line), as well as the results of our moderator block model simulation (blue solid line). The shading represents the statistical uncertainty in the model results. A close approximation of the measured LET spectrum is thus feasible for ground-based experiments. In addition, four single-ion exposures from current radiobiological experiments are shown (large symbols; see caption) to highlight the lack in breadth of energies in current radiobiological damage studies.

energetic ion beams currently used for radiobiological experiments. while accurate to their limited spectral contributions, these single ion exposures do not capture the richness of the measured intravehicular LET.

4.2 International Space Station

The ISS was launched into orbit in 1998 and is still flying today with an orbital inclination of $51.6°$ and an altitude of approximately 400km. Figure 4.2 shows the measured intravehicular

LET spectrum from the ISS. LET measurements were taken using a Timepix hybrid pixel detector [130, 131, 132]. The measured LET spectrum includes all charged particles (electrons, pions, heavy charged particles, etc.); however, like in the Badhwar et al.'s measurements for Mir [129], ISS measurements exclude neutrons. The simulation of the designed moderator block presented in Figure 4.2 again closely replicates the intravehicular spectrum of charged particles over many orders of magnitude.

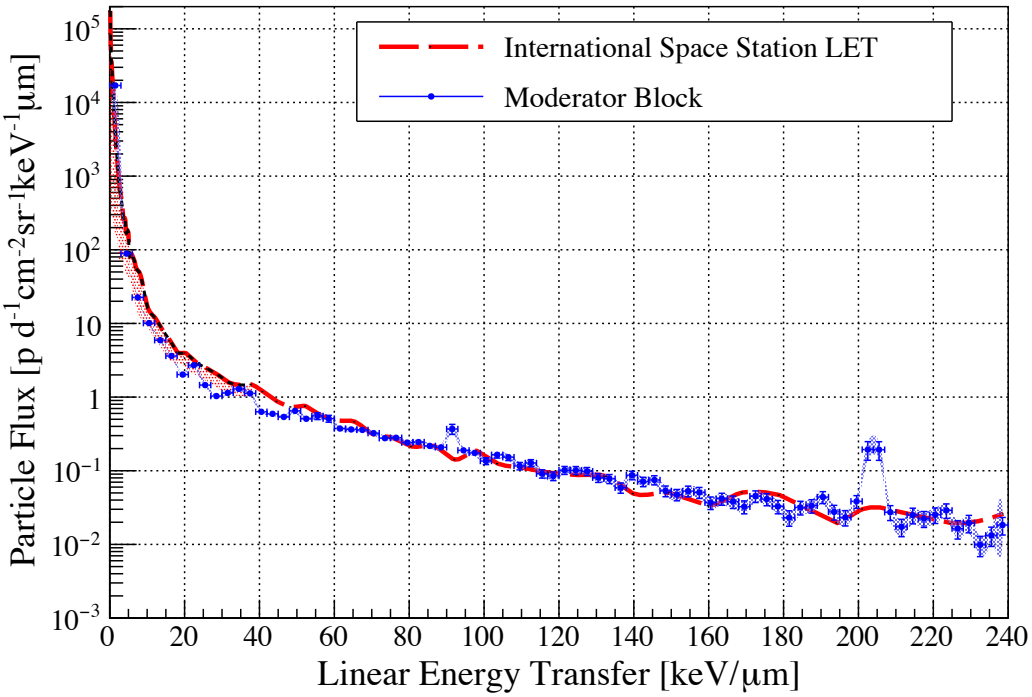

Figure 4.2: **Measured intravehicular LET field (per day) as measured onboard the ISS with a Timepix dosimeter (dashed line) compared to the moderator block model (blue solid line)**. The uncertainty in the numerical results is emphasized by the light blue shade. The spikes at LET approximately 90 keV/μm and approximately 205 keV/μm are due to an overabundance of energetic protons generated in the thicker layers of the modeled block. The red shaded area indicates an uncertainty in the low-energy measurements (LET $\leq$ 40keV/μm). This is most likely due to secondary electrons stopping within the instrument's silicon detector and resulting in an overestimation of approximately 10% of their LET values. Note that the original LET measurements were normalized per second; measurements have been re-normalized to LET per day for consistency, as well as to display the estimated LET rate in units that are more relevant to radiation risk estimation for long-duration missions.

The contribution of particles with low LET ($\leq$ 40 keV/μm) falls off much more slowly than what was seen for the Mir 18/19 measurements. This results in a moderator block with a far more complex geometry, including layers with thicknesses much greater than previously anticipated (e.g., larger than 50cm) that could generate the low-Z, high-energy particles needed to shape this portion of the LET distribution. The resulting spectrum closely matches the measured energies to a high degree of accuracy for continuous LET values of up to 240 keV/μm over approximately seven orders of magnitude. The sharp peaks in the modeled LET spectra seen at 90 keV/μm and 205 keV/μm result from an overabundance of low-energy protons ($E \leq 2$ MeV) generated in the thicker portion of the moderator block. These results indicate that modifications to the internal block geometry and material composition can successfully fit dose spectra for space vehicles with vastly different structure and shielding capabilities (i.e., the Space Shuttle versus the much larger and more heavily-shielded ISS).

4.3 Multi-Purpose Crew Vehicle Exploration Flight Test

The measurement results from NASA's recent Exploration Flight Test (EFT-1) were recently made available and provided us with an opportunity to illustrate the robustness of our approach by demonstrating the ability to fit the intravehicular LET spectrum as measured onboard a third space vehicle [133]. EFT-1 was the first flight of the new Orion Multi-Purpose Crew Vehicle (MPCV) that NASA will use for future interplanetary exploration missions. Although the MPCV had a brief flight duration of approximately four hours, the EFT-1 data are unique because of a high apogee on the second orbit that included traversal through the radiation-dense Van Allen Belts and briefly into the interplanetary radiation environment. Timepix-based radiation detectors were operational shortly after liftoff and collected data for the duration of the mission [134].

Similar to the Mir and ISS measurements, the EFT-1 flight data did not include measurements from non-charged particles (i.e., neutrons) which can provide a significant contribution to the total dose. This model is capable of generating both thermal and fast spallation neutron products; however, for better comparison with the measured data, these calculations were not included in the modeled LET spectrum. The EFT-1 flight data are shown in Fig. 4.3 along with the results of

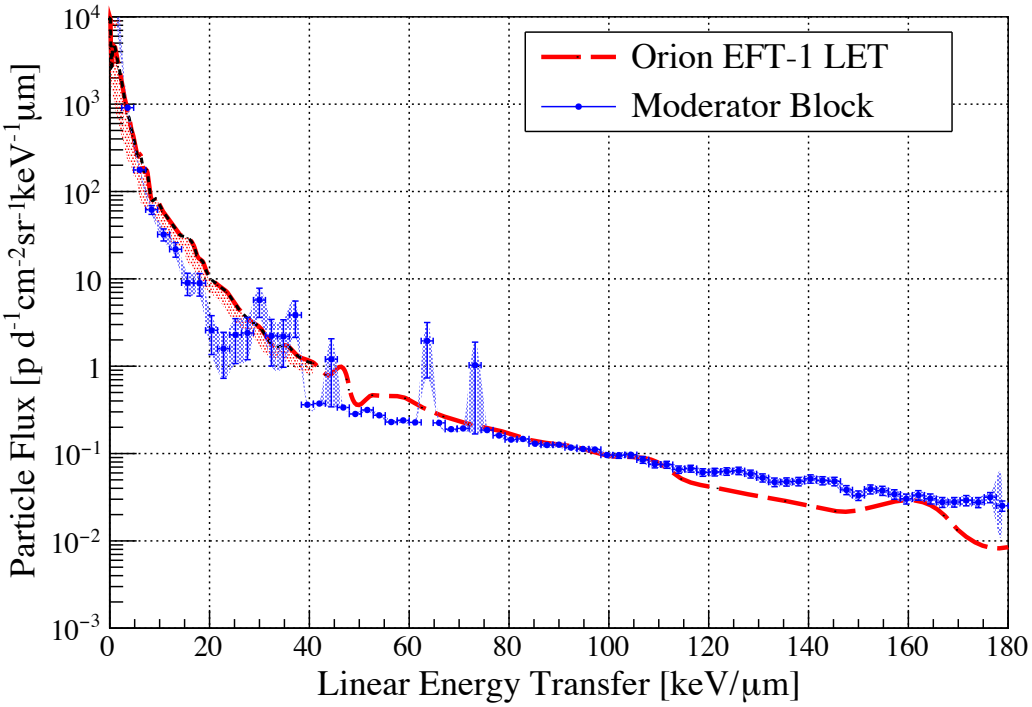

Figure 4.3: **LET field measured during the EFT-1 flight of NASA's new Orion Multi-Purpose Crew Vehicle**. The EFT-1 mission lasted approximately four hours and included two orbits with a peak altitude of approximately 5800km. The LET was measured for the duration of the entire flight and averaged to LET per day [133]. The exposure includes both interplanetary and Van Allen belt radiation fields. The mission is similar to the Apollo 4 mission of 1967, that validated the Apollo flight control system and heat shield at re-entry conditions planned for the return from lunar missions.

the model modified to accommodate for the unique spectrum. Results fit reasonably well with the flight measurements, though there are visible fluctuations in the 30-80 keV/μm range with several sharp peaks at approximately 65 keV/μm and 73 keV/μm. This weakly corresponds to a smaller fluctuation found from 30-50 keV/μm in the measured data. It is not yet clear whether these are indicators of the true nature of the measured LET spectrum or simple statistical fluctuations resulting from the smaller measurement period of the EFT-1 flight. Moderator layers made of polymers as thick as 100 cm are required to produce this LET spectrum. The sharp peaks at approximately 65 keV/μm and 73 keV/μm in the model results are due to an overabundance of ions with charge $Z \leq 6$ in these 90 cm and thicker layers. Of note, effort was made to use *few* hydrogen-rich materials in

the model. The relative difficulty in reproducing the EFT-1 data may be an indication that other low-Z materials and metamaterials should be considered in future studies.

4.4 Statistical Error Analysis

Systematic errors associated with these results are attributed to the many approximations required for a three-dimensional particle-transport Monte Carlo simulation. The bootstrap method was utilized for error analysis to verify the statistical stability of the results and minimize systematic biases in the outcomes [135].

The bootstrap analysis used N_{boot} data sets each containing N points that were obtained by random sampling of the original N points in the dataset with the constraint:

$$\sum_{i=1}^{N} n_i = N, \tag{4.1}$$

where n_i is the number of times a data point x_i appears in the generated datasets and N_{boot} is the number samples sets. The *bootstrap* average of x_i is then found with:

$$x_\alpha^\beta = \frac{1}{N} \sum_{i=1}^{N} n_i n_i^\alpha x_i, \tag{4.2}$$

where α is summed from 1 to N_{boot}. The bootstrap average of the mean of x along with the bootstrap variance of the mean was then determined with:

$$\overline{x}^B = \frac{1}{N_{\text{boot}}} \sum_{\alpha=1}^{N_{\text{boot}}} x_\alpha^{\text{B}} = \sum_{i=1}^{N} [n_i]_{\text{MC}} x_i = \sum_{i=1}^{N} x_i = \overline{x} \tag{4.3}$$

$$\sigma_{x^{\text{B}}}^2 = \frac{1}{N_{\text{boot}}} \sum_{\alpha=1}^{N_{\text{boot}}} \left[(x_\alpha^{\text{B}})^2 \right]_{\text{MC}} - (\overline{x}^B)^2 = \frac{1}{N^2} \left(1 - \frac{1}{N} \right) \sum_{i=1}^{N} x_i^2 - \frac{1}{N^3} \sum_{i \neq j}^{N} x_i x_j. \tag{4.4}$$

These are summed over many repetitions of the original data set and the averages are found with:

$$\langle \overline{x}^{\mathrm{B}} \rangle = \langle \overline{x} \rangle \equiv X \tag{4.5}$$

$$\langle \sigma^2_{x_{\mathrm{B}}} \rangle = \frac{N}{N-1}\sigma^2 = \frac{N}{N-1}\sigma^2_{\overline{x}}. \tag{4.6}$$

These show that the bootstrap average, $\overline{x}^{\mathrm{B}}$ is an unbiased estimate of the exact average X. Using equation 4.6, an unbiased estimate of the uncertainty, can be determined with:

$$\sigma_{\overline{x}} = \sqrt{\frac{N}{N-1}}\sigma_{x^{\mathrm{B}}}, \tag{4.7}$$

where N is carefully chosen so that the square root term is approximately equal to unity. The minimum value of N_{boot} was determined by performing the above analysis with iterations of increasing N_{boot} until the value of $\sigma_{\overline{x}}$ converged, indicating the unbiased estimate of uncertainty for the entire data set.

4.5 Benchmarking PHITS LET Measurements

The development of PHITS was in the support of heavy-ion radiotherapy and the intermediate energies of interest in this study. There are several other notable 3D Monte Carlo particle transport codes *e.g.,* FLUKA (Fluktuierende Kaskade), GEANT4 (GEometry ANd Tracking), MCNPX (Monte Carlo N-Particle Transport) [136, 137, 138]. Both PHITS and FLUKA utilize the total reaction cross-sections developed by Tripathi et al. [126, 127, 128]. It should be noted that PHITS uses the Tripathi cross-section model as the default option, however, the model developed by Shen can be selected by the user. These will be referred to as Tripathi-PHITS and Shen-PHITS, respectively[1].

GEANT4 implements a variety of reaction cross-sections depending on atomic and mass number of the reaction system and collision energy. For protons and light particles, the Axen-Wellisch and Tripathi light-ion parameterizations are used, while Tripathi et al., is used for intermediate energy

[1]The Tripathi parameterization has been adopted by NASA and is the cross-section model used for all PHITS simulations in this thesis study.

heavy ions (e.g., up to approximately 1 GeV/n). At very high energies, above 1 GeV/n, GEANT4 employs the Shen reaction cross-sections [139, 126, 127, 128, 140].

A recent study by Sihver et.al., compared the total reaction cross-sections for a ^{56}Fe iron nuclei interacting with a CH_2 target as calculated by the transport codes GEANT4, FLUKA, and PHITS. For the PHITS measurements, both cross-section tables, e.g., Shen and Tripathi, are demonstrated. The results, seen in Figure 4.4, show that particle generation in PHITS is in agreement with similar 3D Monte Carlo codes [141], where there is reasonable agreement between each of the codes for energies greater than approximately 50 MeV/n. In each case, the transport codes slightly over predicted the previously measured total reaction cross-sections, with Tripathi-PHITS closer to the experimental measurements, however both FLUKA and GEANT4 still have reasonable approximations of the cross-section values.

Both GEANT4 and Shen-PHITS predict higher cross-sections for energies between 100 MeV/n and 1 GeV/n, while FLUKA and the Tripathi-PHITS cross-sections have similar outcomes over the same range. For energies greater than 1 GeV/n, which is outside the energy of interest in this study, all model outcomes have similar predictions with the Tripathi-PHITS measurements showing slightly lower total reaction cross-sections. A discontinuity at 1 GeV/n is seen in the GEANT4 measurements. The authors attribute this to a model transition, without smoothing, from the Tripathi parameterizations at lower energies to the Shen model at higher energies [141].

These results reported by Sihver et al., show that the total reaction cross-section and generation of progeny fragments by PHITS are in agreement with FLUKA for projectile ion species, energies, and target material used in this study, e.g. 100 - 1000 MeV/n. Relative agreement is also seen between PHITS and GEANT4. These results, however, do not clarify the energy distribution of reaction products emerging from the target blocks. Thus, we will compare the emerging LET field of 1 GeV iron primary and 30 cm CH_2 target generated with PHITS, to the same using FLUKA. The 30 cm target block is chosen because it is used in the SSL model found in Section 4.1. Additionally, the target dimensions are greater than the range of a 1 GeV iron nuclei in CH_2 (approximately 24 cm), ensuring that the ions emerging from the target block simulation are progeny fragments.

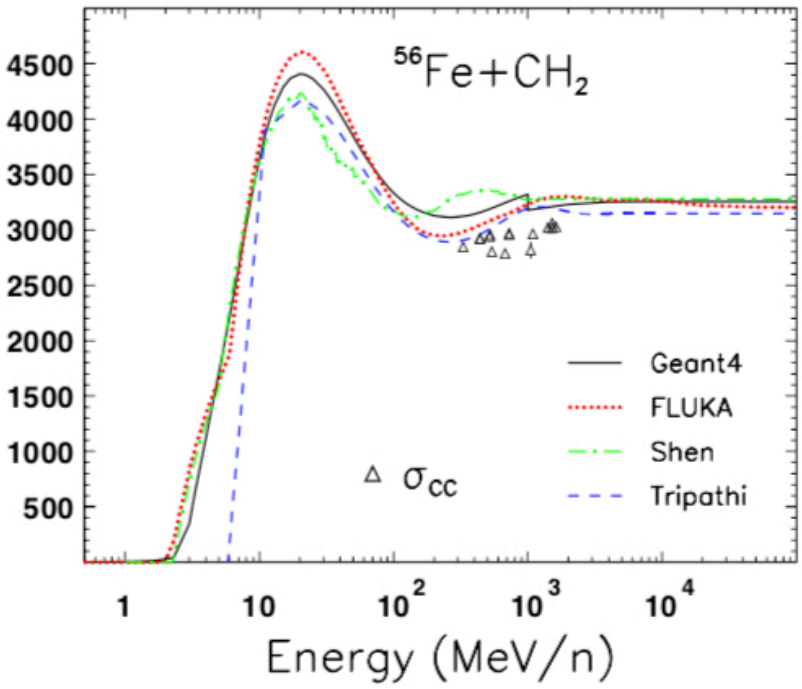

Figure 4.4: **Comparison of PHITS to similar particle transport codes.** Total reaction cross-sections for Iron primary and CH_2 target compared to PHITS, FLUKA, and GEANT4. Here *Tripathi* refers to PHITS simulations using the default Tripathi cross-section tables, while *Shen* refers to the same measurements with the Shen cross-section tables implemented. Figure reprinted with permission from Reference [141]

For this verification exercise, FLUKA was compiled on a Linux virtual machine using Linux Intel Fortran, the same used for compiling PHITS for all the simulations discussed in this thesis study. A 3D combinatorial geometry, replicating the 30 cm target block used in the SSL model (e.g., Section 4.1) was created, with careful attention to utilizing the same target geometry, chemical makeup of the target block, and the ambient environment measured in the beam house at the NSRL. The emerging field was scored one meter from the exiting point of the target block. A sample set of n=10000 primary ions was used and the results were normalized to per primary iron ion.

The results, shown in Figure 4.5, show qualitative agreement for LET energies up to approximately 60 keV/μm, and to within a half order of magnitude for higher LET energies. This indicates, along with the results reported by Sihver et al., some confidence that the outcomes generated in

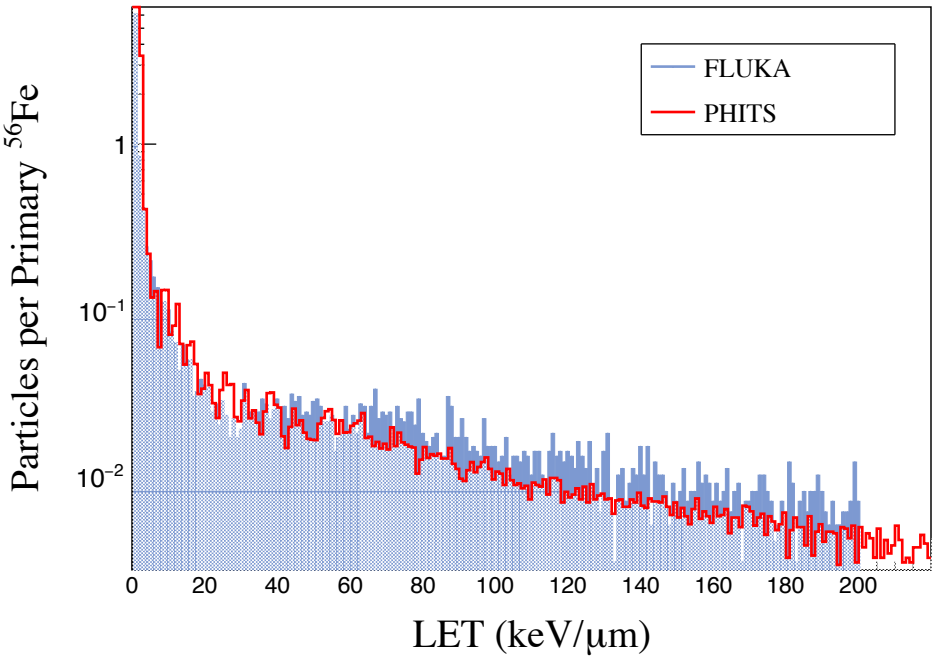

Figure 4.5: **Comparison of LET fields generated by PHITS and FLUKA.** The emerging LET field from a 1 GeV iron primary on a 30cm CH_2 target. The results, normalized to per primary nuclei, show that PHITS (blue) has reasonable agreement with the output from FLUKA (red).

Sections 4.1 – 4.3 are not dependent on the choice of 3D Monte Carlo particle transport code. It is feasible to conclude that 3D Monte Carlo analysis with similar constraints using PHITS or FLUKA, will provide similar LET distributions for the primary ion species, target material, and geometries being studied.

These results provide initial verification that the numerical methods discussed in this chapter replicates the desired LET fields. Model utility, however, depends on how accurately a given model can reproduce physical observations and measurements as well as make accurate predictions. Clearly, further work remains and validation using experimental beamline measurements will necessitate confidently concluding that the proposed method is an accurate replication of physical results.

5. DIRECT VALIDATION WITH EXPERIMENTAL DATA FROM PEER REVIEWED LITERATURE

All models, to a certain degree, are limited in the ability to capture all features measured in experiments. Model utility depends on how accurately a given model can reproduce physical observations and measurements as well as make accurate predictions. The primary hypothesis of this work was to develop a model that recreated the intravehicular LET spectrum as measured in spaceflight vehicles. The stopping power, and thus the energy loss of charged particles transported through single-ion materials and most other compounds, has been exhaustively validated with experimental results [142, 143, 144, 145, 146].

As an example, the Shuttle-Mir missions depicted in Fig. 4.1 are analyzed in more detail. The relative accuracy of the charge distribution resulting from the moderator block is shown in Fig. 5.1. These results provide initial evidence that the model could, with clever utilization of materials and geometry, more closely match both the LET *and* the the charge distribution of the measured field. This would provide a true, ground-based analog of the space radiation environment. The preliminary validation study will thus focus on the prediction accuracy of progeny fragments created by the highly stochastic spallation processes. Here the moderator block model will be compared to experimental measurements of the fragmentation production of 1 GeV/n ^{56}Fe ions incident on several different targets. The target materials include pseudo-thin and thick hydrogen-rich compound materials (CH_2), lead (^{208}Pb), and aluminum (^{26}Al), which are commonly found in the structure of space vehicles. The fragmentation and particle multiplicity are reproduced using the moderator block model and compared with the published results of Zeitlin et al. [148, 149, 124, 125].

Figures 5.2(a) – 5.2(d) demonstrate that the model provides a close reproduction of the charge distribution measurements for each of the target blocks. The fluence of surviving ^{56}Fe primaries closely agrees with the measured fraction of surviving projectiles measured, providing an initial demonstration of the model's accuracy in replicating the mechanisms of charge-changing interactions. In each case, the odd-even effect is clearly visible, with a slight preferential enhancement of

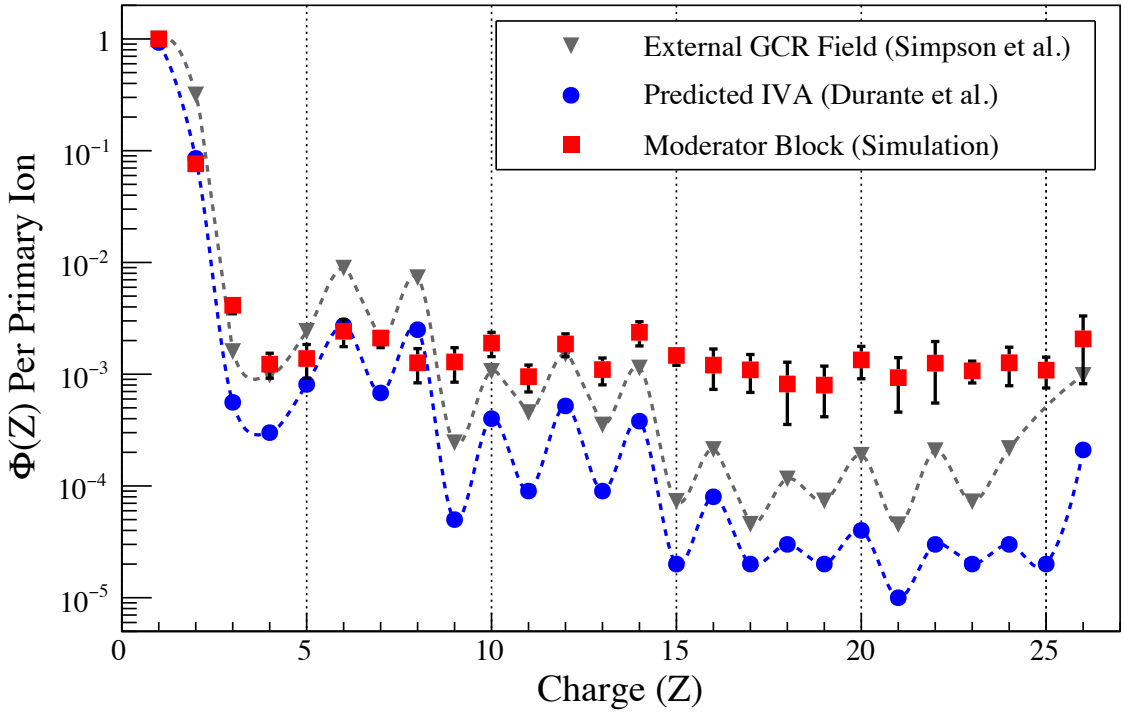

Figure 5.1: **Comparison of predicted charge distributions.** The relative abundance of intravehicular ions in the exiting field created by the moderator block (red squares), as well as the results of Durante et al., [147] (blue circles), as a function of the atomic number Z. The lower-Z ions ($Z \leq 8$) that contribute to the majority of the entire spectrum closely match the predicted abundance. There is a close similarity in the distribution of ions for $Z \leq 14$. As Z increases up to ^{56}Fe ($Z = 26$), the charge distributions diverge similarly, with the moderator block generating more heavy ions.

even-charge fragments. Knott et al., first demonstrated this effect for projectiles with isospin $T_z = 0$ [150], but Zeitlin et al., showed that there was still a subtle, but pronounced, odd-even trend with 1GeV/n ^{56}Fe projectiles ($T_z = -2$) [151].

Previous studies have shown that the closed $d_{5/2}$ Si sub-shell should lead to an enhancement of $Z = 14$ (Si) fragments. This is seen in Figs. 5.2(a), 5.2(b), and 5.2(c), but is less subtle in Fig. 5.2(d). This trend is repeated in the the measured suppression of $Z = 9$ (F). This is seen in the ^{26}Al, ^{208}Pb and thinner CH_2 target(s), but is less obvious in the thick CH_2 target block.

The measured fluence of progeny fragments is accurately replicated with the model to within approximately half an order of magnitude or less for each test case. There is still room for

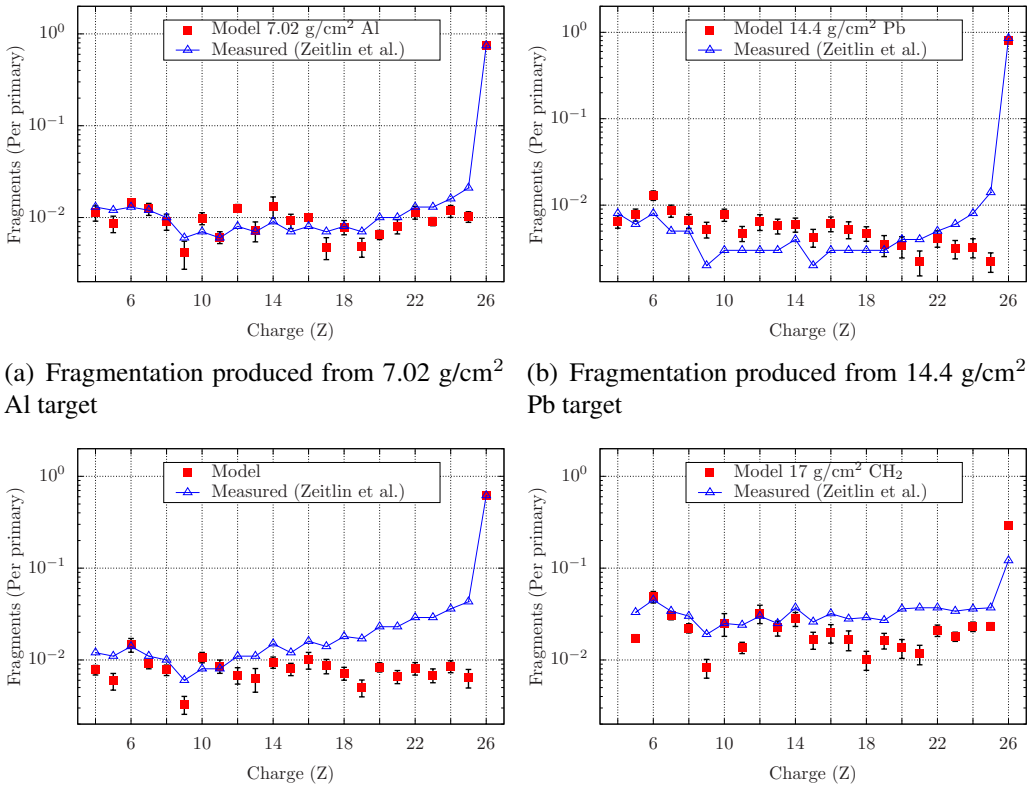

(a) Fragmentation produced from 7.02 g/cm^2 Al target

(b) Fragmentation produced from 14.4 g/cm^2 Pb target

(c) Fragmentation produced from 4.2 g/cm^2 CH_2 target

(d) Fragmentation produced from 17 g/cm^2 CH_2 target

Figure 5.2: **Comparison of charge multiplicity in mono-ion and compound targets.** The relative abundance of fragment ions per primary in the exiting field created by the moderator block (red squares), as well as the measurement results of Zeitlin et al. [125] (blue triangles), as a function of the atomic number Z. For each case, there is a good agreement in the surviving ^{56}Fe primaries with the measured fraction of surviving projectiles measured by Zeitlin et al., This provides good initial indication that the model is very capable of accurately replicating the mechanisms of charge-changing interactions. Additionally, there is a visible preference for even charged progeny, as demonstrated by Zeitlin et al., and previous experiments [150, 151]. Figure adapted from Zeitlin et. al. 2008 [151], with permission from Elsevier.

improvement. However, this work was intended merely as a demonstration of a proof-of-principle design. Compared to previous mono-energetic single-ion beam studies, this model represents a far more accurate emulation of the effects of space radiation. The trend for both single material blocks, ^{26}Al and ^{208}Pb, demonstrates good agreement for all charges $4 \leq Z \leq 26$. In the 4.2 g/cm^2 CH_2 target, there is good agreement for $4 \leq Z \leq 16$ with subsequent divergence for charges greater

than $Z = 17$. A similar trend is seen in the thick CH_2 target, Fig. 5.2(d), but with model results diverging at $Z \approx 15$. Additionally, the survivability of the primary ^{56}Fe is under-predicted in the thicker CH_2 target block, but within an acceptable half-order of magnitude.

In the mono-species target blocks (panels (a) and (b) of 7.4, there is very good agreement with the measured charge distribution including the expected enhancement of $Z = 14$ (Si) and suppression of $Z = 9$ (F). In the (thin) CH_2 target (panel (c)), the progeny ions created in fragmentation reactions closely match the predicted abundance up to approximately $Z \leq 16$. There is a very close match with the amount of surviving primary ions, ^{56}Fe. There is a close similarity in the distribution of ions for $Z \leq 17$. As Z increases up to ^{56}Fe ($Z = 26$), the charge distributions diverge similarly, but with the the moderator block generating less heavy ions to within one order of magnitude. Similar to the thin CH_2 target, the progeny ions created in fragmentation reactions (panel (d)) closely match the predicted abundance up to approximately $Z \leq 14$, with the amount of surviving ^{56}Fe primary ions slightly higher than measured. There still remains a close similarity in the distribution of ions for $Z \geq 15$ up to ^{56}Fe ($Z = 26$), where the charge distributions diverge (to within one order of magnitude) with the the moderator block generating less of the heavier ions.

Summarizing, the model demonstrates that the intrinsic properties of hydrogen-rich crystalline materials can preferentially produce specific nuclear spallation and fragmentation processes when placed in an accelerated heavy-ion beam. The perturbation of their micro-structure can influence the material's capability to simultaneously generate the complex mix of LET, nuclei, and energies found in the GCR spectrum. Astrophysics models should demonstrate an agreement better than 10% with measured and observed data [150]. The under-emphasis of $17 \leq Z \leq 25$ charges in Fig. 5.2(c) and $Z \geq 6$ charges in Fig. 5.2(d) is likely attributed to a weakness of the cross-section dynamics for charged particle transport, where the normalization factors used in the interaction model(s) are less effective as fragment Z increases towards the charge of the projectile ion. These higher-Z fragments are produced in peripheral collisions that are very sensitive to the choice of allowed impact factors defined in the molecular dynamics, leading to interaction cross-sections that are hyper-responsive to the primary ion's energy and charge, target material(s), etc. Previous

research studies have demonstrated a preference for low-Z targets to generate low-Z fragments (e.g., $Z \lesssim 8$). In the work presented here, we observe an accurate replication of surviving primaries in both of the CH_2 target(s) but a noticeable divergence of progeny fragments created as Z increases. These results indicate further tuning of the model is needed, perhaps with the exploration of other target materials and metamaterials.

6. BEAM-LINE MEASUREMENTS

An experiment performed at the NSRL. The NSRL uses beams of heavy ions extracted from Brookhaven's Booster accelerator to provide heavy charged particle beams of species and energies similar to those found in LEO and intergalactic space. NSRL has its own beam line dedicated to radiobiology and materials research with state-of-the-art specimen preparation resources available to the researcher. NSRL allows for space radiation scientists to expose condensed matter and biological specimens (e.g., tissues, cells, and cell DNA), to beams of relativistic heavy ions.

Beam-line measurements were performed through beam time sharing to minimize associated cost, though this led to data collection being reliant on the completion of preceding experiments and rapid data collection. Experimental target blocks were borrowed from the Nuclear Research Center and transported to the NSRL. The target blocks included approximately 150 lbs. of polyethylene (CH_2) blocks to match the SSL model parameters discussed in Chapter 4. Pre-calibrated scintillator detectors were supplied by the beam-line science staff. These moderator block measurements were performed to provide further experimental validation of the model outputs discussed in Chapter 4 and allow for robust comparison between a Monte Carlo-generated and a physically constructed moderator block. Results of the physical experiment, and comparison to model outputs, will be discussed below and in the following chapter.

6.1 Experiment Design

Beam-line measurements were taken using a 1 GeV ^{56}Fe beam incident on four polyethylene targets with thicknesses of 10 cm, 20 cm, 30 cm, and 40 cm. The beam was measured upstream of the target using a thin trigger counter ($3 \times 3 \times 0.2$ cm^3). The trigger counter was used for coincidence of the downstream energy deposition and to initiate the event-by-event data acquisition. The counter signals an acquisition or 'start' when a particle is measured and opens the 'gate' to collect all fragments. The next subsequent primary triggers a new 'start' signal. The trigger counter was positioned approximately 18.28 cm upstream of the target blocks.

Downstream of the target blocks two thin plastic scintillator dE/dx counters were used to record successive energy deposition measurements of the primary and fragment particles emerging from the target blocks. The dE/dx scintillators (dE1, dE2) had thickness of 0.625 cm with active areas of 160 cm^2. The distance between dE1 and dE2 was measured to be 28 mm, allowing the approximation that both detectors subtended the same solid angle as seen from the center of the target. Immediately following the dE/dx detector array was a large calorimeter (CAL) with a thickness of 20.96 cm. The initiation of each event recorded by the dE1, dE1, and CAL detectors was provided by the trigger counter. Energy deposition events were recorded by a charge-sensitive analog to digital converter for each detector. For each event the value of the trigger pulse were recorded. Each beam spill provided a 1 cm RMS ^{56}Fe beam with a flux of approximately 10^6 ions/spill.

The four target blocks used were ultra-high molecular weight polyethylene with measured thickness of 10.16 cm, 10.3 cm, 9.7 cm, and 12.2 cm. The variation in target thickness, intended to simulate the moderator block construction used in the Monte Carlo results, was created by placing successive blocks to give target thicknesses of 10.16 cm, 20.46 cm, 30.16 cm, and 42.36 cm. For ease of discussion, we will refer to these as the 10cm, 20cm, 30cm, and 40cm target blocks. The material density of the target blocks is 0.93 g/cm^3, the ionizing potential (I) 57.8 eV, and the electron density 3.435×10^{29} g^{-3}.

The detector acceptance is defined by the location of dE1 as seen from a point at the exit of the target and precisely on the beam axis. This corresponded to a cone of half-angle $3.0^\circ - 3.5^\circ$ for the 10cm and 20cm blocks, and approximately 3.9°-4.6° for the 30cm and 40cm target blocks. Figure 6.1 shows the layout of the experiment for each of the five data sets. Post-measurement calculations determined that the energy of the primary ions emerging from the trigger counter was approximately 994.5 MeV/n. The distances from the exiting side of the 10cm, 20cm, 30cm, and 40cm target blocks to dE1 were 94 cm, 83.7 cm, 74 cm, and 61.8 cm, respectively. An additional dataset with no target blocks, referred to as the *target-out* data set, was recorded to provide calibration of the detector array. This provided five distinct datasets for LET discrimination, ion identification, and cross-section measurements.

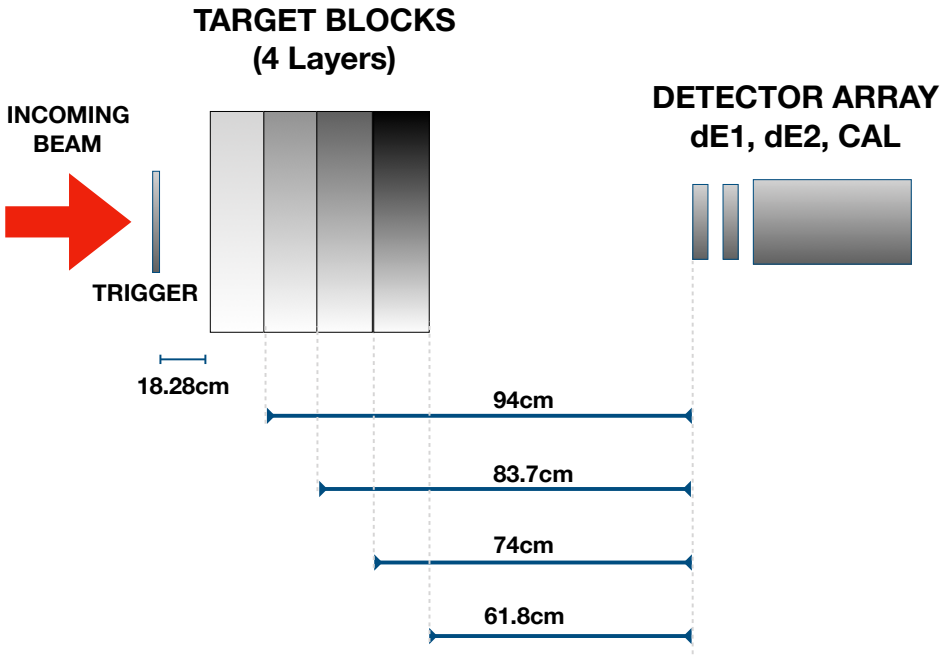

Figure 6.1: **Schematic of the experiment performed at NSRL on November 19, 2016.** Primary beam of 1 GeV ^{56}Fe ions is accelerated from the left passing through the trigger detector which initiates event recording by the successive dE/dx and calorimeter detectors. Beam ions and progeny fragments emerge from the target block, accelerated towards the detector array. Successive discrete energy depositions in the thin dE/dx detectors followed by large energy deposition of a "ranged out" particle allow for LET discrimination in order to identification of ion species.

6.2 Data Analysis

Several steps were performed to eliminate the events that are not attributed to the primary ions interacting with the target blocks. As the accelerated primary ions exit from the evacuated part of the beam-line, interactions with the beam-line infrastructure can provoke inhomogeneity by introducing contaminant ion species or energy loss. Progeny fragments are also produced by the interaction of the beam with the trigger detector upstream of the target blocks. In order to eliminate these discrepancies, only the events within about two standard deviations of the iron peak as measured in the trigger detector are kept for analysis (Figure 6.2).

It is useful at this point to normalize the event measurements to the energy deposition in dE1,

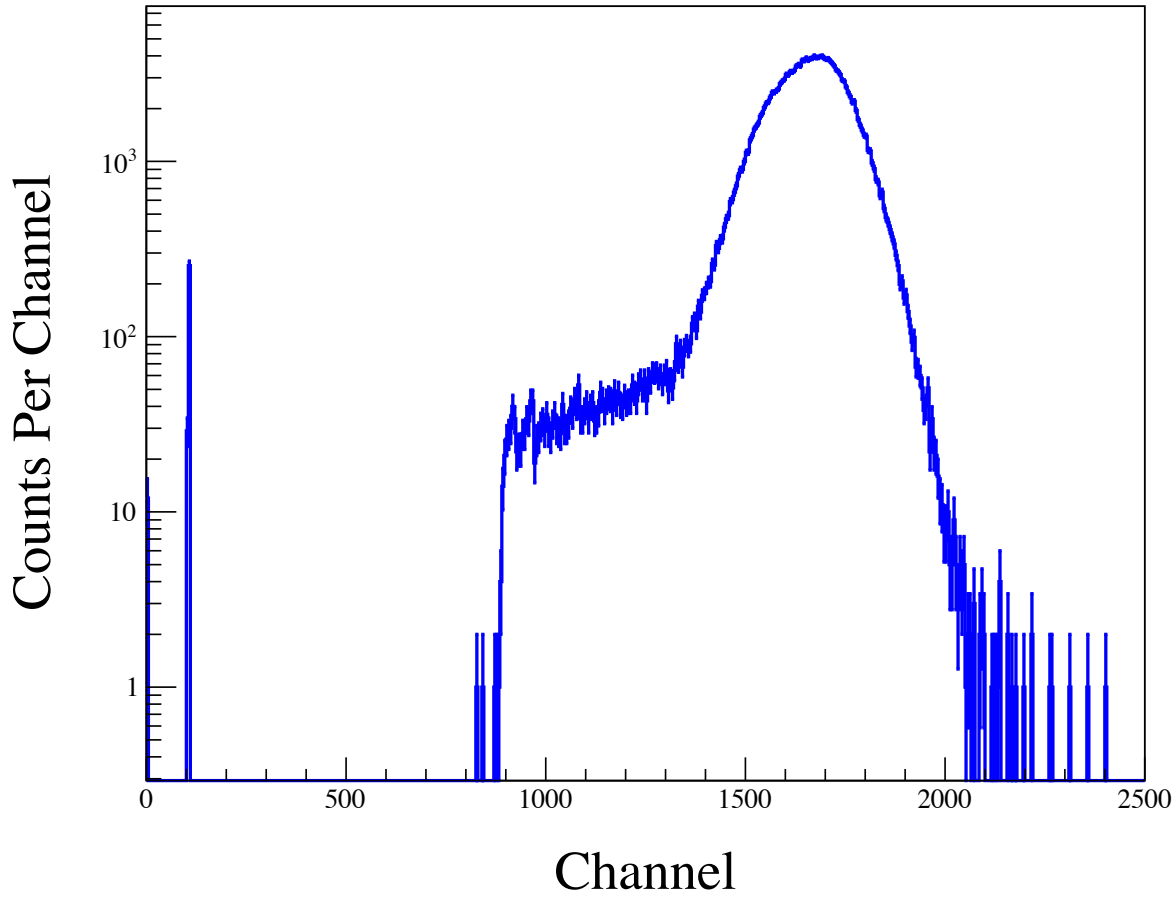

Figure 6.2: The peak of the primary ^{56}Fe beam is found and only events corresponding to those within two standard deviations are kept for analysis. Typically the number of events was reduced by 5-7% that could be attributed to contamination in the beam prior to leaving the beam-line vacuum or fragments created in the trigger detector.

dE2, and the calorimeter detectors. Using equation (2.7), target-out measurements for energy deposition in each detector were normalized to the iron peaks at 882.086 MeV, 885.244 MeV, and 29,321 MeV, for the dE1, dE2, and CAL detectors, respectively. These values were subsequently used in the analysis for all datasets.

A second cut was performed using profile histograms of the energy depositions made in detectors dE1 and dE2. This determines which events recorded an incomplete registration in one of the detectors (*e.g.* edge hits, incomplete charge registration by the detector electronics, etc.) or

fragments created in either of the dE detectors. An example is shown in Figure 6.3 for the 10 cm target block. In this figure the blue colored dots are measurements retained for analysis, while the red colored dots are discarded events. The events lying along the densely populated 45° line (up to the predominant iron peak) represent lighter progeny fragments created in spallation processes inside the target block and indicate well-correlated signals.

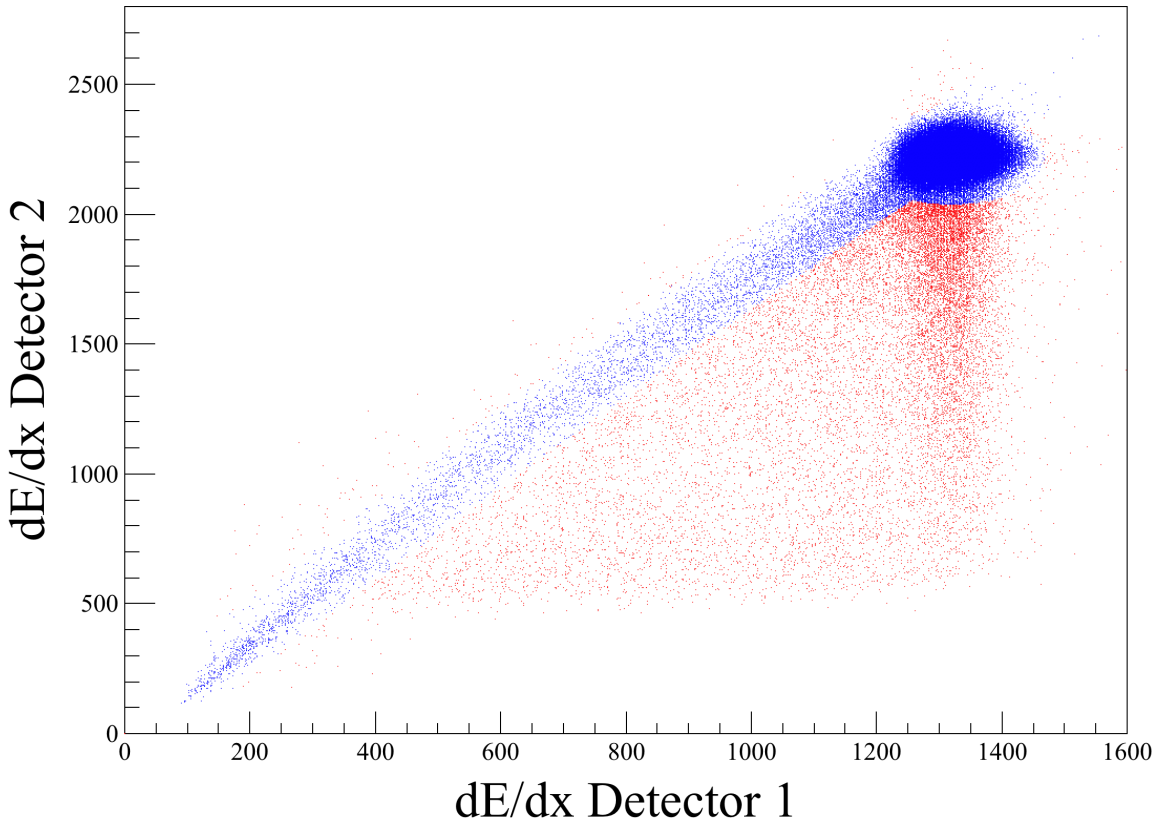

Figure 6.3: The second "cut" of the data sets. The blue colored dots represent measurements in dE1 and dE2 that are well correlated. The red colored dots are likely fragment products produced in either dE/dx detector or events that were not completely recorded. The prominent blue spot are the primary ^{56}Fe ions. The well emphasized line of red dots emerging from below the primary ions plotted are ^{56}Fe ions that fragmented in the first dE/dx detector.

For thick targets, as is the case in this study, it could not be assumed that the progeny fragments produced in the target blocks would emerge with approximately the same velocity as the primary

ions. This is because at high energies the logarithmic term in the stopping power equation (Equation (2.9)) is slowly varying with energy allowing for the energy deposition to be approximated with $(dE/dx) \propto z^2/\beta^2$, and, subsequently, the charge distribution could then be determined with,

$$Z_i = Z_{Fe} \sqrt{\frac{\Delta E_i}{\Delta E_{Fe}}} \tag{6.1}$$

Since this was not the case, an additional correction is needed to accurately analyze the charge spectrum of the emerging ion field. The energy spectrums measured in dE1 and dE2 can be scaled to a LET distribution with the approximation, $LET = \alpha \Delta E$. Here α is a constant that relates the energy deposition to the LET to within $\pm 5\%$ and conveniently allows the conversion to LET in water (H_2O) for direct analysis by the scaling relation [152, 153],

$$LET_t(Fe) = \frac{\Delta E_t(Fe)}{\Delta E_0(Fe)} LET_0(Fe). \tag{6.2}$$

The subscripts t and 0 refer to the measurements taken with and without the target block in the beam, respcetively. The values for $\Delta E_0(Fe)$ and $\Delta E_t(Fe)$ were obtained from the measurements, while $LET_0(Fe)$ was determined using equation 2.7. For the determination of $LET_0(Fe)$, the energy loss of the target-out ^{56}Fe beam in the trigger detector and air (assumed to be at approximately sea level) were calculated and the LET in dE1 and dE2 were found to be 148.213 keV/μm and 148.746 keV/μm, respectively. The measurements in dE1 and dE2 were then rescaled to an equivalent LET (in H_2O) using the equation,

$$LET_t(\Delta E) = LET_t(Fe) \frac{\Delta E_t}{\Delta E_t(Fe)}. \tag{6.3}$$

The resulting LET spectrum for the 10cm target block is shown as an example in Figure 6.4. A distinct peak corresponding to the surviving iron primaries is seen at approximately 155 keV/μm. Fragments are then distinguishable by the sharp separations starting at 140 keV/micron corresponding to ion species $Z = 25$ to $Z = 12$.

The number of each species was then determined by counting the events between each distin-

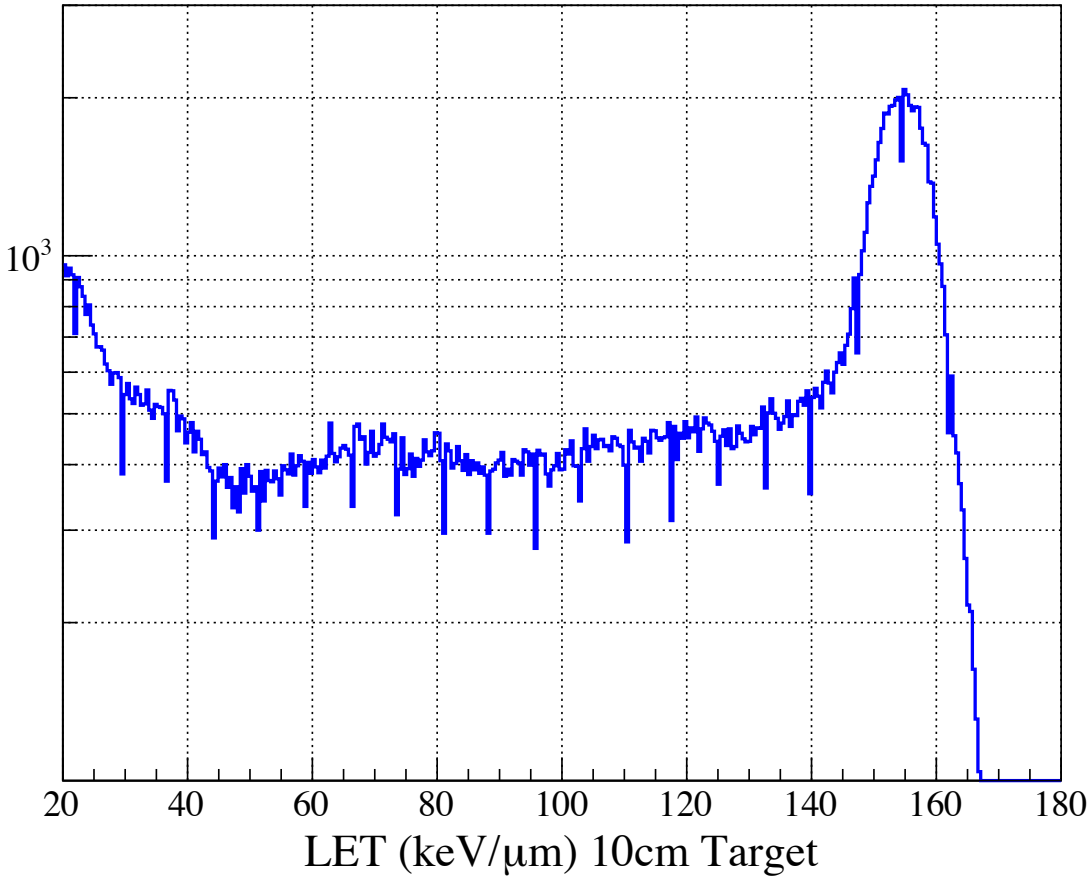

Figure 6.4: **Histogram of the 10 cm polyethylene target block scaled to the matching measured LET in dE1 and dE2.** The primary Iron peak is seen at 155 keV/μm and distinguishable delimitations starting at 140 keV/μm corresponding to ion species $Z = 26$ to $Z = 12$

guishable peak. Charges of $Z = 12$ to $Z = 26$ were measured in the 10cm target and charges of $Z = 15$ to $Z = 26$ in the 20cm target. For these targets, the resolution of successive energy losses by a particle in the dE detectors was usually sufficient to identify the higher-Z nuclei emerging from the target blocks. For both targets, approximately 34% and 11%, respectively, of the primary ions were expected to survive without a charge changing reaction, providing a distinct iron peak.

Charge species $Z = 16$ to $Z = 18$ were identifiable for the 30cm target block, while charges $Z = 11$ to $Z = 12$ were obtained from the 40cm target. In the 30cm target block, there are no discernible peaks below approximately 85 keV/μm, which corresponds to the expected mean LET

of $Z \leq 13$. In the 40 cm target block, there are no discernible peaks below approximately 40 keV/μm, corresponding to the expected mean LET for $Z \leq 9$.

The inability to identify lower charges can be attributed to the target thickness, detector resolution, and to some degree, the large acceptance angle of the dE detectors. Silicon detectors would have provided a higher degree in resolution, however, would be saturated at the very high spill rate (e.g., 10^6 ions/spill). As the target thickness increased, the higher-Z nuclei were slowed at greater relative rates than lighter progeny fragments, resulting in more separation between mean LET values. The effect, subsequently also makes it more difficult to identify higher-Z fragments as the target thickness increased. For example, in the 30 cm block, calculations using Monte Carlo, demonstrated that the expected mean LET for charges $5 \leq Z \leq 12$ were between 15 keV/μm to 40 keV/μm. In contrast, for charges $13 \leq Z \leq 22$, the mean LETs are between 60 keV/μm and 258 keV/μm.

An example of this is shown in Figure 6.5 for carbon ($Z = 6$) and argon ($Z = 18$) progeny fragments emerging from a 30 cm polyethylene target block. The heavier argon nuclei are slowed more rapidly than the lighter carbon nuclei resulting in a larger breadth of measured LETs in scintillator detectors downstream of the target block. A sharp peak at approximately 14 keV/μm is easily identified for the energy deposition of the carbon nuclei. In contrast, the argon nuclei with a mean energy loss of approximately 120 keV/μm is washed out by the large spread in measured energy depositions (e.g., 100 keV/μm - 300 keV/μm).

Additionally, the larger acceptance angle allowed for more combinations of light fragments hitting the detector simultaneously causing overlapping ΔE distributions and resulting in energy deposition equal to the sum of each of their energies. Both of these effects are exacerbated as the target thickness and detector acceptance increased.

An additional energy discrimination cut using the CAL detector provided charge identification for the events previously not determined by correlating the energy depositions in the dE calorimeter detectors. A lookup table was created with the calculated values of the mean energy depositions of a particle traversing successively through dE1, dE2 and CAL. This was done for ions with charges

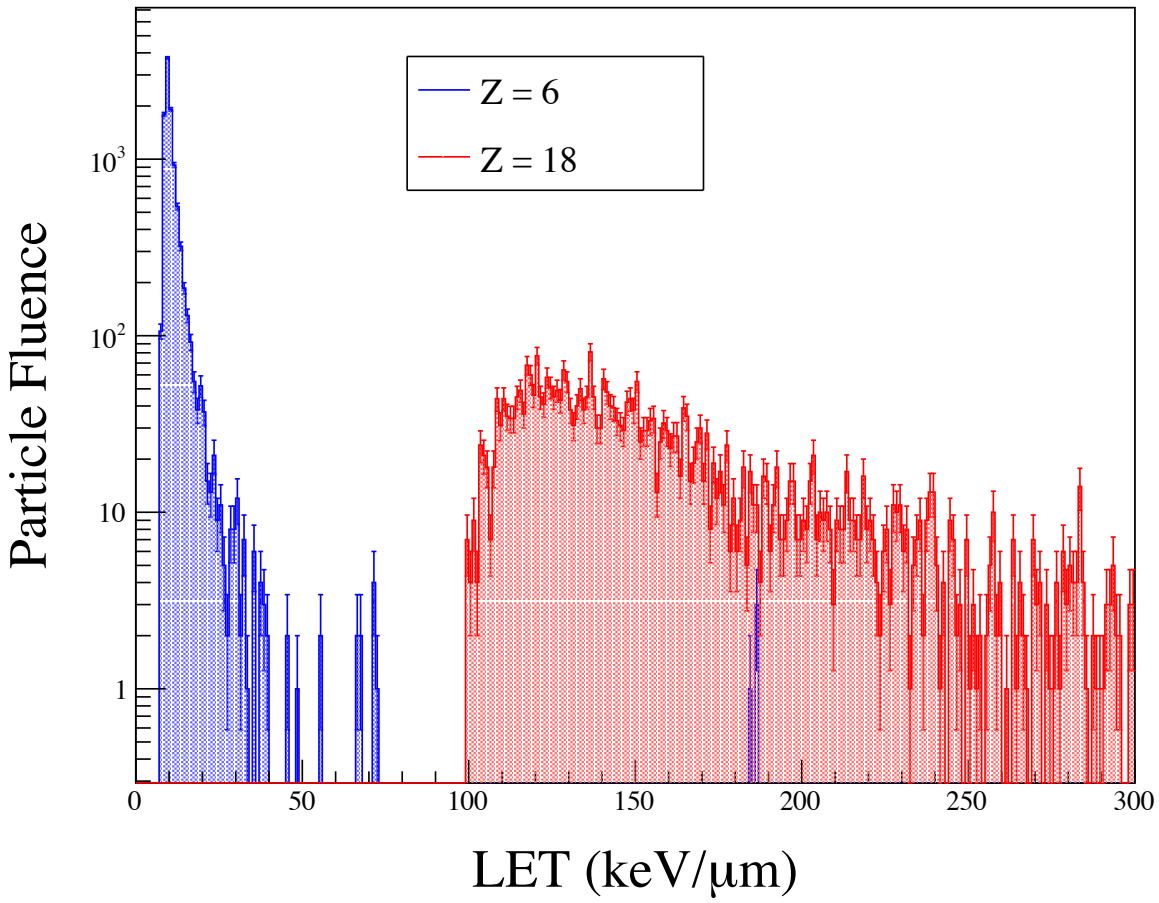

Figure 6.5: **The LET distributions for charges Z=6 (blue) and Z=18 (red) in the 30 cm target block.** Figure demonstrates how the LET disperses as the charge increases, making it difficult to distinguish the heavier ions with measurements from detectors at terrestrial simulators.

$1 \leq Z \leq 26$ with energies 10 MeV$\leq E \leq E_{\max}$. Here the maximum energy for a charge species, $E_{\max}$, was determined using equation (2.7) and compared to Monte Carlo calculations for additional validation. The energy depositions of each measured event was then compared to the calculated values using a computational algorithm. The threshold for a positive species identification was all three measured values falling within the mean energy deposition defined in equation (2.20). In a small percentage of cases (< 10%), it was possible that the measured energy depositions corresponded to one or more charges. This was resolved by determining the mean variation in total energy deposition for all three detectors, and then selecting the lowest value.

The fluence of particles was determined by summing up the values of $n(Z)$ and corrected for attenuation by charge-changing reactions caused by traversing dE1 and dE2. To perform this last correction, the survival probability was calculated for each species using,

$$P_s = e^{-\Delta x \, \frac{\sigma(Z) N_{\mathrm{A}}}{A_{\mathrm{T}}}}, \tag{6.4}$$

where Δx is the width of dE1 and dE2, N_{A} is the Avogadro constant, A_{T} is the atomic mass of the target material, and $\sigma(Z)$ is the geometric cross-section determined with:

$$\sigma(Z) = 0.86\pi \left[(A_{\mathrm{PF}} + 0.5)^2 - (A_{\mathrm{PF}} - 0.5)^2 \right. \tag{6.5}$$

Here A_{PF} is the pre-fragment atomic number of the ion Z [17]. The corrected fluence for each ion species is then found by:

$$n'(Z) = \frac{n(Z)}{P_s}, \tag{6.6}$$

and fraction of events by charge, $f(Z)$, normalized to the total events, N:

$$f(Z) = \frac{n'(Z)}{N}. \tag{6.7}$$

This provides the fluence, per event as a function of species Z. The measured fluence for each target block is listed in Table 6.1.

Systematic errors are the dominating source of uncertainties with these type of measurements. Any variations in target center energy would be dependent on the beam energy at the point of extraction from the main accelerator source. The results presented assume a mono-energetic beam source where the primary energy was determined using equation (2.7), calculating the energy loss in all materials up to the target blocks. This accounts for mass upstream of the target block and air attenuation. NSRL reports beam uniformity to within $\pm$ 2%. The largest source of systematic errors, however, can be attributed to the determination of cut contours around the fragment energy

Table 6.1: **Measured particle fluence for the 10 cm, 20 cm, 30 cm, and 40 cm target blocks.**

Charge (Z)	**Fluence**$\times 10^{-3}$			
	10 cm	**20 cm**	**30 cm**	**40 cm**
4	–	–	62.969 $\pm$ 2.5	126.87 $\pm$ 5
5	7.0 $\pm$ 1.70	19.88 $\pm$ 0.795	133.67 $\pm$ 5.3	241.95 $\pm$ 9.7
6	12.9 $\pm$ 1.095	34.41 $\pm$ 1.29	175.09 $\pm$ 7	266.076 $\pm$ 10.7
7	11.0 $\pm$ 1.0	40.66 $\pm$ 1.63	138.229 $\pm$ 5.5	173.63 $\pm$ 6.94
8	9.76 $\pm$ 1.02	42.03 $\pm$ 1.68	103.45 $\pm$ 4	107.78 $\pm$ 4.3
9	7.5 $\pm$ 1	39.02 $\pm$ 1.56	87.3 $\pm$ 3	81.7 $\pm$ 3.3
10	11.7 $\pm$ 1.11	30.82 $\pm$ 1.22	76.81 $\pm$ 3	61.4 $\pm$ 2.45
11	8.12 $\pm$ 1	30.86 $\pm$ 1.22	75.8 $\pm$ 3	41.49 $\pm$ 1.65
12	16.8 $\pm$ 2.46	31.14 $\pm$ 1.25	78.47 $\pm$ 3	19.78 $\pm$ 0.79
13	8.13 $\pm$ 1.86	35.37 $\pm$ 1.41	67.74 $\pm$ 3	5.03 $\pm$ 0.2
14	12.8 $\pm$ 1	36.9 $\pm$ 1.48	36.13 $\pm$ 1.5	5.03 $\pm$ 0.2
15	10.3 $\pm$ 1.8	49.8 $\pm$ 1.99	9.37 $\pm$ 1	–
16	11.3 $\pm$ 1.7	64.5 $\pm$ 2.58	13.14 $\pm$ 1	–
17	11.2 $\pm$ 1.1	46.36 $\pm$ 1.85	3.98 $\pm$ 1	–
18	20.2 $\pm$ 2.0	57.63 $\pm$ 2.31	–	–
19	16.6 $\pm$ 2.1	31.12 $\pm$ 1.24	–	–
20	25.9 $\pm$ 3.13	36.12 $\pm$ 1.44	–	–
21	11.5 $\pm$ 1.61	37.17 $\pm$ 1.49	–	–
22	27.9 $\pm$ 2.31	50.15 $\pm$ 2.01	–	–
23	15 $\pm$ 1.97	65.05 $\pm$ 2.6	–	–
24	19.1 $\pm$ 2.44	46.7 $\pm$ 1.87	–	–
25	21.4 $\pm$ 5.33	57.93 $\pm$ 2.312	–	–
26	82.6 $\pm$ 1.87.	118.39 $\pm$ 4.73	–	–

depositions in dE1 and dE2 demonstrated in Figure 6.3. There is a degree of subjectivity in this method. Specifically, inconsistency in selecting those points that correspond to the primary ion can lead to variability in the fluence measurements. For the 10cm and 20cm targets, the surviving primary iron nuclei is easily distinguished in the figure. This is not true for the 30cm and 40cm targets, where the primary ion is stopped at depths shorter than the target thickness. Thus the error analysis was performed using the bootstrap technique described in section 4.4. This more conservative approach the led to slightly higher values of error in the 30cm and 40cm targets.

7. VALIDATION WITH BEAMLINE MEASUREMENTS

The beamline measurements taken with the 20 cm, 30 cm, and 40 cm targets allow for comparing the predictions of LET and ion species emerging from target blocks of the same material and similar depths as those used in the SSL model (Chapter 4). With the results reported here, we demonstrate a qualitative match between the measured LET and a reasonable approximation of progeny ions generated when the beamline measurements are compared with the PHITS Monte Carlo.

The LET energies measured for the fragments emerging from the 20 cm, 30 cm and 40 cm targets, are plotted in Figures 7.2(a), 7.3(a), and 7.4(a), and compared to the same as determined with PHITS. This is repeated for charge species in Figures 7.2(b), 7.3(b), and 7.4(b). For the LET measurements, there are significant differences in the spectra below approximately 40 keV/μm in the 20 cm target, and below approximately 50 keV/μ in the 30 cm and 40 cm targets. This can be attributed to the dE detector's relatively large angle acceptance (e.g. 7° – 9°) and the "pile up" of light fragments striking the detector in coincidence, resulting in an energy deposition equal to the sum of their energies[1]. This is demonstrated in Figure 7.1 where Zeitlin et al., compared the measured LET spectrum of a 1 GeV ^{56}Fe primary ion emerging from a 17 g/cm^2 (approximately 17.71 cm thick) CH_2 target block. In the measurements by Zeitlin et al., the detector acceptance angle, (e.g approximately $7.4°$) is comparable to those in our beamline measurements.

Additionally the sharp peaks in the PHITS model are noticeably smeared in the measured values for all beamline measurments shown in Figures 7.2(a), 7.3(a), and 7.4(a). This is likely because the target thickness is near or greater than the mean interaction length of iron nuclei in polyethylene. Lighter fragments emerge from the target block at higher velocities because of energy loss while traversing the target from the point of their production (*e.g.* the location of the spallation), causing a spread, ΔE, in the measured energy spectrum at dE1 and dE2.

[1]This is actually true for all measured events; however, when there is a sufficiently heavy leading fragment, it will dominate the summed energy.

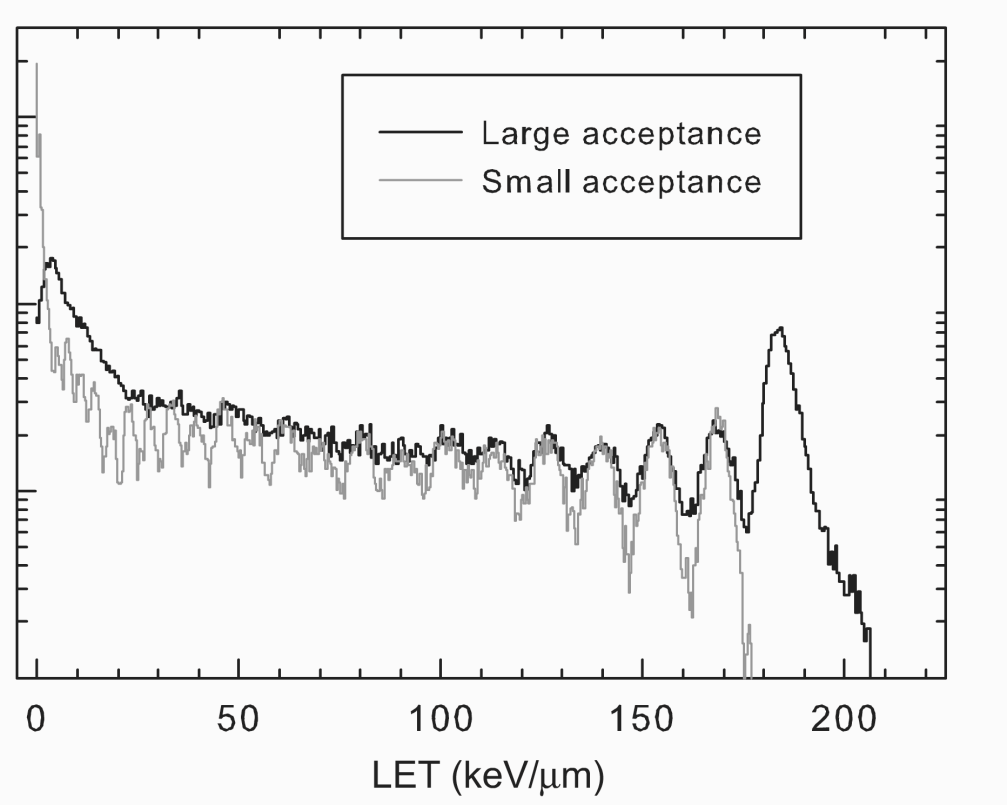

Figure 7.1: **Comparison of small angle versus large angle acceptance detector measurements** The measured LET by Zeitlin et al., demonstrates the difference in low-LET energy resolution between detectors with large angle and small angle acceptance [151]. In their data, the small angle detector acceptance is reported to be $1.2^\circ - 1.5^\circ$, while the large angle detector acceptance is $3.7^\circ - 8^\circ$. The difference in spectra for LET energies below 30 keV/μm is attributed to events with no leading heavy ion fragments. In the large acceptance detectors, this results in a higher probability of multiple light fragments striking the detectors in coincidence. This results in the energy of the individual fragments adding together and producing a pulse height proportional to the sum of the individual energies. Figure reprinted from Zeitlin et. al. 2008 [151], with permission from Elsevier.

7.1 20 cm Target Measurements

The 20 cm target, Figure 7.2(a), shows qualitative agreement between the beamline measurements when compared to the modeled LET spectrums. LET measurements for the $Z = 25$ and $Z = 26$ peaks are slightly separated with PHITS showing the peaks at approximately 174 keV/μm and 194 keV/μm, respectively. The measured LET spectrum indicates the corresponding $Z = 25$ and $Z = 26$ peaks are found at 168 keV/μm and 184 keV/μm, with the $Z = 25$ slightly skewed towards a lower LET. We attributed this to $Z = 25$ fragments produced in the blocks arriving

at the energies comparable to the surviving iron primaries, making it difficult to resolve them in the scintillator detectors measurements. This is also demonstrated in Figures 7.2(b), where the measured fluence of $Z = 25$ is higher than predicted by PHITS.

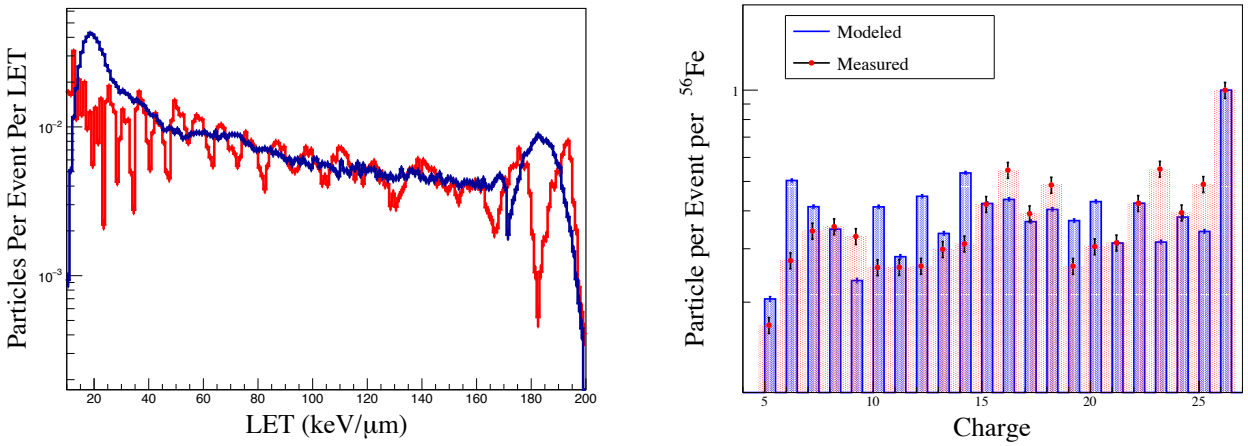

(a) LET distribution for the 20 cm target block

(b) Charge distribution for the 20 cm target block

Figure 7.2: **LET and charge species measurements for the 20 cm target.** In the left figure, the measured LET is plotted in blue, while the PHITS output is shown in red, while the measured versus modeled charge distribution for the 20 cm target block is shown on the right.

The measured fluence as a function of charge are shown in Figure 7.2(b) and compared to PHITS simulations of the experiment geometry. These are normalized to the most predominant measured ion species, iron, $Z = 26$. Charges as low as $Z = 4$ and $Z = 5$ up to the primary $Z = 26$ are seen in the results for the 20 cm target. As shown in Chapter 4, PHITS replicates the odd-event effect and predicts a slight preference for even versus odd progeny fragments [148, 149, 124, 125]. Figure 7.2(b) demonstrates a similar trend in the measured data for charges greater than $Z = 15$, however, this is muted for the lighter charge species. Additionally, the suppression of $Z = 9$ and enhancement of $Z = 14$ is not prominent in the measured data, while PHITS predicts both. The higher fluence of measured $Z = 9$ ions can perhaps be attributed to the corresponding suppression of measured versus predicted $Z = 6$ ions. The combination of lighter lithium ($Z = 3$) or $Z = 1, 2$

ions simultaneously arriving at the dE detectors will skew the measured charge species from $Z = 6$ towards $Z = 9$. This is also indicated by the previously discussed "pile up" of measured LET for values less than 25 keV/μ in the 20cm target (Figure 7.2(a)). Additionally, in Figure 7.2(a), the PHITS results show distinct peaks at LETS of approximately 27 keV/μ, 33 keV/μ, 39 keV/μ, and 45 keV/μ, corresponding to charges $Z = 10, 11, 12, 13$ respectively. This is not reflected in the beamline results and indicates that the lack of measurement resolution for the low LETs inhibits positive identification of ion species in the $Z = 10$ to $Z = 15$ range.

7.2 30 cm Target Measurements

The measured LETs for the 30 cm target is shown in Figure 7.3(a), while measured fluence as a function of charge are shown in Figure 7.2(b). The charge species are normalized to the most predominant measured ion species, carbon, $Z = 6$. Both the measured LET and charge spectrums are compared to PHITS simulations of the experiment geometry. The spectrum from the beamline measurements demonstrates qualitative agreement for LETs between approximately 50 keV/μm and 135 keV/μ. This is not reflected for LET energies less than $40 - 50$ keV/μm, and as discussed above, can be attributed to "pile up" of light fragments striking the detector in coincidence, resulting in energy deposition equal to the sum of their individual energies. Additionally, the highest LET seen in the beamline measurements is approximately 135 keV/μ, where PHITS predicts up to 180 keV/μ.

The 30 cm target has charge measurements down to $Z = 4$, but poor correlation for charges greater than $Z = 14$, where PHITS predicts similar fluences for charges $Z = 15$ through $Z = 18$. As discussed at the beginning of the chapter, the sharp peaks in the PHITS model are noticeably smeared in the measured values, making it difficult to distinguish the higher charge progeny fragment species. There is a subtle peak seen between approximately 116 keV/μ and 123 keV/μ in the beamline measurements for the $Z = 17$ progeny fragments, roughly corresponding to the PHITS prediction of 120 keV/μ and 128 keV/μ. Additionally, as shown in Figure 7.3(a), the lack of LET energies greater than approximately 137 keV/μm in the beamline measurements, corresponds the noticeable deficit of ion species with charges greater than approximately $Z = 17$, where the

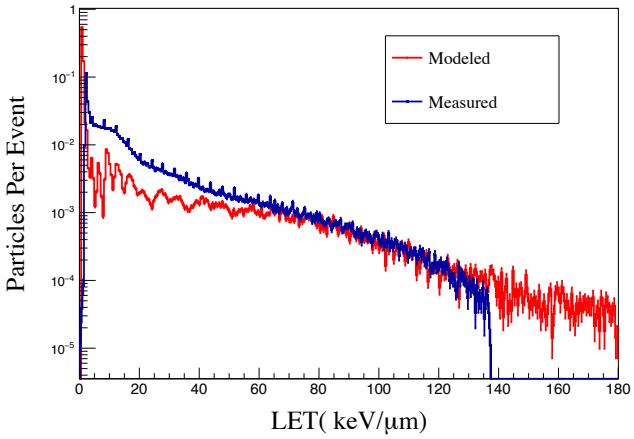

(a) LET distribution for the 30 cm target block

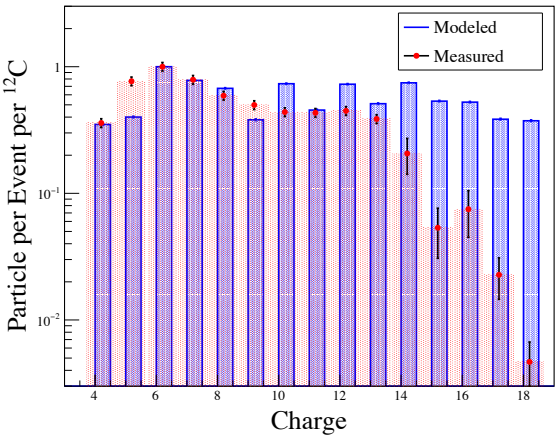

(b) Charge distribution for the 30 cm target block

Figure 7.3: **Measured versus modeled LET and charge distribution for the 30 cm target block** The measured LET is plotted in blue, while the PHITS output is shown in red. There is reasonably good agreement for LETs between 60 keV/μm and 130 keV/μ. An interesting detail is the suppression of events measured with LETs less than approximate 2 keV/μm. This corresponds to a relative enhancement of LETs between 3 keV/μm and approximate 50 keV/μm. This can be attributed to "pile up" of light fragments striking the detector in coincidence, resulting in energy deposition equal to the sum of their individual energies.

mean predicted LETs are 128 keV/μ and higher. This indicates that PHITs may over predict the generation of higher charge progeny nuclei.

7.3 40 cm Target Measurements

The measured LET for the 40 cm target block is shown in Figure 7.4(a) while the measured fluence as a function of charge is shown in Figure 7.4(b). These are both compared to PHITS simulations of the experiment geometry. The charge spectrum is again normalized to the most predominant measured ion species, carbon, $Z = 6$. The measured LET energies for the demonstrates trends similar to the 30 cm target, though slightly more pronounced, where there is a noticeable divergence between measured versus modeled spectrums for LETs less than approximately 50 keV/μm.

As shown in Figure 7.4(b), the beamline results have charge measurements down to $Z = 4$, but

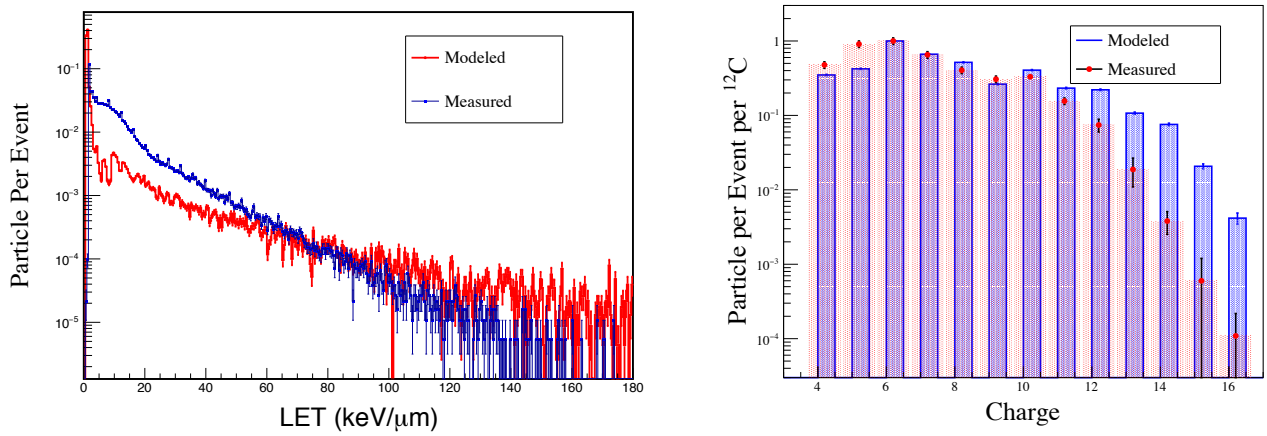

(a) LET distribution for the 40 cm target block

(b) Charge distribution for the 40 cm target block

Figure 7.4: **Measured versus modeled LET and charge distribution for the 40 cm target block** The measured LET is plotted in blue, while the PHITS output is shown in red. Similar to the 30 cmm target results presented in Figure 7.3(a), measurements of LETs from approximately 2 keV/μm to 50 keV/μm are much higher than what is predicted by PHITS. Higher resolution beamline measurements would be needed to ascertain whether this can be attributed to measurement technique or a deficiency in the PHITS transport code.

poor correlation for charges greater than $Z = 12$. The disparity in the species measured for charges approximately greater than $Z = 14$ corresponds to the poor measurement statistics for LETs greater than 100 keV/μ. There are corresponding peaks at LETs of approximately 65 keV/μm,77 keV/μm, and 89 keV/μm. These roughly correspond to the expected LETs for charges $Z = 11$, $Z = 12$, and $Z = 13$, indicating that the PHITS calculation underestimates the attenuation of higher surviving charges as greater target block depths.

7.4 Discussion

As discussed in the beginning of the section, some limitations on the measurement resolution do not allow for direct comparison to the Monte Carlo results presented in Chapter 4. These can be attributed to our access to beamtime, and limited time for *in situ* preparation and fine adjustment of target geometry. For example, as seen in Figure 6.1, the distance from the exit point of the target block to dE1 decreased with increasing target size. This occurred because target blocks were

quickly added in succession to the beam field and there was insufficient time to ensure that the Monte Carlo geometry was preserved. As 40-60 cm of air has roughly the same stopping power as 3-4 mm of tissue, imposing a theoretical geometric correction could lead to convoluted results and limits imposed in the interpretation of the results.

As a further limitation, the multiplicity of the particles exiting the target blocks was not captured and the fragmentation fluences and LET reported here are per event. One of the strengths of the model is the recognition of secondary fragments produced *per primary ion*. This allows for matching the the integrated LET rate per day to the spill rate of the accelerated beams. For instance, the NSRL lists the maximum spill rate for 1 GeV iron ions as approximately 5^8 ions per second. In the Space Shuttle simulation, approximately 5^8 primary ions were used to match the integrated LET rate per day as measured by Badhwar et al. At this spill rate, results can provide the equivalent daily dose-rate every single second. When compared to a measured spectrum from the ISS, this would be an equivalent dose rate of 36 mSv/min. In other words, 6.1 minutes of exposure at the NSRL (or any equivalent heavy-ion accelerator) would be equivalent to the projected exposure of an astronaut spending one year onboard the ISS. In fact, the approximate integrated dose for a one-year mission on board the ISS in LEO is approximately 200-250 mSv. Assuming a controlled reduction of the beam spill rate at the NSRL, it is very feasible to assume that a significantly lower dose-rate can be achieved. This is one of the greater strengths of this approach to a ground-based space radiation analog.

Finally, additional dE detector pairs, preferably one set farther downstream of the target blocks, would have allowed for additional corrections and higher measurement resolution of charge distributions with smaller acceptance angles on detector measurements. For larger acceptance measurements, specifically those take with the 30cm and 40cm targets, there is a high probability of simultaneous impact by multiple light fragments. Event-by-event recordings sum the energy deposited by multiple light fragments and record it as a single hit. There are many combinations of fragment ion species and the measured spectrum becomes unresolved in regions of lower charge. Additional detector pairs would allow for discriminating these events by comparing pulse height

measurements.

These points preclude a high-fidelity comparison with the Monte Carlo results of the Space Shuttle model discussed in Chapter 4. Validation of a computational model should heavily favor experimental parameters that exactly mimicked those in the model, though this was not entirely feasible in the experimental design discussed in Chapter 6. However, the results presented here were compared with PHITS simulations that demonstrated qualitative agreement with the measurements taken at the NSRL. In each case, the measured LET, ion species, and fluence for the 20cm, 30cm, 40cm polyethylene target blocks were comparable to those found in the PHITS simulations. This suggest that it is reasonable to infer our approach is physically valid, but further work would solidify the computational verification.

8. CONCLUSION AND FUTURE WORK

8.1 Conclusion and Future Work

Our understanding of the space radiation environment and the risk it poses to long-duration astronauts remains limited. There is a disparity between research results and observed empirical effects seen in human astronaut crews, in part due to the numerous factors that limit terrestrial simulation of the complex space environment and extrapolation of human clinical consequences. Given the intended future of human spaceflight, with efforts now to rapidly expand capabilities for human missions to the moon and Mars, there is a pressing need to improve upon the understanding of the space radiation risk, predict likely clinical outcomes of interplanetary radiation exposure, and develop appropriate and effective mitigation strategies for future missions.

The clinical utility of models for predicting the dose-toxicity response to space radiation in astronauts are limited by radiobiology studies using analogs of mono-energetic beams (e.g., Li, C, O, Si, Fe) where the entire projected dose for an exploration-class mission is given to animal models using high dose-rate exposures. These exposures reflect neither the low dose-rate nor the complex energetic and ionic make up of GCR radiation, and *in vivo* experiments with such beams are unlikely to accurately model the potential multi-organ toxicity of GCR radiation [57]. The differences in the RBE of different heavy ions are primarily attributed to differences in the LET spectra of the radiation [41]. While the specific ion species depositing dose may have biological significance, the LET distribution created by the intrinsic properties of these ion species is most critical when determining the biological response. Here, the LET serves as the basis of radiation protection and risk assessment in mixed radiation exposure scenarios [5, 41].

Given the extensive evidence to the inadequacy of terrestrial radiobiological experimental design presented throughout this manuscript, we conclude that the previous radiobiological models and experiments utilizing mono-energetic beams have not fully characterized the biological responses or described the impact of space radiation on the health of human tissues and organ systems. I sought

to address these limitations with the development of a ground-based space radiation analog that closely resembles the complex intravehicular radiation environment. As demonstrated in Chapters 3 and 4, the moderator block model shows that the intrinsic properties of hydrogen-rich crystalline materials can preferentially produce specific nuclear spallation and fragmentation processes when placed in an accelerated heavy-ion beam allowing for a continuous generation of ionizing radiation. The perturbation of their micro-structure can influence the materials capability to simultaneously generate the complex mix of nuclei and energies found in the GCR spectrum. The numerical simulations indicate that this approach provides a significantly more robust and accurate recreation of the space radiation environment for experiments with ground-based analogs.

The confirmation of the hypothesis and the utility of the model depends on how accurately it captures features measured in laboratory experiments and how accurately it predicts reproducible measurements. Initial validation of the numerical results is an important step. The methods used in this model show qualitative agreement with beamline measurements found in peer-reviewed literature when adapted to a geometry and environment representative of the experiment setup. We approximated the relative abundance of progeny fragments and surviving ^{56}Fe projectiles that were generated in CH_2 targets, as measured in the experiments by Zeitlin et al. Agreement was shown in single-species compounds (e.g., aluminum, $Z = 13$, and lead, $Z = 82$), including the visible preference for even charged progeny, as demonstrated by Zeitlin et al. and previous experiments [150, 125]. This provided a initial indication that the model could be capable of replicating the mechanisms of charge-changing interactions.

Additional validation was performed with beamline measurements made at the NSRL, discussed in Chapters 6 and 7. Beamline measurements demonstrated qualitative agreement in the prediction of charge and LET distributions for a 1 GeV/n iron beam accelerated at polyethylene targets of $10 - 40$ cm when compared to the SSL model discussed in Chapter 4. Limitations in the experiment framework preclude a direct comparison to the computational model. However, Monte Carlo simulation adjusted to the experiment parameters demonstrates qualitative agreement with both the fragment fluence and LET distributions from the beamline measurements. This allows, to first order,

the conclusion that our simulated model reflects physical reality.

Beamline measurements are needed in order to determine whether the discrepancies observed in the analysis described in Chapter 7 are attributed to measurement resolutions or to the SSL simulation. Additionally, several discrepancies between the spectrum resulting from beam-line simulation still remain to be resolved. GCR models imply that over 90% of particle fluence is found below a LET of about 0.5 keV/μm. The Monte Carlo techniques used for the beamline simulation transports under-represents the lighter, low LET ions. It is not yet known how well the target design fills in the LET distribution for particles $\leq$ 5 keV/μm. I predict that, based on past calculations, any discrepancies may be solved by adjusting the geometry and/or atomic composition of the proposed target moderators.

I would be remiss without addressing the issue of the resulting LET distribution in humans. One key hypothesis driving the necessity of this space radiation analog is the accurate reflection of dose distributions that account for the relative dose depositions in organ systems. This is critical for the accurate determination of biological response. The dose distribution that a human would incur if exposed to a proton energy spectrum representative of a very large SPE (In this case, the Sept 1989 event) is demonstrated in Figure 8.1. This figure was created using Monte Carlo to reproduce the 1989 SPE dose distribution superimposed over a clinical MRI scan of a human. This demonstrates that, for even a single ion, multi-energy distribution alters the intensity of stress placed on organ systems.

Our approach at addressing the need for ground-based space radiation analogs is thus incomplete without moderator blocks that could reproduce the dose deposition of the LET field measured in humans to a comparable dose deposition in the animal models (e.g. rodent, pig, primate, etc) as discussed in Chapter 2. I would prioritize addressing this deficit over any previously mentioned. It would be an important next step to create scalable moderator blocks; it is likely that these could be fabricated at the Texas A&M Cyclotron center in parallel to further validation efforts. With this capability, biological endpoints could be evaluated in increasingly complex animal systems to study precursors for a few very specific outcomes predicted to occur in humans during long-

duration spaceflight. These could then be compared to specimens taken during previous flights onboard the ISS and extrapolated to determine a dose-threshold for human biological response. This would not only provide the first clinical correlations for space radiation health in humans but would also take advantage of a valuable U.S. laboratory asset immersed in the space radiation environment. Additionally, we now have the benefit of a larger, cumulative astronaut population that has flown in space while exposed to a variety of doses that exceed the presumed thresholds for some degenerative and carcinogenic outcomes. The health of these astronauts, including early indicators of disease, is closely monitored by NASA medical and epidemiological resources with yearly medical examinations and careful records of clinical outcomes. This provides critical, real human data that could be used to evaluate these results and study the actual long-term health risk of space radiation. The additional application of this source of data could enhance our understanding of the true risk of space radiation, the characterization of human clinical outcomes, and the development of appropriate mitigation strategies [8].

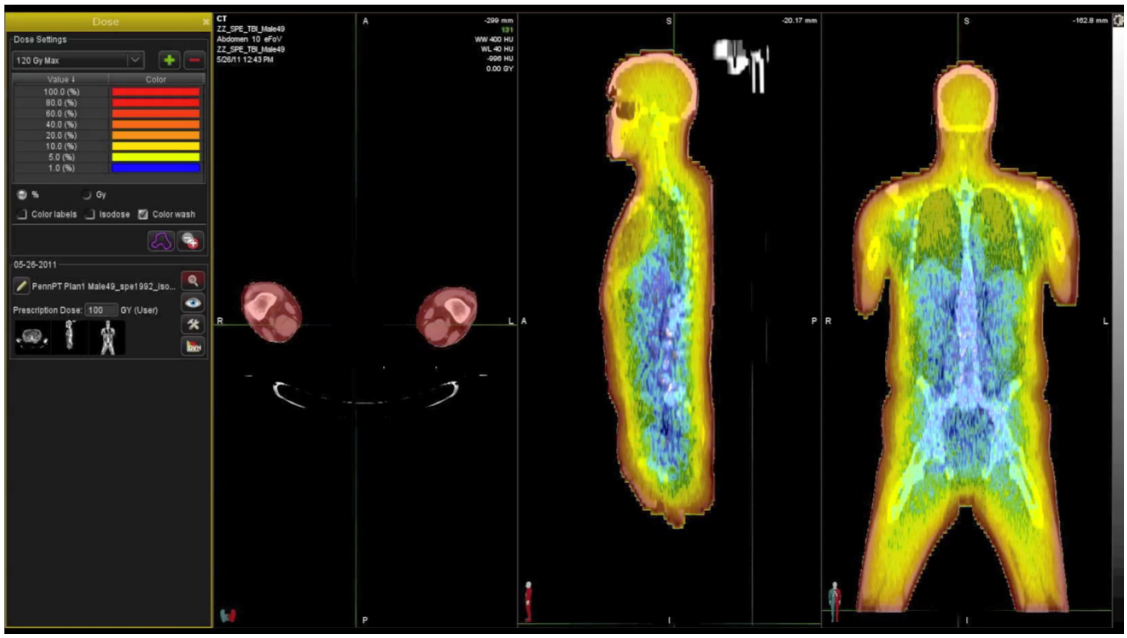

Figure 8.1: **Projected dose distribution in human following large SPE exposure**. In the figure, the shading indicates relative intensity of dose deposition with red being the worst. This demonstrates that dose deposition widely varies and simultaneously instigates varying degrees of stresses to multiple organ systems. Image courtesy of Keith Cengel, University of Pennsylvania.

The next step and a pressing need in this research would be high fidelity beamline measurements. With good planning, a complete approach would involve several measurements of the polyethylene target block lengths discussed in Chapter 6. Beam-line measurements would be done over the course of $2-3$ consecutive days. Additional pairs of dE/dx detectors, giving three or more total sets, would allow for multiple levels of species discrimination and accurate identification of ion species. Beam spills should be moderated, allowing for determining particle fluence and LET spectrum normalized to the number of primary iron ions. This would provide accurate fragmentation cross-sections that can be directly and rapidly compared to those in the simulations. If needed, the projected moderated block geometry could then be incrementally modified using additional polyethylene blocks of length $1-2$ cm until there was good agreement between measurement and simulation data. Assuming measurements were again being performed at the NSRL, the projected moderated block geometry could then be fabricated at the laboratory machine shop for final validation.

Additional next steps should be the measurements of the LET and particle spectrum for increasing scatter angles up to approximate 20° are also needed. It has been presumed that the measurement of particle species were performed along the line of the primary ion's path. This provides minimal information about the homogeneity of the resulting field at angles greater than the detectors. Homogeneity could then be adjusted by adding thin layers of high-Z materials (such as lead) to increase the scattering angles of progeny fragments created in the target blocks. Energy loss differences because of the additional mass could be accommodated with small adjustments to the polyethylene blocks so that the total areal density remains approximately constant.

Previously, due to resource limitations, historical radiation risk models rely heavily on deterministic code as a mathematical solution to describe how various particles travel through a given material. These historical models have limited ability to accurately replicate and track secondary, tertiary, and higher-order nuclear interactions. The common historical model used for most space radiation studies are a one-dimensional straight-ahead approximation of particle transport that lacks the sophistication and inherent capability of PHITS and other more modern and advanced 3D Monte Carlo programs (e.g. FLUKA (Fluktuierende Kaskade) and GEANT (Geometry and

Tracking) Simulation Programs, see Appendix A.1). An important outcome of the results discussed in Chapters 4 - 7 is the validity for using 3-D Monte Carlo particle transport codes for determining complex physical outcomes using high-performance, multi-core computers. The results demonstrate computational alternatives of complex dynamics that are difficult to mimic in a laboratory setting. The recent advances in multi-core computation techniques allow for decreasing statistical errors by drastically increasing the number of samples sets. For example, the simulation results reported in Chapter 4 required massive computation resources. Each model (Shuttle, ISS, EFT-1) utilized the equivalent of 135,000 cpu hours (about 2.5 years on a desktop or laptop computer) and generated 2.5 TB of data using 5000 cores. These computations were performed in roughly 10 hours. Remarkably, recent updates to the high performance computing cluster reduced the same computational time to approximately 10 minutes.

This immediately points to application of high performance computational techniques and the adaptation of the moderator block to the rapidly maturing use of heavy-ion beams in radiotherapy. Carbon ions are successfully being used in Japan and in Europe as alternative cancer treatment. The unique interaction of heavy charged particles with materials (e.g., tissue) that creates so much difficulty in space radiation health protection, is leveraged to an advantage for delivering a penetrating energy to deep-seated tumors. An important issue remaining with carbon therapy is the localization of applied radiation fields to the tumors being treated. Fragmentation of the carbon ions can cause secondary damage to healthy neighboring tissues and organs. In theory, it should be possible to create the spallation fields using a carefully crafted moderator block that could be used to study the dynamics in tissue and organ models.

Finally, our model can provide a new robust method to test the impact of cosmic ray radiation on hardware that support both commercial satellite and space vehicle systems. This unique capability can facilitate the customization of the analog environment for ground based validation and countermeasure testing (e.g., low/high altitude satellites in polar, equatorial or geosynchronous orbits, spaceflight vehicles in LEO or interplanetary spaceflight). This can provide significant advances that can increase reliability in space manufacturing processes while reducing cost and enabling new

spaceflight capabilities.

In conclusion, our model leverages available technologies to provide an enhancement to current ground-based analogs of the space radiation environment by reproducing the measured intravehicular LET spectrum. While NASA is proposing a GCR simulator that will provide three to five consecutive mono-energetic heavy ions, such an approach only provides a few LET data points (see Figure 1.2) and lacks the generation of pions and neutrons that account for 15-20% of a true space radiation dose [154]. Additionally, questions still remain on what order the ion species should be delivered since this can affect the outcomes of the experiment [155, 156]. As a contrasting approach, we have demonstrated a more accurate modeled replication of the spectrum measured in previous spaceflight, including onboard the U.S. Space Shuttle, ISS, and the Orion Crew Vehicle. Validation of these results with beamline measurements, both from the peer-reviewed literature and as performed herein, demonstrate qualitative agreement with model predictions. This is highly relevant to current U.S. space exploration efforts.

The ability to recreate the space radiation environment in terrestrial research efforts, as demonstrated here, would significantly boost the understanding of the space radiation environment, allowing for rapid advances in the understanding of human radiobiological health during long-duration spaceflight while drastically cutting costs and reducing risks involved in radiobiological research efforts. These results address a pressing need for better understanding of the true health risk imposed by the space radiation environment on future human exploration missions. Our approach can be generalized to other radiation spectra and is therefore of wide applicability for general radiation studies, not just of biological material, but also for the deployment of shielding, electronics, and other materials in a space environment. Additionally, our approach can also be utilized to emulate the external GCR field, the planetary surface spectrum (e.g., Mars), and the local radiation environment of orbiting satellites. This provides the first instance of a true ground-based analog for characterizing the effects of space radiation.

REFERENCES

[1] NCRP, *Guidance on radiation received in space activities*. NCRP Report No. 98, 1988.

[2] NCRP., *Radiation Protection for Space Activities: Supplement to Previous Recommendations*. NCRP Commentary No. 23, 2015.

[3] NASA, "Nasa spaceflight human-system standard," Tech. Rep. NASA-STD-3001 VOL 1 REV A, Washington, DC, 2015.

[4] J. C. Chancellor, G. B. Scott, and J. P. Sutton, "Space radiation: the number one risk to astronaut health beyond low earth orbit," *Life*, vol. 4, p. 491, 2014.

[5] S. A. Walker, L. W. Townsend, and J. W. Norbury, "Heavy ion contributions to organ dose equivalent for the 1977 galactic cosmic ray spectrum," *Advances in Space Research*, vol. 51, pp. 1792–1799, May 2013.

[6] J. E. Turner, *Atoms, radiation, and radiation protection*. John Wiley & Sons, 2008.

[7] G. D. Badhwar, W. Atwell, B. Cash, V. M. Petrov, Y. Akatov, I. V. Tchernykh, V. A. Shurshakov, and V. A. Arkhangelsky, "Radiation environment on the Mir orbital station during solar minimum," *Adv Space Res*, vol. 22, no. 4, pp. 501–510, 1998.

[8] J. C. Chancellor, R. S. Blue, K. A. Cengel, S. M. Auñón-Chancellor, K. H. Rubins, H. G. Katzgraber, and A. R. Kennedy, "Limitations in predicting the space radiation health risk for exploration astronauts," *Nature Microgravity*, vol. 4, apr 2018.

[9] A. R. Kennedy, "Biological effects of space radiation and development of effective countermeasures," *Life Sciences in Space Research*, vol. 1, p. 1, 2014.

[10] A. L. Romero-Weaver, X. S. Wan, E. S. Diffenderfer, L. Lin, and A. R. Kennedy, "Effect of SPE-like proton or photon radiation on the kinetics of mouse peripheral blood cells and radiation biological effectiveness determinations," *Astrobiology*, vol. 13, p. 570, 2014.

[11] J. W. Norbury, W. Schimmerling, T. C. Slaba, E. I. Azzam, F. F. Badavi, G. Baiocco, E. Benton, V. Bindi, E. A. Blakely, S. R. Blattnig, D. A. Boothman, T. B. Borak, R. A. Britten, S. Curtis, M. Dingfelder, M. Durante, W. S. Dynan, A. J. Eisch, S. Robin Elgart, D. T. Goodhead, P. M. Guida, L. H. Heilbronn, C. E. Hellweg, J. L. Huff, A. Kronenberg, C. La Tessa, D. I. Lowenstein, J. Miller, T. Morita, L. Narici, G. A. Nelson, R. B. Norman, A. Ottolenghi, Z. S. Patel, G. Reitz, A. Rusek, A.-S. Schreurs, L. A. Scott-Carnell, E. Semones, J. W. Shay, V. A. Shurshakov, L. Sihver, L. C. Simonsen, M. D. Story, M. S. Turker, Y. Uchihori, J. Williams, and C. J. Zeitlin, "Galactic cosmic ray simulation at the NASA Space Radiation Laboratory," *Life Sci. Space Res.*, vol. 8, pp. 38–51, Feb. 2016.

[12] T. C. Slaba, S. R. Blattnig, J. W. Norbury, A. Rusek, C. La Tessa, and S. A. Walker, "Gcr simulator reference field and a spectral approach for laboratory simulation," Tech. Rep. NASA/TP-2015-218698, 2015.

[13] J. C. Chancellor, S. Guetersloh, K. Cengel, J. Ford, and H. G. Katzgraber, "Emulation of the space radiation environment for materials testing and radiobiological experiments," *arXiv preprint arXiv:1706.02727*, 2017.

[14] X. Elmore, R. Kapadia, M. Swete, and J. Redpath, "Neoplastic transformation in vitro by mixed beams of high-energy iron ions and protons," *Radiat. Res.*, vol. 176, no. 3, pp. 291–302, 2011.

[15] E. Rutherford, "The Scattering of α and β Particles by Matter and the Structure of the Atom," *Philosophical Magazine*, vol. 92, p. 379, 2012.

[16] H. Bradt and B. Peters, "The heavy nuclei of the primary cosmic radiation," *Physical Review*, vol. 77, no. 1, p. 54, 1950.

[17] L. W. Townsend and J. W. Wilson, "Energy-Dependent Parameterization of Heavy-Ion Absorption Cross Sections," *Radiation Research*, vol. 106, p. 283, 1986.

[18] ICRU, "Report 60, Recommendations of the International Commission of Radiation Protection," tech. rep., 1991.

[19] J. W. Wilson, R. C. Thibeault, F. A. Cucinotta, M. L. Shinn, M. H. Kim, R. Kiefer, and F. F. Badavi, "Issues in protection from galactic cosmic rays," *Radiat. Environ. Biophys*, vol. 34, p. 217, 1995.

[20] E. J. Hall, A. J. Giaccia, *et al.*, *Radiobiology for the Radiologist*, vol. 6. Lippincott Williams & Wilkins Philadelphia:, 2006.

[21] N. A. Schwadron, J. B. Blake, A. W. Case, C. J. Joyce, J. Kasper, J. Mazur, N. Petro, M. Quinn, J. A. Porter, C. W. Smith, S. Smith, H. E. Spence, L. W. Townsend, R. Turner, J. K. Wilson, and C. Zeitlin, "Does the worsening galactic cosmic radiation environment observed by CRaTER preclude future manned deep space exploration?," *J. Space Weather*, vol. 12, pp. 622–632, Nov. 2014.

[22] F. H. Attix, *Introduction to radiological physics and radiation dosimetry*. John Wiley & Sons, 2008.

[23] J. A. Simpson, "Elemental and Isotopic Composition of the Galactic Cosmic Rays," *Annu. Rev. Nucl. Part. Sci.*, vol. 33, pp. 323–382, Dec. 1983.

[24] L. W. Townsend, F. A. Cucinotta, J. W. Wilson, and R. Bagga, "Estimates of HZE particle contributions to SPE radiation exposures on interplanetary missions," *Adv. Space Res.*, vol. 14, no. 10, pp. 671–674, 1994.

[25] C. E. Hellweg and C. Baumstark-Khan, "Getting ready for the manned mission to mars: the astronauts' risk from space radiation," *Naturwissenschaften*, vol. 94, no. 7, pp. 517–526, 2007.

[26] J. W. Wilson, F. Cucinotta, J. Shinn, L. Simonsen, R. Dubey, W. Jordan, T. Jones, C. Chang, and M. Kim, "Shielding from solar particle event exposures in deep space," *Radiat. Meas.*, vol. 30, no. 3, pp. 361–382, 1999.

[27] D. Smart and M. Shea, "Comment on estimating the solar proton environment that may affect mars missions," *Adv. Space Res.*, vol. 31, no. 1, pp. 45–50, 2003.

[28] S. Hu, M.-H. Y. Kim, G. E. McClellan, and F. A. Cucinotta, "Modeling the acute health effects of astronauts from exposure to large solar particle events," *Health Phys.*, vol. 96, pp. 465–476, Apr. 2009.

[29] J. Wilson, "Overview of radiation environments and human exposures," *Health Phys.*, vol. 79, no. 5, pp. 470–494, 2000.

[30] "Goddard space flight center." `https://cdaweb.sci.gsfc.nasa.gov/index.html/`. Accessed: 2017-10-30.

[31] M. S. Clowdsley, J. E. Nealy, J. W. Wilson, B. M. Anderson, M. S. Anderson, and S. A. Krizan, "Radiation protection for lunar mission scenarios," tech. rep., 2005.

[32] H. Wu, J. L. Huff, R. Casey, M.-H. Kim, and F. A. Cucinotta, "Risk of acute radiation syndromes due to solar particle events," TR NASA/SP-2009-3405, National Aeronautics and Space Administration, Johnson Space Center, 2008.

[33] R. A. Mewalt, "Interplanetary Particle Environment," tech. rep., 1988.

[34] F. A. Cucinotta, M.-H. Y. Kim, and L. Ren, "Evaluating shielding effectiveness for reducing space radiation cancer risks," *Radiat. Meas.*, vol. 41, pp. 1173–1185, Oct. 2006.

[35] P. M. O'Neill, "Badhwar-O'Neill galactic cosmic ray flux model – revised," *IEEE Trans. Nuc. Sci*, vol. 57, p. 3148, 2010.

[36] F. A. Cucinotta, W. Schimmerling, J. W. Wilson, L. Peterson, G. Badhwar, P. Saganti, and J. Dicello, "Space Radiation Cancer Risk Projections for Exploration Missions: Uncertainty Reduction and Mitigation," TR JSC-29295, National Aeronautics and Space Administration, Johnson Space Center, 2001.

[37] F. A. Cucinotta and M. Durante, "Cancer risk from exposure to galactic cosmic rays: implications for space exploration by human beings," *J.-Lancet Oncology*, vol. 7, pp. 431–435, May 2006.

[38] B. B. Rossi, *High-Energy Particles*. New York: Prentice-Hall, 1952.

[39] P. E. Hodgson, E. Gadioli, and E. Gadioli-Erba, *Introductory Nuclear Physics*. New York: Oxford Univ. Press, 1997.

[40] S. Guetersloh, C. Zeitlin, L. Heilbronn, J. Miller, T. Komiyama, A. Fukumura, Y. Iwata, T. Murakami, and M. Bhattacharya, "Polyethylene as a radiation shielding standard in simulated cosmic-ray environments," *Nucl. Instrum. Methods Phys. Res., Sect. B*, vol. 252, pp. 319–332, Nov. 2006.

[41] R. Mewaldt, A. Davis, W. Binns, G. de Nolfo, J. George, M. Israel, R. Leske, E. Stone, M. Wiedenbeck, and T. von Rosenvinge, "The Cosmic Ray Radiation Dose in Interplanetary Space - Present Day and Worst-Case Evaluations," in *ICRC2005*, vol. 2, (Pune, Maharashtra), pp. 101–104, 2005.

[42] N. C. on Radiation Protection and Measurements, "Report no. 153 - information needed to make radiation protection recommendations for space missions beyond low-earth orbit," tech. rep., 2006.

[43] F. A. Cucinotta, M.-H. Y. Kim, and L. Ren, "Managing lunar and mars mission radiation risks. part 1; cancer risks, uncertainties, and shielding effectiveness," 2005.

[44] A. Edwards, "RBE of Radiations in Space and the Implications for Space Travel," *Physica Med.*, vol. 17, no. Suppl 1, pp. 147–52, 2001.

[45] R. Setlow, *Radiation Hazards to Crews of Interplanetary Missions: Biological Issues and Research Strategies*. Washington, D.C.: National Academies Press, 1996.

[46] A. A. Edwards, "RBE of radiations in space and the implications for space travel," *Physica Medica*, vol. 17, p. 147, 2000.

[47] K. A. Cengel, E. S. Diffenderfer, S. Avery, A. R. Kennedy, and J. McDonough, "Using electron beam radiation to simulate the dose distribution for whole body solar particle event proton exposure," *Radiat. Environ. Biophys.*, vol. 49, pp. 715–721, Nov. 2010.

[48] P. B. Saganti, F. A. Cucinotta, J. W. Wilson, L. C. Simonsen, and C. Zeitlin, "Radiation climate map for analyzing risks to astronauts on the mars surface from galactic cosmic rays," *Space Sci. Rev.*, vol. 110, no. 1/2, pp. 143–156, 2004.

[49] J. D. Cherry, B. Liu, J. L. Frost, C. A. Lemere, J. P. Williams, J. A. Olschowka, and M. K. O'Banion, "Galactic Cosmic Radiation Leads to Cognitive Impairment and Increased aβ Plaque Accumulation in a Mouse Model of Alzheimer's Disease," *PLoS One*, vol. 7, p. e53275, Dec. 2012.

[50] V. K. Parihar, B. Allen, K. K. Tran, T. G. Macaraeg, E. M. Chu, S. F. Kwok, N. N. Chmielewski, B. M. Craver, J. E. Baulch, M. M. Acharya, F. A. Cucinotta, and C. L. Limoli, "What happens to your brain on the way to Mars," *Sci. Adv.*, vol. 1, pp. e1400256–e1400256, May 2015.

[51] M. Durante, K. George, H. Wu, and F. Cucinotta, "Karyotypes of human lymphocytes exposed to high-energy iron ions.," *Radiat. Res.*, vol. 158, pp. 581–590, 2007.

[52] M. Durante, K. George, G. Gialanella, G. Grossi, C. La Tessa, L. Manti, J. Miller, M. Pugliese, P. Scampoli, and F. Cucinotta, "Cytogenetic effects of high-energy iron ions: Dependence on shielding thickness and material.," *Radiat. Res.*, vol. 164, pp. 571–6, 2007.

[53] H. Wang and Y. Wang, "Heavier ions with a different linear energy transfer spectrum kill more cells due to similar interference with the ku-dependent dna repair pathway.," *Radiat. Res.*, vol. 182, pp. 458–461, 2015.

[54] B. Loucas and M. Cornforth, "The let dependence of unrepaired chromosome damage in human cells: a break too far?," *Radiat. Res.*, vol. 179, pp. 393–405, 2015.

[55] E. J. Hall and A. J. Giaccia, *Radiobiology for the radiologist*. Philadelphia, PA: Wolters Kluwer Health : Lippincott Williams and Wilkins, 2012.

[56] M. Billings, W. Yucker, and B. Heckman, "Body self-shielding data analysis," TR MDC-G4131, McDonald Douglas Astronautics Company West, 1973.

[57] J. W. Wilson, M. Kim, W. Schimmerling, F. F. Badavi, S. A. Thibeault, F. A. Cucinotta, J. L. Shinn, and R. Kiefer, "Issues in space radiation protection: galactic cosmic rays," *Health Phys.*, vol. 68, pp. 50–58, Jan. 1995.

[58] A. R. Kennedy, J. G. Davis, W. Carlton, and J. H. Ware, "Effects of Dietary Antioxidant Supplementation on the Development of Malignant Lymphoma and Other Neoplastic Lesions in Mice Exposed to Proton or Iron-Ion Radiation," *Radiat. Res.*, vol. 169, pp. 615–625, June 2008.

[59] H. Paganetti, "Nuclear interactions in proton therapy: dose and relative biological effect distributions originating from primary and secondary particles," *Phys. Med. Biol.*, vol. 47, pp. 747–764, Mar. 2002.

[60] J. D. Slater, "Clinical applications of proton radiation treatment at Loma Linda University: review of a fifteen-year experience," *Technol. Cancer Res. Treat.*, vol. 5, pp. 81–89, Apr. 2006.

[61] N. Tilly, J. Johansson, U. Isacsson, J. Medin, E. Blomquist, E. Grusell, and B. Glimelius, "The influence of RBE variations in a clinical proton treatment plan for a hypopharynx cancer," *Phys. Med. Biol.*, vol. 50, pp. 2765–2777, June 2005.

[62] C. O. Wambi, J. K. Sanzari, C. M. Sayers, M. Nuth, Z. Zhou, J. Davis, N. Finnberg, J. S. Lewis-Wambi, J. H. Ware, W. S. El-Deiry, and A. R. Kennedy, "Protective effects of dietary antioxidants on proton total-body irradiation-mediated hematopoietic cell and animal survival," *Radiat. Res.*, vol. 172, pp. 175–186, Aug. 2009.

[63] K. A. Cengel, E. S. Diffenderfer, S. Avery, A. R. Kennedy, and J. McDonough, "Using electron beam radiation to simulate the dose distribution for whole body solar particle event proton exposure," *Radiat. Environ. Biophys.*, vol. 49, pp. 715–721, Nov. 2010.

[64] J. K. Sanzari, X. S. Wan, A. J. Wroe, S. Rightnar, K. A. Cengel, E. S. Diffenderfer, G. S. Krigsfeld, D. S. Gridley, and A. R. Kennedy, "Acute hematological effects of solar particle event proton radiation in the porcine model," *Radiat. Res.*, vol. 180, pp. 7–16, July 2013.

[65] J. K. Sanzari, S. X. Wan, E. S. Diffenderfer, K. A. Cengel, and A. R. Kennedy, "Relative biological effectiveness of simulated solar particle event proton radiation to induce acute hematological change in the porcine model," *J. Radiat. Res. (Tokyo)*, vol. 55, pp. 228–244, Mar. 2014.

[66] M. P. Little, E. J. Tawn, I. Tzoulaki, R. Wakeford, G. Hildebrandt, F. Paris, S. Tapio, and P. Elliott, "A systematic review of epidemiological associations between low and moderate doses of ionizing radiation and late cardiovascular effects, and their possible mechanisms," *Radiat. Res.*, vol. 169, pp. 99–109, Jan. 2008.

[67] E. Lorenz and C. C. Congdon, "Radioactivity biologic effects of ionizing radiations," *Annu Rev Med*, vol. 5, no. 1, pp. 323–338, 1954.

[68] C. P. Miller and C. W. Hammond, "The role of infection in radiation injury," *Trans. Assoc. Am. Physicians*, vol. 63, pp. 155–160, 1950.

[69] I. U. Boone, K. T. Woodward, and P. S. Harris, "Relation between bactermia and death in mice following x-ray and thermal column exposures," *J. Bacteriol.*, vol. 71, pp. 188–195, Feb. 1956.

[70] G. S. Krigsfeld, A. R. Savage, P. C. Billings, L. Lin, and A. R. Kennedy, "Evidence for Radiation-Induced Disseminated Intravascular Coagulation as a Major Cause of Radiation-Induced Death in Ferrets," *IJROBP*, vol. 88, pp. 940–946, Mar. 2014.

[71] G. Krigsfeld, J. Shah, J. Sanzari, L. Lin, and A. Kennedy, "Evidence of disseminated intravascular coagulation in a porcine model following radiation exposure," *Life Sci. Space Res.*, vol. 3, pp. 1–9, Oct. 2014.

[72] G. S. Krigsfeld and A. R. Kennedy, "Is Disseminated Intravascular Coagulation the Major Cause of Mortality from Radiation at Relatively Low Whole Body Doses?," *Radiat. Res.*, vol. 180, pp. 231–234, Sept. 2013.

[73] G. S. Krigsfeld, J. K. Sanzari, and A. R. Kennedy, "The effects of proton radiation on the prothrombin and partial thromboplastin times of irradiated ferrets," *Int. J. Radiat. Biol.*, vol. 88, pp. 327–334, Apr. 2012.

[74] G. S. Krigsfeld, A. R. Savage, J. K. Sanzari, A. J. Wroe, D. S. Gridley, and A. R. Kennedy, "Mechanism of hypocoagulability in proton-irradiated ferrets," *Int. J. Radiat. Biol.*, vol. 89, pp. 823–831, Oct. 2013.

[75] A. R. Kennedy, "Biological effects of space radiation and development of effective countermeasures," *Life Sci. Space Res.*, vol. 1, pp. 10–43, Apr. 2014.

[76] C. J. Maks, X. S. Wan, J. H. Ware, A. L. Romero-Weaver, J. K. Sanzari, J. M. Wilson, S. Rightnar, A. J. Wroe, P. Koss, D. S. Gridley, J. M. Slater, and A. R. Kennedy, "Analysis of white blood cell counts in mice after gamma- or proton-radiation exposure," *Radiat. Res.*, vol. 176, pp. 170–176, Aug. 2011.

[77] A. L. Romero-Weaver, X. S. Wan, E. S. Diffenderfer, L. Lin, and A. R. Kennedy, "Effect of SPE-like proton or photon radiation on the kinetics of mouse peripheral blood cells and radiation biological effectiveness determinations," *Astrobiology*, vol. 13, pp. 570–577, June 2013.

[78] J. Sanzari, X. Wan, G. Krigsfeld, A. Wroe, D. Gridley, and A. Kennedy, "The effects of gamma and proton radiation exposure on hematopoietic cell counts in the ferret model," *Gravit Space Res*, vol. 1, no. 1, pp. 79–94, 2013.

[79] National Council on Radiation Protection and Measurements (NCRP), "Potential impact of individual genetic susceptibility and previous radiation exposure on radiation risk for astronauts," Tech. Rep. No. 167, National Council on Radiation Protection and Measurements, Bethesda, Maryland, 2011.

[80] V. Beir, *Health Risks from Exposure to Low Levels of Ionizing Radiation: BEIR VII Phase 2*. Washington, D.C.: National Academies Press, Mar. 2006. DOI: 10.17226/11340.

[81] M. R. Shavers, N. Zapp, R. E. Barber, J. W. Wilson, G. Qualls, L. Toupes, S. Ramsey, V. Vinci, G. Smith, and F. A. Cucinotta, "Implementation of ALARA radiation protection on the ISS through polyethylene shielding augmentation of the Service Module Crew Quarters," *Adv. Space Res.*, vol. 34, no. 6, pp. 1333–1337, 2004.

[82] Longnecker, David E. and Manning, Frederick J. and Worth, Melvin H., ed., *Review of NASA's Longitudinal Study of Astronaut Health*. Washington, D.C: National Academies Press, U.S. Institute of Medicine, 2004. OCLC: ocm55201397.

[83] "Guidance on Radiation Received in Space Activities.," Tech. Rep. NCRP 98, National Council on Radiation Protection and Measurements, Bethesda, MD, 1989.

[84] "Information needed to make radiation protection recommendations for space missions beyond low-Earth orbit.," Tech. Rep. NCRP Report No. 153, NCRP, Bethesda, MD, 2006.

[85] E. A. Blakely and P. Y. Chang, "A review of ground-based heavy-ion radiobiology relevant to space radiation risk assessment. Part II: Cardiovascular and immunological effects," *Adv. Space Res.*, vol. 40, pp. 461–469, Jan. 2007.

[86] A. Kennedy and X. Wan, "Countermeasures for space radiation induced adverse biological effects," *Adv. Space Res.*, vol. 48, no. 9, pp. 1460–79, 2011.

[87] F. A. Cucinotta and E. Cacao, "Non-targeted effects models predict significantly higher mars mission cancer risk than targeted effects models," *Sci. Rep.*, vol. 7, 2017.

[88] J. Huff and F. Cucinotta, "Risk of degenerative tissue or other health effects from radiation exposure," TR NASA/SP-2009-3405, NASA, Johnson Space Center, 2009.

[89] M. Bender, P. Gooch, and S. Kondo, "The gemini-3 s-4 spaceflight-radiation interaction experiment," *Radiat. Res.*, vol. 31, pp. 91–111, 1967.

[90] B. Fedorenko, S. Druzhinin, L. Yudaeva, V. Petrov, Y. Akatov, G. Snigiryova, N. Novitskaya, V. Shevchenko, and Rubanovich, "Cytogenetic studies of blood lymphocytes from cosmonauts after long-term space flights on mir station," *Advanced Space Research*, vol. 27, pp. 355–9, 2001.

[91] L. Testard, M. Ricoul, F. Hoffschir, A. Flury-Herard, B. Dutrillaux, B. Federenko, V. Gerasimenko, and L. Sabatier, "Radiation-induced chromosome damage in astronauts' lymphocytes.," *Int. J. Radiat. Biol.*, vol. 70, pp. 403–11, 1967.

[92] K. George and F. Cucinotta, "Biological dosimetry in astronauts," Tech. Rep. JSC-CN-23294, NASA Johnson Space Center, Houston, TX, 2011.

[93] J. Huff, L. Carnell, S. Blattnig, L. Chappell, K. George, S. Lumpkins, L. Simonsen, T. Slaba, and C. Werneth, "Risk of radiation carcinogenesis," Tech. Rep. JSC-CN-35748, Houston, TX, 2016.

[94] M. Belli, R. Cherubini, and M. Dalla Vecchia, "Dna fragmentation in v79 cells irradiated with light ions as measured by pulsed-field gel electrophoresis: I. experimental results.," *Int. J. Radiat. Biol.*, vol. 78, pp. 475–82, 2002.

[95] M. Hada, F. Cucinotta, S. Gonda, and H. Wu, "mband analysis of chromosomal aberrations in human epithelial cells exposed to low- and high-let radiation.," *Radiat. Res.*, vol. 168, pp. 98–105, 2007.

[96] C. Johannes, M. Horstmann, and D. M, "Chromosome intrachanges and interchanges detected by multicolor banding in lymphocytes: searching for clastogen signatures in the human genome," *Radiat. Res.*, vol. 161, pp. 540–8, 2007.

[97] F. Cucinotta, M. Kim, and L. Chappell, "Space radiation cancer risk projections and uncertainties – 2012," Tech. Rep. NASA/TP-2013-217375, NASA Johnson Space Center, Houston, TX, 2012.

[98] W. D. Loveland, D. J. Morrissey, and G. T. Seaborg, *Modern nuclear chemistry*. John Wiley & Sons, 2017.

[99] S. P. Ahlen, "Theoretical and experimental aspects of the energy loss of relativistic heavily ionizing particles," *Rev. Mod. Phys.*, vol. 52, p. 121, 1980.

[100] J. F. Ziegler, M. D. Zeigler, and J. P. Biersack, "SRIM – The Stopping and Range of Ions in Matter," *Nuclear Instruments and Methods in Physics Research,Section B: Beam Interactions with Materials and Atoms*, vol. 268, p. 1818, 2010.

[101] N. Bohr, "On the constitution of atoms and molecules," *Phil. Mag. S.*, vol. 26, p. 161, 1913.

[102] H. Bethe, "Braking formula for electrons of relativistic speed," *The European Physical Journal H*, vol. 39, p. 537, 2014.

[103] C. Moller, "On the theory of relativistic electrons in matter," *Ann. Physik*, vol. 14, p. 531, 1932.

[104] U. Fano, "Penetration of Protons, Alpha Particles, and Mesons," *Annual Review of Nuclear and Particle Science*, vol. 13, p. 1, 1963.

[105] F. Bloch, "Stopping power of atoms with several electrons," *Z. Phys.*, vol. 81, p. 363, 1933.

[106] J. F. Ziegler, *Handbook of Stopping Cross Sections for Energetic Ions in All Elements*, vol. 5. New York,NY: Pergamon, 1980.

[107] E. Fermi, "The ionization loss of energy in gases and in condensed materials," *Phys. Rev.*, vol. 57, pp. 485–493, Mar 1940.

[108] R. M. Sternheimer, "Range straggling of charged particles in be, c, al, cu, pb, and air," *Phys. Rev.*, vol. 117, pp. 485–488, Jan 1960.

[109] R. M. Sternheimer, "Density effect for the ionization loss of charged particles," *Phys. Rev.*, vol. 145, pp. 247–250, May 1966.

[110] R. M. Sternheimer, "Density Effect for the Ionizing Loss of Charged Particles in Various Substances," *Phys. Rev. B*, vol. 26, p. 6067, 1982.

[111] A. Crispin and G. N. Fowler, "Density effect in the ionization energy loss of fast charged particles in matter," *Rev. Mod. Phys.*, vol. 42, pp. 290–316, Jul 1970.

[112] R. Sternheimer, M. Berger, and S. M. Seltzer, "Density effect for the ionization loss of charged particles in various substances," *Atomic Data and Nuclear Data Tables*, vol. 30, no. 2, pp. 261–271, 1984.

[113] R. Cabrera-Trujillo, J. Sabin, Y. Öhrn, and E. Deumens, "Case for projectile kinetic energy gain in stopping power studies," *International Journal of Quantum Chemistry*, vol. 94, no. 4, pp. 215–221, 2003.

[114] K. Nakamura, P. D. Group, *et al.*, "Review of particle physics," *Journal of Physics G: Nuclear and Particle Physics*, vol. 37, no. 7A, p. 075021, 2010.

[115] C. Zeitlin, S. Guetersloh, L. Heilbronn, and J. Miller, "Shielding and fragmentation studies," *Radiat. Prot. Dosim.*, vol. 116, p. 123, 2005.

[116] NRC, "National research council - committee on nuclear science: Studies in penetration of charged particles in matter," vol. 1133, 1964.

[117] A. S. Lodhi and D. Powers, "Energy loss of α particles in gaseous C-H and C-H-F compounds," *Phys. Rev. A*, vol. 10, p. 2131, 1974.

[118] R. Kreutz, W. Neuwirth, and W. Pietsch, "Analysis of electronic stopping cross sections of organic molecules," *Phys. Rev. A*, vol. 22, p. 2606, 1980.

[119] D. Powers, "Influence of molecular structure on stopping power of chemical species for helium(+) ions from a low-energy particle accelerator," *Accounts of Chemical Research*, vol. 13, p. 433, 1980.

[120] G. Both, R. Krotz, K. Lohmer, and W. Neuwirth, "Density dependence of stopping cross sections measured in liquid ethane," *Phys. Rev. A*, vol. 28, p. 3212, 1983.

[121] M. R. Shavers, N. Zapp, R. E. Barber, J. W. Wilson, G. Qualls, L. Toupes, S. Ramsey, V. Vinci, G. Smith, and F. A. Cucinotta, "Implementation of ALARA radiation protection on the ISS through polyethylene shielding augmentation of the service module crew quarters," *Adv. Space Res.*, p. 1333, 2004.

[122] J. Miller, C. Zeitlin, F. Cucinotta, L. Heilbronn, D. Stephens, and J. Wilson, "Benchmark studies of the effectiveness of structural and internal materials as radiation shielding for the international space station," *Adv. Space Res.*, vol. 159, p. 381, 2003.

[123] P. M. O'Neill, "Badhwar-O'Neill galactic cosmic ray flux model – revised," *IEEE Trans. Nuc. Sci*, vol. 57, p. 3148, 2010.

[124] C. Zeitlin, S. Guetersloh, L. Heilbronn, J. Miller, A. Fukumura, Y. Iwata, and T. Murakami, "Fragmentation cross sections of 290 and 400 mev/nucleon c12 beams on elemental targets," *Phys. Rev. C*, vol. 76, p. 014911, 2007.

[125] C. Zeitlin, S. Guetersloh, L. Heilbronn, J. Miller, A. Fukumura, Y. Iwata, L. Murakami, T.and Sihver, and D. Mancusi, "Fragmentation cross sections of medium-energy Cl 35, Ar40, and Ti 48 beams on elemental targets," *Phys. Rev. C*, vol. 77, p. 034605, 2008.

[126] R. Tripathi, F. A. Cucinotta, and J. W. Wilson, "Accurate universal parameterization of absorption cross sections," *Nuclear Instruments and Methods in Physics Research Section B: Beam Interactions with Materials and Atoms*, vol. 117, no. 4, pp. 347–349, 1996.

[127] R. Tripathi, J. W. Wilson, and F. A. Cucinotta, "Accurate universal parameterization of absorption cross sections ii—neutron absorption cross sections," *Nuclear Instruments and Methods in Physics Research Section B: Beam Interactions with Materials and Atoms*, vol. 129, no. 1, pp. 11–15, 1997.

[128] R. Tripathi, F. Cucinotta, and J. Wilson, "Accurate universal parameterization of absorption cross sections iii–light systems," *Nuclear Instruments and Methods in Physics Research Section B: Beam Interactions with Materials and Atoms*, vol. 155, no. 4, pp. 349–356, 1999.

[129] G. D. Badhwar, W. Atwell, B. Cash, V. M. Petrov, Y. A. Akatov, I. V. Tchernykh, V. A. Shurshakov, and V. A. Arkhangelsky, "Radiation Environment on the Mir Orbital Station During Solar Minimum," *Advanced Space Research*, vol. 2, p. 501, 1998.

[130] L. Pinsky, J. Chancellor, and D. Minthaka, "Evolving the Medipix2 Technology For Use As An Active Space Radiation Dosimeter," in *Aerospace Conference, 2008 IEEE*, p. 1, IEEE, 2008.

[131] N. Stoffle, L. Pinsky, M. Kroupa, S. Hoang, J. Idarraga, C. Amberboy, R. Rios, J. Hauss, J. Keller, A. Bahadori, and *et al.*, "Timepix-based radiation environment monitor measurements aboard the International Space Station," *Nuclear Instruments and Methods in Physics Research Section A: Accelerators, Spectrometers, Detectors and Associated Equipment*, vol. 782, p. 143, 2015.

[132] S. Hoang, L. Pinsky, R. Vilalta, and J. Jakubek, "LET estimation of heavy ion particles based on a timepix-based Si detector," in *J. Physics: Conference Series*, vol. 396, p. 022023, 2012.

[133] M. Kroupa, A. Bahadori, T. Campbell-Ricketts, A. Empl, S. M. Hoang, J. Idarraga-Munoz, R. Rios, E. Semones, N. Stoffle, L. Tlustos, and *et al.*, "A semiconductor radiation imaging pixel detector for space radiation dosimetry," *Life sciences in space research*, vol. 6, p. 69, 2015.

[134] A. A. Bahadori, E. S. Semones, R. Gaza, M. Kroupa, R. R. Rios, N. N. Stoffle, T. Campbell-Ricketts, L. A. Pinsky, and D. Turecek, "Battery-operated Independent Radiation Detector Data Report from Exploration Flight Test 1," tech. rep., 2015.

[135] K. B. Athreya, "Bootstrap of the mean in the infinite variance case," *Ann. Statist.*, vol. 15, p. 724, 06 1987.

[136] A. Ferrari, P. R. Sala, A. Fasso, and J. Ranft, "Fluka: A multi-particle transport code (program version 2005)," tech. rep., 2005.

[137] S. Agostinelli, J. Allison, K. a. Amako, J. Apostolakis, H. Araujo, P. Arce, M. Asai, D. Axen, S. Banerjee, G. . Barrand, *et al.*, "Geant4—a simulation toolkit," *Nuclear instruments and methods in physics research section A: Accelerators, Spectrometers, Detectors and Associated Equipment*, vol. 506, no. 3, pp. 250–303, 2003.

[138] T. Goorley, M. James, T. Booth, F. Brown, J. Bull, L. Cox, J. Durkee, J. Elson, M. Fensin, R. Forster, *et al.*, "Features of mcnp6," in *SNA+ MC 2013-Joint International Conference on Supercomputing in Nuclear Applications+ Monte Carlo*, p. 06011, EDP Sciences, 2014.

[139] H. Wellisch and D. Axen, "Total reaction cross section calculations in proton-nucleus scattering," *Physical Review C*, vol. 54, no. 3, p. 1329, 1996.

[140] W.-q. Shen, B. Wang, J. Feng, W.-L. Zhan, Y.-T. Zhu, and E.-P. Feng, "Total reaction cross section for heavy-ion collisions and its relation to the neutron excess degree of freedom," *Nuclear Physics A*, vol. 491, no. 1, pp. 130–146, 1989.

[141] L. Sihver, M. Lantz, T. T. Böhlen, A. Mairani, A. Cerutti, and A. Ferrari, "A comparison of total reaction cross section models used in fluka, geant4 and phits," in *Aerospace Conference, 2012 IEEE*, pp. 1–10, IEEE, 2012.

[142] A. S. Lodhi and D. Powers, "Energy loss of α particles in gaseous c-h and c-h-f compounds," *Phys. Rev. A*, vol. 10, pp. 2131–2140, Dec 1974.

[143] R. Kreutz, W. Neuwirth, and W. Pietsch, "Analysis of electronic stopping cross sections of organic molecules," *Phys. Rev. A*, vol. 22, p. 2606, 1980.

[144] D. Powers, "Influence of molecular structure on stopping power of chemical species for helium(+) ions from a low-energy particle accelerator," *Accounts of Chemical Research*, vol. 13, p. 433, 1980.

[145] G. Both, R. Krotz, K. Lohmer, and W. Neuwirth, "Density dependence of stopping cross sections measured in liquid ethane," *Phys. Rev. A*, vol. 28, p. 3212, 1983.

[146] J. F. Ziegler, M. D. Zeigler, and J. P. Biersack, "SRIM – The Stopping and Range of Ions in Matter," *Nuclear Instruments and Methods in Physics Research, Section B: Beam Interactions with Materials and Atoms*, vol. 268, p. 1818, 2010.

[147] M. Durante and F. A. Cucinotta, "Heavy ion carcinogenesis and human space exploration," *Nature Reviews Cancer*, vol. 8, p. 465, 2008.

[148] C. Zeitlin, S. Guetersloh, L. Heilbronn, and J. Miller, "Shielding and fragmentation studies," *Radiat. Prot. Dosim*, vol. 116, p. 123, 2005.

[149] C. Zeitlin, L. Heilbronn, J. Miller, S. E. Rademacher, T. Borak, T. R. Carter, K. A. Frankel, W. Schimmerling, and C. E. Stronach, "Heavy fragment production cross sections from 1.05 gev/nucleon $^{56}\mathrm{Fe}$ in c, al, cu, pb, and $\mathrm{ch_2}$ targets," *Phys. Rev. C*, vol. 56, pp. 388–397, Jul 1997.

[150] C. N. Knott, S. Albergo, Z. Caccia, C.-X. Chen, S. Costa, H. J. Crawford, M. Cronqvist, J. Engelage, P. Ferrando, R. Fonte, and *et al.*, "Interactions of relativistic neon to nickel projectiles in hydrogen, elemental production cross sections," *Phys. Rev. C*, vol. 53, p. 347, 1996.

[151] C. Zeitlin, L. Sihver, C. La Tessa, D. Mancusi, L. Heilbronn, J. Miller, and S. B. Guetersloh, "Comparisons of fragmentation spectra using 1GeV/amu 56 Fe data and the PHITS model," *Radiation Measurements*, vol. 43, p. 1242, 2008.

[152] C. La Tessa, S. Guetersloh, L. Heilbronn, J. Miller, L. Sihver, and C. Zeitlin, "Fragmentation of 1 gev/nucleon iron ions in thick targets relevant for space exploration," *Advances in Space Research*, vol. 35, no. 2, pp. 223–229, 2005.

[153] N. Stoffle, L. Pinsky, M. Kroupa, S. Hoang, J. Idarraga, C. Amberboy, R. Rios, J. Hauss, J. Keller, A. Bahadori, *et al.*, "Timepix-based radiation environment monitor measurements aboard the international space station," *Nuclear Instruments and Methods in Physics Research Section A: Accelerators, Spectrometers, Detectors and Associated Equipment*, vol. 782, pp. 143–148, 2015.

[154] T. C. Slaba, S. R. Blattnig, J. W. Norbury, A. Rusek, C. La Tessa, and S. A. Walker, "Simulator Reference Field and a Spectral Approach for Laboratory Simulation," tech. rep., 2015.

[155] E. Elmore, X.-Y. Lao, R. Kapadia, M. Swete, and J. L. Redpath, "Neoplastic Transformation In Vitro by Mixed Beams of High-Energy Iron Ions and Protons," *Radiation Research*, vol. 176, p. 291, 2011.

[156] R. J. Fry, *Radiation Protection Dosimetry*, vol. 100. 2002.

[157] K. Niita, T. Sato, H. Iwase, H. Nose, H. Nakashima, and L. Sihver, "Phits – a particle and heavy ion transport code system," *Radiation measurements*, vol. 41, pp. 1080–1090, 2006.

[158] K. Niita, H. Takada, S.-i. Meigo, and Y. Ikeda, "High-energy particle transport code nmtc/jam," *Nuclear Instruments and Methods in Physics Research Section B: Beam Interactions with Materials and Atoms*, vol. 184, no. 3, pp. 406–420, 2001.

[159] Y. Nara, N. Otuka, A. Ohnishi, K. Niita, and S. Chiba, "Relativistic nuclear collisions at 1 0 a gev energies from p+ be to au+ au with the hadronic cascade model," *Physical Review C*, vol. 61, no. 2, p. 024901, 1999.

[160] K. Niita, S. Chiba, T. Maruyama, T. Maruyama, H. Takada, T. Fukahori, Y. Nakahara, and A. Iwamoto, "Analysis of the (n, xn') reactions by quantum molecular dynamics plus statistical decay model," *Physical Review C*, vol. 52, no. 5, p. 2620, 1995.

[161] J. F. Briesmeister, "A general monte carlo n-particle transport code," *LA-12625-M*, 1997.

[162] K. Shibata, T. Kawano, T. Nakagawa, O. Iwamoto, J.-I. Katakura, T. Fukahori, S. Chiba, A. Hasegawa, T. Murata, H. Matsunobu, *et al.*, "Japanese evaluated nuclear data library version 3 revision-3: Jendl-3.3," *Journal of nuclear science and technology*, vol. 39, no. 11, pp. 1125–1136, 2002.

[163] T. Armstrong and K. Chandler, "Spar, a fortran program for computing stopping powers and ranges for muons, charged pions, protons, and heavy ions," tech. rep., Oak Ridge National Lab., 1973.

[164] K. Niita, T. Sato, H. Iwase, H. Nose, H. Nakashima, and L. Sihver, "Phits – a particle and heavy ion transport code system," *Radiation measurements*, vol. 41, pp. 1080–1090, 2006.

[165] R. M. Sternheimer, "Density Effect for the Ionizing Loss of Charged Particles in Various Substances," *Phys. Rev. B*, vol. 26, p. 6067, 1982.

[166] R. Sternheimer, M. Berger, and S. M. Seltzer, "Density effect for the ionization loss of charged particles in various substances," *Atomic Data and Nuclear Data Tables*, vol. 30, no. 2, pp. 261–271, 1984.

APPENDIX A

PARTICLE AND HEAVY ION TRANSPORT SYSTEM (PHITS)

A.1 PHITS Overview

The transported particle can generate different types of particles. These processes are described collectively by the transport equation. The nodal solution of the transport equation requires averaging of the flux density, and other dependent variable in the transport equation, over discrete time intervals, energy groups, solid angles, and spatial volume elements. The stochastic solution of the particle transport problem relies on the simulation of particle movement and interactions via random variables sampled from probability distributions. It is found that the body crossing estimator evaluates the flux crossing a surface, by accumulating the weight of particles crossing the surfaces divided by the absolute value of the cosine of the angle between the normal to the surface and direction of the incident particle.

Deterministic particle transport codes utilize solutions to the Boltzman transport equation. Here the one-body phase-space distribution function is evaluated by integrating the test particle tracks in the phase-space. These solutions to the Boltzmann equation include only the mean values of the one-body observables in the phase space. They cannot provide information about the fluctuations around the mean value, because the Boltzmann equation has no information about the two-body and higher correlations that determine the fluctuation around the mean value of the one-body observables. Additionally, the deposited energy distribution in a volume or cell of unit area cannot be described with deterministic codes, only the mean value.

The 3D Monte Carlo approach can be considered as a numerical solution of the 3D Boltzmann equation. The advantage to utilizing a 3D Monte Carlo approach is allowing the simulation of realistic geometry and physical conditions that leveraging an event generator in which each collision is simulated in accordance the energy and momentum conservation laws.A 3-D, Monte Carlo-based computer code called Particle and Heavy Ion Transport code System, or PHITS was chosen as the

computer simulation for this dissertation study because it can simulate particle induced reactions and features an event generator mode that will produce a fully correlated transport for all particles with energies up to 200 GeV/n [157].

PHITS is utilizes the Liege Intranuclear Cascade (INCL4.6) an the Jet AA microscopic transport mode (JAM) models [158] for nucleon/meson transport. JAM and INCL4.6 are intra-nuclear cascade models that simulate the dynamic stages of hadron-induced nuclear reactions in the high and intermediate energy regions, respectively. JAM and INCL4.6 are hadronic cascade models that which treats all hadronic states and resonances, as well as their anti-particles, with explicit spin and isospin. INCL4.6 is a used to simulate the nucleon, pion and light ion induced reactions on nuclei, for incident energies ranging from a few tens of MeV/n to a few GeV/n, while JAM is used for particle induced reactions up to 200 GeV/n.

The JAERI quantum molecular dynamics (JQMD) for nucleus-nucleus collisions and nucleus-induced reactions [159, 160]. In the JQMD model, a nucleus is described as a self-binding system of nucleons which are interacting with each other through effective interactions in a framework of molecular dynamics. Nuclear and atomic data libraries are used for low-energy neutron-induced reactions, photo-, and electro-atomic interactions. MCNP4C for neutron transport and JENDL-4.0 for photon and electron nuclear interactions [161, 162]. Photo-nuclear reactions can be treated only for the lower energy regions in which the giant resonance is the dominant reaction mechanism.

Fission and evaporation processes for both hadron and nucleus induced reactions are described by the generalized evaporation model (GEM). The user can specify whether to use the Shen formula or the Tripathi models for calculating the total reaction cross sections and either the SPAR or ATIMA models for stopping power calculations. Both utilize the slowing down approximation [163, 164].

The development of PHITS was in the support of heavy-ion radiotherapy and the intermediate energies of interest in this study. There are several other notable 3D Monte Carlo simulations *e.g.,* FLUKA, GEANT4, MCMPX [136, 137, 138]. PHITS has been shown to be in close agreement with similar codes [141] as demonstrated by Figure 4.4. Additionally, PHITS was utilized in many

beam-line experiments of cross-section analysis using ions, targets, and energies relevant to space radiation [124, 125, 151].

Monte Carlo multi-purpose particle transport codes like PHITS simulate and describe two physical processes, transport and collision. Particle transport includes the capability to describe the motion of a charged particle under an external magnetic field. This description also includes neutral particles that would move along straight path with constant energy until the next collision point. During the transport process, charged particles (up to Z=2) and heavy charged particles (Z >3) moving through a target material will lose energy through ionization processes in the medium with target nuclei and electrons while undergoing multiple Coulomb scatters. PHITS treats the ionization reactions as energy loss is given by the charge density of the material and the momentum of the transported particle, including accounting for fluctuations in energy loss and angular deviation.

The collision and the decay of unstable particles are treated during the collision processes. Here the total reaction cross section and/or the lifetime of the particle is the primary quantity when determining the mean free path of the transported particles. Following each interaction with the medium, Monte Carlo is utilized to determine the next collision point according the mean free path. Secondary particles generated on the collision processes are calculated using the particles' final states. For neutron induced reactions in the low-energy regions, PHITS uses the cross sections from the evaluated nuclear data libraries ENDF-B/VI, JENDL-4.0 [162]; the LA150 library for particle energies up to 150 MeV/n; and JENDL-HE for particles up to 3 GeV/n.

The biggest advantage of using a computer simulation is avoiding the large costs of multiple experiments at accelerator facilities. Using a simulation will allow sufficient results to still be generated in a relatively short time.

APPENDIX B

MATERIAL AND COMPOUND DATA TABLES

B.1 Data Table of Atomic Elements

Table B.1: Data Table of Atomic Elements for $1 \leq Z \leq 50$

Element	**Symbol**	**Density** (g/cm^3)	$\langle I \rangle$ **(eV)**
Hydrogen	H	$8.374x10^{-5}$	19.2
Helium	He	$1.663x10^{-4}$	41.8
Lithium	Li	0.533	40.0
Beryllium	Be	1.848	63.7
Boron	B	2.34-2.37	–
Carbon	C	1.9-2.3	78.0
Nitrogen	N	$1.165x10^{-3}+$	82.0
Oxygen	O	$1.331x10^{-3}$	95.0
Flourine	F	$1.58x10^{-3}$ 7	–
Neon	N	$8.385x10^{-4}$	137
Sodium	S	0,969	149
Magnesium	Mg	1.735	156
Aluminum	Al	2.69	166
Silicon	Si	2.32	173
Phosphorus	P	1.82-2.69	–
Sulfur	S	1.954,2.07	–
Chlorine	Cl	$2.995x10^{-3}$	–
Argon	Ar	$1.622x10^{-3}$	188
Potassium	K	09.86	190

Table B.1

Element	**Symbol**	**Density** (g/cm^3)	$\langle I \rangle$ **(eV)**
Calcium	Ca	1.55	191
Scandium	Sc	2.98	–
Titanium	Ti	4.54	233
Vanadium	V	6.10	245
Chromium	Cr	7.18	–
Manganese	Mn	7.21-7.44	272
Iron	Fe	7.86	286
Cobalt	Co	8.9	297
Nickel	Ni	8.88	311
Copper	Cu	8.94	322
Zinc	Zn	7.11	330
Gallium	Ga	5.88	–
Germanium	Ge	5.31	350
Arsenic	As	5.73	–
Selenium	Se	4.28,4.79	348
Bromine	Br	$7.07x10^{-3}$	–
Krypton	Kr	$3.478x10^{-3}$	352
Rubidium	Rb	1.529	363
Strontium	Sr	2.54	–
Yttriuim	Y	4.46	–
Zirconium	Zr	6.49	–
Niobium	Nb	8.54	–
Molybdenum	Mo	10.20	–
Technetium	Tc	11.50	–
Ruthenium	Ru	12.41	–

Table B.1

Element	**Symbol**	**Density** (g/cm^3)	$\langle I \rangle$ **(eV)**
Rhodium	Rh	12.41	–
Palladium	Pd	12.0	–
Silver	Ag	10.48	470
Cadmium	Cd	8.65	469
Indium	In	7.30	487
Tin	Sn	7.30	488

B.2 Material Data Table For Some Compounds, Mixtures, and Polymers

Table B.2: Data Table For Some Compounds, Mixtures, and Polymers. Adapted from Sternheimer *et al.*[165, 166]

Material	Density (g/cm^3)	Electron Density (10^{23} e/g)	$\langle I \rangle$ (eV)
A-150 plastic	1.127	3.306	65.1
Air	0.001205	3.006	63.2
Calcium Flouride (CaF_2)	3.18	2.931	166l
Carbon Dioxide (CO_2)	0.001842	3.010	85.0
Cesium Iodide (CsI)	4.51	2.503	553
Fatty Tissue (ICRP)	0.92	3.363	63.2
Lithium Flouride (LiF)	2.64	2.786	94
Lucite ($C_5H_8O_4$)	1.19	3.248	74.0
Skeletal Muscle (ICRP)	1.04	3.308	75.3
Mylar ($C_{10}H_8O_4$)	1.14	3.299	78.7
Nylon-6 ($C_6H_{11}NO$)	1.14	3.299	63.9
Polycarbonate ($C_{16}H_{14}O_3$)	1.2	3.173	73.1
Polyethylene (C_2H_4)	0.94	3.435	57.4
Polymide ($C_{22}H_{10}N_2O_5$)	1.42	3.087	79.6
Polypropylene (C_3H_5)	0.9	3.372	59.2
Polystyrene (C_8H_8)	1.03	3.238	68.7
Polyvinyl Chloride ($C_2H_{13}Cl$)	1.30	3.083	108.2
Pyrex (borisilicate glass)	2.23	2.993	134
Silicon Dioxide (SiO_2)	2.32	3.007	139.2
Silver Bromide (AgBr)	6.47	2.629	487
Sodium Iodide (NaI)	3.67	2.571	452
Teflon (C_2F_4)	2.20	2.890	99.1
Water	0.9982	3.343	75

B.3 Accuracy of Bragg's Rule in Some Compounds

Table B.3: Accuracy of Bragg's Rule in Heavy Compounds

Compound	Deviation from Bragg's Rule (%)
Al_2O_3	< 1
Au-Ag alloys	< 1
Au-Cu alloys	< 2
BaF_2	< 2
$BaCl_2$	< 2
Fe_2O_3	< 1
Fe_3O_4	< 1
HSi_2	< 2
NbC	< 2
NbN	< 2
Nb_2O_5	< 1
RhSi	< 2
SiC	< 2
Si_3N_4	< 2
Ta_2O_5	< 1
TiO_2	< 1
WO_3	< 2
ZnO	< 1

B.4 Stopping Power Data for Relevent Materials

Table B.4: Data sets of materials and block lengths

Material	**Ionizing Potential (eV)**	**Density (g/cm^3)**	**Data Sets Available**
Aluminum	166	2.69	5cm - 100cm
High Density Polyethylene (HDPE)	73.1	1.2	5cm - 100cm
Iron	286	7.874	5cm - 50cm
Lead	823	13.5	5cm - 50cm
Plastic Scintillator (Vinyltoluene)	64.7	1.032	5cm - 40cm
Poly(methyl methacrylate) (Lucite)	74	1.19	5cm - 100cm
Polyethylene Terephthalate) (Mylar)	78.7	1.4	5cm - 100cm
Polystyrene	68.7	1.03	5cm - 100cm
Polyethylene	57.4	0.94	5cm - 110cm
Pyrex	1.34	2.23	5cm - 100cm
Water	57	1.0	5cm - 100cm